



11/14/2025

# Long-Term Shrinkage and Mechanical Properties of Alkali-Activated Slag

by

R. Khalifa

to obtain the degree of Master of Science in Civil Engineering

at the Delft University of Technology

to be defended publicly on 27-11-2025 at 13.00h.

**Student number:**

**4804295**

**Chair:**

**Prof. Dr. G. (Guang) Ye**

**Thesis committee:**

**Dr. G. (Gozde) Ozerkan**

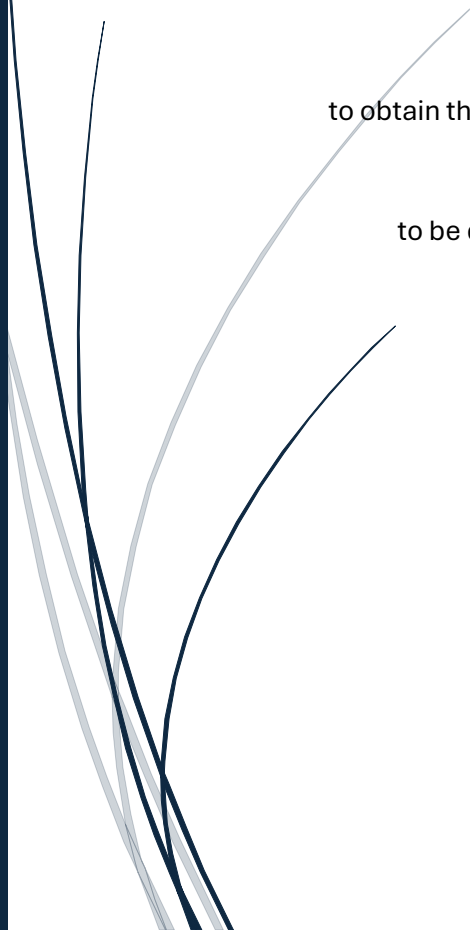
**Dr. C. (Chen) Liu**

**Dr. F. (Fengqiao) Zhang**

**Dr.ir. M. (Marc) Ottele**

**Place:**

**Faculty of Civil Engineering, Delft**



## Acknowledgements

To begin with, I would like to express my heartfelt gratitude to my supervisor Dr.ir G. Ye, Dr. ir G. Ozerkan, Dr. C. Liu, Dr. Fengqiao Zhang, and Dr. Marc Ottele . I would like to thank my research supervisor who was a fundamental part of the success of this project. With their expertise in sustainable construction materials and feedback, the quality and direction of this work was greatly aided.

I thank academic and technical personnel in the Department of Civil Engineering, TU Delft for granting access to laboratory facilities and materials and assisting me with various aspects of the experimental work. We express our special thanks to lab technicians for their assistance in preparing and testing the specimen.

I wish to extend my heartfelt gratitude to my fellow students and colleagues for sharing the burden with me and engaging me in dialogue during the course of study. They always intervened and encouraged us at exactly the right time.

For the last I'd like to thank all my family and friends for their love, patience and moral coming. This thesis would not have been possible without your encouragement and deep understanding.

I would like to thank the people who helped me in various ways to make this research a success.

## Abstract

Alkali-activated slag (AAS) binders offer a sustainable alternative to Portland cement, yet their long-term mechanical properties remain uncertain. Despite reported declines in strength and stiffness over time, the mechanisms behind these reductions are not fully understood. Existing research largely focuses on short-term properties or isolated factors, and there is a lack of integrated studies spanning paste, mortar, and concrete. The role of dry shrinkage in long-term degradation and the development of effective mitigation strategies has also received limited attention.

This thesis addresses these gaps by investigating the causes of long-term reductions in the strength and elastic modulus of AAS mortars and concretes and evaluating potential solutions. An experimental program examined the influence of activator type (sodium silicate vs. sodium carbonate), curing regime (ambient, 7-day fog, and fog-sealed curing), and gypsum addition. Mortar and concrete specimens were monitored for their compressive strength, flexural strength, elastic modulus, and dry shrinkage over a six-month period. Results were also compared to traditional Portland cement systems (CEM I and CEM III) to benchmark performance. Moreover, correlations between mechanical properties and dry shrinkage were analysed, and the elastic modulus and shrinkage were compared with model predictions.

Findings indicate that early fog curing substantially reduces shrinkage and increases mechanical properties by limiting moisture loss and microcrack formation. Sodium silicate activation produces denser microstructures, higher strengths, and stiffness than sodium carbonate systems. Incorporating 6% gypsum mitigates shrinkage by over 30% through ettringite formation and pore refinement, while slightly delaying early strength gain.

In AAS mortars and concrete, increasing dry shrinkage reduces both elastic modulus and flexural strength, while compressive strength may still rise under ambient curing, whereas Portland cement mortars (CEM I and CEM III) exhibit simultaneous gains in compressive strength, elastic modulus, and flexural strength due to ongoing hydration, and early-age fog curing in AAS mitigates shrinkage and microcracking, maintaining higher stiffness and flexural strength with long-term stabilisation as the microstructure densifies. Comparisons with Standard predictive models indicate that OPC-based codes overestimate the AAS elastic modulus, although long-term shrinkage trends are reasonably captured.

This study provides new insight into the mechanisms linking shrinkage to long-term degradation in AAS and demonstrates that combining sodium silicate activation, gypsum addition, and early fog curing offers a practical route to durable, shrinkage-resistant, and sustainable AAS concretes suitable for structural applications.

## Contents

Acknowledgements .....	1
Abstract.....	2
List of terms and abbreviations .....	6
Chapter 1 .....	7
1. Introduction .....	7
1.1. Background information .....	7
1.2. Research aim and Strategy .....	9
1.3. Scope.....	9
1.4. Outline of master thesis .....	10
Chapter 2 .....	11
2. Literature review on AAM .....	11
2.1. Alkali-activated materials.....	11
2.2. Precursors .....	12
2.2.1. Blast furnace slag .....	12
2.2.2. Fly ash.....	12
2.2.3. Slag-to-fly-ash ratio .....	13
2.3. Alkaline activators.....	15
2.3.1. Sodium Carbonate .....	15
2.3.2. Sodium Silicate .....	16
2.3.3. Sodium hydroxide solution .....	17
2.3.4. Potassium hydroxide and silicate .....	18
2.4. Curing conditions.....	19
2.5. Water content .....	21
2.6. Mechanical properties .....	22
2.6.1. Compressive strength .....	22
2.6.2. Flexural strength .....	24
2.7. Dry Shrinkage .....	28
2.7.1. Introduction to dry shrinkage .....	28
2.7.2. Primary concept of dry shrinkage .....	28
2.7.3. Terminology .....	29
2.7.4. Fundamental Factors Influencing Dry Shrinkage. ....	30
2.8. Dry Shrinkage Mitigation Strategies in Alkali-Activated Materials .....	30
2.8.1. Air-entraining agents .....	30
2.8.2. Gypsum.....	31
2.8.3. Shrinkage reduction admixture (SRA).....	31

2.8.4. Fibre Reinforcement.....	31
2.8.5. Chemical Admixtures: Naphthalene Formaldehyde Polymers (S) and Water-Reducing Agents (WRRre).....	31
2.9. Literature review on Portland-cement .....	32
2.9.1. Portland-cement .....	32
2.9.2. Curing conditions .....	35
2.9.3. Admixtures for Portland cement .....	37
2.9.3. Mechanical properties .....	38
2.9.4. Shrinkage .....	39
2.10. Knowledge gaps in long-term mechanical research .....	44
Chapter 3 .....	46
3. Approach & Methodology.....	46
3.1. Materials .....	46
3.2. Mix Design .....	46
3.3. Experimental methods .....	50
3.3.1. Alkaline-activated slag paste .....	50
3.3.2. Alkaline-activated slag mortars .....	50
3.3.3. Alkaline-activated slag concrete .....	53
Chapter 4 .....	56
4. Results and Discussion .....	56
4.1. Compressive Strength of AAS mortars.....	56
4.1.1. Effect of alkaline activators .....	56
4.1.2. Effect of curing conditions .....	58
4.1.3. Effect of Admixtures .....	59
4.2. Flexural strength of AAS mortars .....	60
4.2.1. Effect of alkaline activators .....	60
4.2.2. Effect of curing conditions .....	62
4.2.3. Effect of admixtures.....	63
4.3. E-modulus of AAS mortars .....	64
4.3.1. Effect of alkaline activators .....	64
4.3.2. Effect of curing conditions .....	65
4.3.3. Effect of admixtures.....	66
4.3.4. Comparison E-modulus with Predicted Model Codes .....	67
4.4. Mechanical properties of alkali-activated slag concrete .....	68
4.4.1. Compressive strength.....	68
4.4.2. Flexural strength.....	69

4.4.3. Elastic modulus .....	70
4.4.4. Correlation between compressive strength and flexural strength & modulus of elasticity.....	71
4.5. Dry shrinkage and weight loss of AAS mortars .....	72
4.5.1. Effect of the alkaline activators .....	72
4.5.2. Effects of curing conditions.....	77
4.5.3. Effect of the admixtures .....	79
4.5.4. Dry shrinkage and weight loss of AAS concrete .....	82
4.5.5. Comparison dry shrinkage with Predicted Model Codes .....	85
4.5.6. Correlation between dry shrinkage and flexural strength & modulus of elasticity ....	86
4.6. XRD analysis.....	87
4.7. Summary and limitations .....	88
4.7.1. Summary Tables.....	88
4.7.2. Limitations of the Study .....	91
Chapter 5 .....	92
5. Conclusion and recommendations .....	92
5.1 Conclusions .....	92
5.1.1. Activator Type.....	92
5.1.2. Curing Conditions .....	92
5.1.3. Admixtures.....	93
5.1.4. Mortar vs. Concrete Behaviour .....	93
5.1.5. AAS vs. OPC .....	93
5.1.6. Correlations and Comparison with Model Predictions.....	94
5.1.7. Suggestion to improve long-term mechanical properties .....	94
5.2. Recommendations .....	95
References .....	96
Appendix .....	117
Appendix A: Determination of secant modulus of elasticity .....	117
Appendix B: Methods of testing cement - Part 1: Determination of strength.....	119
B1) Flexural Strength Testing Procedure .....	119
B2) Compressive Strength Testing Procedure .....	119

## List of terms and abbreviations

- Precursor
  - AASC                      Alkali Activated Slag Concrete (ground granulated blast furnace slag activated)
    - GGBS                      Ground Granulated Blast furnace Slag activated
    - BFS                              Blast Furnace Slag activated
  - FA                              Fly Ash
    - LCFA                      Low Calcium Fly Ash
    - HCFA                      High Calcium Fly Ash
  - AM                              Activated Metakaolin
  - AMF                              Activated Metakaolin + Fly ash
  - AS                              Activated Slag
  - ASF                              Activated Slag + Fly Ash
  - SF                              Silica Fume
  - MK                              Metakaolin
- Alkali Activator (kg/m<sup>3</sup>)
  - Na<sub>2</sub>SiO<sub>3</sub>                      Sodium silicate (waterglass)
  - NaOH                              Sodium hydroxide
  - H<sub>3</sub>PO<sub>4</sub>                      Phosphoric acid
  - CaCO<sub>3</sub>                      Calcium carbonate
  - Ca(OH)<sub>2</sub>                      Calcium di-hydroxide
- Reaction product
  - N-A-S-H                      Sodium-Alumino-Silicate-Hydrate (reaction product of alkali activation for low-calcium materials, like FA)
  - C-(A)-S-H                      Calcium-(Alumino)-Silicate-Hydrate (reaction product of alkali-activation for high-calcium materials, like BFS)
- Chemical notations cement industry
  - C                              CaO
  - S                              SiO<sub>2</sub>
  - A                              Al<sub>2</sub>O<sub>3</sub>
  - F                              Fe<sub>2</sub>O<sub>3</sub>
  - S                              SO<sub>4</sub>
  - H                              H<sub>2</sub>O
- Other
  - w/c                              Water to cement ratio
  - w/b                              Water to binder ratio

# Chapter 1

## 1. Introduction

### 1.1. Background information

In recent years, there has been a growing awareness of the environmental implications of climate change and the associated increase in greenhouse gas emissions. Among the major contributors to global carbon dioxide (CO<sub>2</sub>) emissions is the construction sector, with cement production identified as a particularly significant source. Research indicates that the manufacturing of cement accounts for approximately 5–8% of global CO<sub>2</sub> emissions [1].

Figure 1.1 illustrates (a) global cement production and (b) the global process emissions from cement production over the past century. A marked acceleration in cement production has been observed in recent decades, reflecting the growing societal demand for binder materials. However, this development poses a critical challenge, as it conflicts with the urgent need to reduce greenhouse gas emissions [2].

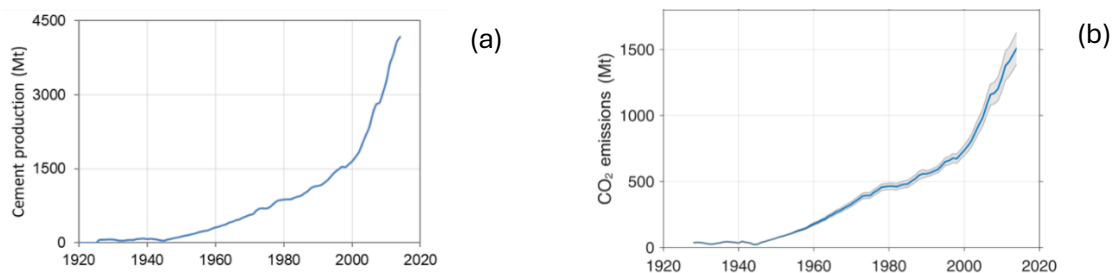


Figure 1.1. (a) Global cement production over the past century; (b) global process emissions from cement production during the same period [2].

In line with the Paris Agreement's goal of limiting global warming to well below 2 °C, achieving climate neutrality by 2050 requires significant reductions in greenhouse gas emissions [3]. The Netherlands has committed to a fully circular construction sector by mid-century, with concrete playing a central role in this transition. This study examines alkali-activated materials (AAM) as a low-carbon alternative to Portland cement [4]. Produced from industrial by-products, AAM can reduce CO<sub>2</sub> emissions by 26–45% [5], offering a promising pathway toward more sustainable construction.

To meet the growing demand for construction materials while reducing greenhouse gas emissions, research has increasingly focused on sustainable alternatives to conventional cement [6]. AAM produced by chemically activating aluminosilicate-rich precursors with alkaline solutions, have emerged as a promising option [7]. Unlike ordinary Portland cement (OPC), whose production is energy-intensive and carbon-intensive, AAM can utilise industrial by-products, such as ground granulated blast-furnace slag and fly ash, resulting in a lower overall environmental impact despite the use of minor quantities of industrial activators like NaOH and Na<sub>2</sub>SiO<sub>3</sub> [8].

AAM systems, particularly alkali-activated slag (AAS), exhibit high compressive strength under ambient curing [9, 10]. However, rapid setting can limit workability, which can be mitigated by blending slag with supplementary precursors to balance setting behaviour and mechanical performance [11, 12]. Chemically, alkali-activated concretes (AAC) demonstrate resistance to



aggressive environments—including acids, chlorides, sulphates, and  $\text{CO}_2$ —comparable to or exceeding that of OPC-based concretes [13, 14], with reduced susceptibility to alkali–silica reaction [15] and enhanced thermal stability and fire resistance [15]. Although AAM generally demonstrate excellent early-age strength and durability, they are prone to rapid polymerisation, which can lead to a stagnation in strength development beyond 28 days [16]. In contrast, OPC typically continues to gain strength over extended periods, driven by ongoing hydration reactions [17, 18, 19, 20].

Despite the several positive effects of AAM, several studies have reported a decline in the mechanical properties of AAM over time [21, 22, 23, 24, 25]. The mechanical properties of ordinary Portland concrete, specifically its strength and stiffness, generally improve with age under standard curing conditions, such as moist curing at 20 °C [26]. Under alternative curing regimes, however, the development of compressive strength may either stagnate or progress at a slower rate compared to continuously moist-cured specimens. Recent investigations into concrete have revealed instances in which strength and stiffness can diminish over time [27, 4]. For example, Lantsoght et al. [28] observed a temporary reduction in the measured splitting tensile strength of a high-strength concrete. Similarly, Prinsse et al. [27] reported declines in flexural strength, splitting tensile strength, and elastic modulus in two AAC mixtures exposed to 50% relative humidity after 28 days of moist curing at 20 °C. These findings align with earlier studies on alkali-activated systems [29, 4]. Collins and Sanjayan [27] observed a time-dependent decrease in compressive strength in AAS systems. Similarly, research by Wardhono et al. [3], and Bezemer et al. [28] documented reductions in both flexural strength and elastic modulus in AAS materials as they aged.

Several factors have been identified as influential in the temporal evolution of measured or apparent concrete strength and stiffness, including curing regime, concrete strength grade, and specimen dimensions. With regard to curing, Asselanis et al. [30] and Kocab et al. [31] concluded that specimens continuously exposed to moist curing develop higher elastic moduli compared to those subjected to drying after an initial moist period. The influence of curing on compressive strength, however, is less clear. Some studies have found that moist-cured specimens achieve higher compressive strength than those dried following initial moist curing [32], whereas others reported that drying enhances compressive strength [33]. However, published studies are difficult to compare since different mix designs, curing methods, and exposure conditions have been used.

The structural performance of AAS concrete is fundamentally determined by its strength and stiffness. As a time-dependent material, concrete undergoes volume changes and develops internal stresses even before any external mechanical loading is applied. Therefore, understanding the evolution of its strength and stiffness over time is essential for ensuring reliable and durable structural performance. These properties are governed by a range of interrelated factors, including the characteristics of the raw materials, mix design parameters, and curing conditions. While most existing studies assess structural performance at the standard 28-day test, there remains a lack in the literature regarding the long-term mechanical behaviour of AAS. Moreover, well-established strategies aimed at improving these aspects have not been sufficiently studied. To enable the practical application of AAS in structural construction, it is essential that the material maintains adequate mechanical properties throughout the intended service life of the structure. Therefore, investigating the development and long-term evolution of strength and stiffness properties is critical. Moreover, it is necessary not only to assess the time-dependent mechanical behaviour of these materials but also to develop effective strategies to enhance or stabilise strength and stiffness throughout their lifespan.

## 1.2. Research aim and Strategy

The primary goal of this thesis is to investigate the causes of the reduction in long-term strength and elastic modulus of AAS and to propose potential solutions.

This research primarily focuses on the following aspects:

- Investigating the mechanism behind the long-term reduction in mechanical properties—namely strength and elastic modulus—of AAS mortars and concrete.
- Evaluating the influence of alkaline activators type, i.e., sodium silicate and sodium carbonate, on the mechanical properties of AAS mortars.
- Assessing the effects of curing regimes, particularly fog curing and ambient curing, on the development of mechanical properties in both AAS mortars and concrete.
- Examining the impact of admixtures—specifically air-entraining agents, gypsum, and shrinkage-reducing admixtures—on the strength and elastic modulus of AAS mortars and concrete.

As a preliminary step, a comprehensive literature review is undertaken to examine existing research on the strength and stiffness development of AAS systems. This review identifies and synthesizes the key factors influencing mechanical properties. Building on the insights gained from the literature, a series of experimental investigations is subsequently conducted to evaluate the mechanical properties of AAS.

## 1.3. Scope

To ensure the research is completed within the given time frame, certain limitations have been placed on its scope. These limitations are as follows:

- Precursor: The investigation is limited to GGBFS as the sole precursor material.
- Alkaline Activators: Two types of activators are considered: sodium silicate and sodium carbonate.
- Admixtures: The study incorporates three specific admixtures: an air-entraining agent, gypsum, and a shrinkage-reducing admixture.
- Sample Type: Both mortar and concrete specimens were used in this study.
- Curing Duration: Tests related to shrinkage, compressive strength, and elastic modulus are performed over a maximum period of six months.
- Curing Regimes: Three curing regimes were investigated: 1) continuous ambient curing, 2) 7-day fog curing followed by ambient curing, and 3) 7-day fog curing followed by sealed curing.
- Water-to-Binder Ratio: A constant water-to-binder ratio of 0.5 is for all mixtures.

## 1.4. Outline of master thesis

The structure of this thesis is outlined in Figure 1.2 and comprises the following chapters:

Chapter 1, introduces the research context by outlining the background, objectives, methodology, and scope of the study.

Chapter 2, provides a comprehensive literature review of the current state of knowledge concerning the mechanical properties of AAM, with particular emphasis on the key parameters and factors affecting mechanical properties and dry shrinkage.

Chapter 3, details the research framework, including the selection of design parameters, material specifications, sample preparation procedures, and the experimental methodologies employed. These elements form the basis of the experimental program designed to achieve the main aim of this master's thesis.

Chapter 4, presents the results of the conducted experiments, which are subsequently analysed and discussed in relation to the main research aim.

Chapter 5, summarizes the principal conclusions of the study and provides recommendations for mitigating dry shrinkage, improving the long-term mechanical properties of AAS for structural applications. Additionally, this chapter outlines potential directions for future research.

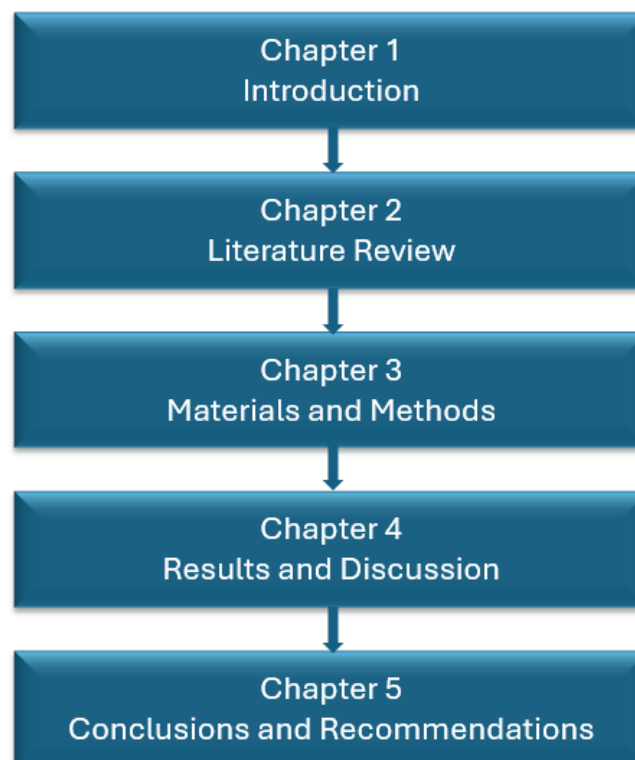


Figure 1.2. : Outline of this thesis.

## Chapter 2

### 2. Literature review on AAM

#### 2.1. Alkali-activated materials

Alkali-activated materials (AAM) have emerged as promising eco-efficient alternatives in the construction sector, primarily due to their reduced environmental impact and ability to incorporate various industrial residues. These materials are synthesized through a chemical transformation initiated by the interaction between an alkaline reagent and aluminosilicate-rich solids, producing a consolidated matrix [34].

A range of industrial derivatives, such as ground granulated blast furnace slag (GGBS), fly ash (FA) [4], silica fume (SF) [35], rice husk ash (RHA) [36], and metakaolin (MK) [37], frequently serve as foundational components for the production of AAM. The growing attention toward these systems is driven by the pressing need to curtail carbon dioxide (CO<sub>2</sub>) emissions linked to conventional Portland cement (OPC) manufacturing, as well as to mitigate issues related to industrial waste accumulation [38].

Consequently, intensified scholarly interest in AAC aims to position it as a replacement for OPC in structural and general construction practices. AAC demonstrate advantageous properties, including enhanced resistance to high temperatures and corrosive environments, extended service life, and mechanical performance comparable to OPC, particularly in compressive strength [39]. Figure 2.1 describes the difference in components between AAC and OPC. This section delves into the roles of alkaline activators, the effects of supplementary additives, and the influence of curing protocols on the performance of AAM.

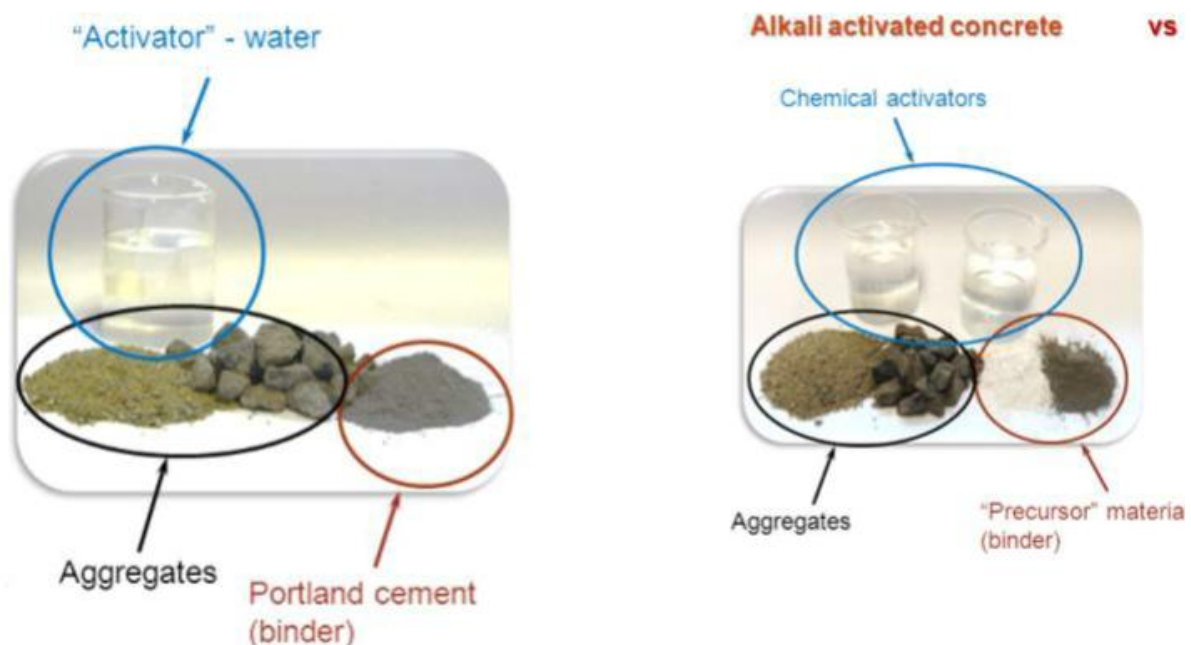


Figure 2.1: Difference between components of AAC and OPC [40].

## 2.2. Precursors

### 2.2.1. Blast furnace slag

Blast furnace slag is a by-product formed during the production of pig iron. In this process, materials like limestone are added as fluxes to help remove impurities from the iron ore. As a result, a molten slag layer forms and rises to the surface above the liquid iron. Once separated, the slag is rapidly cooled, and when it's finely ground, it becomes what's known as ground granulated blast furnace slag (GGBFS).

GGBFS is valued for its latent hydraulic reactivity and its pozzolanic and cement-like properties [41]. Although its exact composition can vary depending on the furnace type and raw materials used, slag produced under consistent conditions in the same system tends to show high uniformity [42]. Table 2.1 provides typical compositional data, showing that slag is generally rich in calcium and silicon.

Table 2.1 summarizes the elemental compositions of both blast furnace slag (BFS) used in this study, determined through X-ray fluorescence (XRF) analysis, as reported by [27].

[%]	SiO <sub>2</sub>	Al <sub>2</sub> O <sub>3</sub>	CaO	Mg	Fe <sub>2</sub> O <sub>3</sub>	SO <sub>3</sub>	Na <sub>2</sub>	K <sub>2</sub>	TiO	P <sub>2</sub> O	L.O.I.
BFS	34.40	11.53	39.17	7.81	1.42	1.60	0.23	0.58	-	-	1.15

One of the most important factors affecting slag reactivity is particle size. Finer particles react more quickly, while larger ones slow the reaction process. In particular, having more particles within the 3–20  $\mu\text{m}$  range has been shown to improve long-term strength [43]. This makes particle size distribution a critical factor in the alkali activation of BFS, influencing how the material sets, gains strength, and develops its internal structure over time [44].

### 2.2.2. Fly ash

Fly ash is a secondary material produced as a consequence of burning coal in power plants during electricity generation. It forms when mineral impurities within coal are exposed to intense heat, causing them to melt and then transform into fine spherical glass particles [45]. These particles, known as fly ash, are transported by the flue gases and later removed using a range of techniques [46].

The activation of fly ash typically involves introducing aqueous alkali hydroxide or alkali silicate solutions to initiate the reaction process. Early-age curing at elevated temperatures—commonly around 40 °C, 60 °C, or 80 °C—is generally required to promote sufficient reactivity. The principal reaction product in alkali-activated fly ash (AAFA) systems is an aluminosilicate gel characterized by a highly cross-linked three-dimensional framework composed of interconnected aluminate ( $\text{AlO}_4$ ) and silicate ( $\text{SiO}_4$ ) tetrahedra, where the negative charge of the structure is counterbalanced by alkali cations [45, 47, 48].

Depending on the substitution of silicon atoms by aluminium within the tetrahedral network, the polymeric chains of  $-\text{Si}-\text{O}-\text{Al}-$  may exist as polysialate (PS), polysialate-siloxo (PSS), or polysialate-disiloxo (PSDS) species [49]. Nevertheless, it has been argued that defining the gel solely through discrete Si/Al ratios oversimplifies the compositional variability inherent in AAFA binders [50]. Therefore, the reaction product is generally referred to as an aluminosilicate gel to encompass the diversity of possible structural configurations.

Fly ash is broadly categorized into Class F and Class C according to ASTM C618, based on its chemical composition and coal source [51]. Class F fly ash, derived from bituminous and

anthracite coals, is low in calcium and rich in silica, alumina, and iron oxides ( $\text{SiO}_2 + \text{Al}_2\text{O}_3 + \text{Fe}_2\text{O}_3 > 70\%$ ), exhibiting primarily pozzolanic behaviour, meaning it reacts with calcium hydroxide from cement hydration to form additional calcium silicate hydrate (C–S–H) that enhances long-term strength and durability [52]. In contrast, Class C fly ash, obtained from sub-bituminous or lignite coals, contains higher CaO content (often 15–30%) and demonstrates both pozzolanic and self-cementitious properties, allowing it to contribute to early strength development [52].

Physically, Class F particles are typically finer and more glassy, improving workability and reducing water demand, while Class C may exhibit more crystalline phases and variable morphology [53]. In terms of performance, Class F generally enhances sulfate and alkali–silica reaction (ASR) resistance due to its low calcium content, whereas Class C, though beneficial for early strength, can be less sulfate-resistant if not properly proportioned [54]. Both types improve long-term durability and reduce permeability by refining pore structure, though their efficiency depends on fineness, loss on ignition, and replacement level. Environmentally, both ashes aid in  $\text{CO}_2$  reduction by substituting cement clinker, but may present trace element leaching risks depending on their chemical composition and disposal conditions. Overall, the distinction between Class F and Class C fly ash is critical for optimizing concrete performance and sustainability in various exposure conditions [53].

### 2.2.3. Slag-to-fly-ash ratio

The effect of slag-to-fly-ash ratio on the mechanical properties of AAM was studied by Wardhono et al. [4], this study found that AAS concrete outperformed fly ash based geopolymer (FAGP) concrete in terms of key mechanical properties, including flexural strength, modulus of elasticity, and compressive strength, as shown in Figure 2.2. At 28 days, AAS concrete showed impressive gains about 40% higher flexural strength, 69% higher stiffness, and 43% higher compressive strength compared to FAGP concrete.

However, while FAGP concrete continued to improve in strength and stiffness over time, AAS concrete began to show a decline in both flexural strength and elastic modulus after the 28-day.

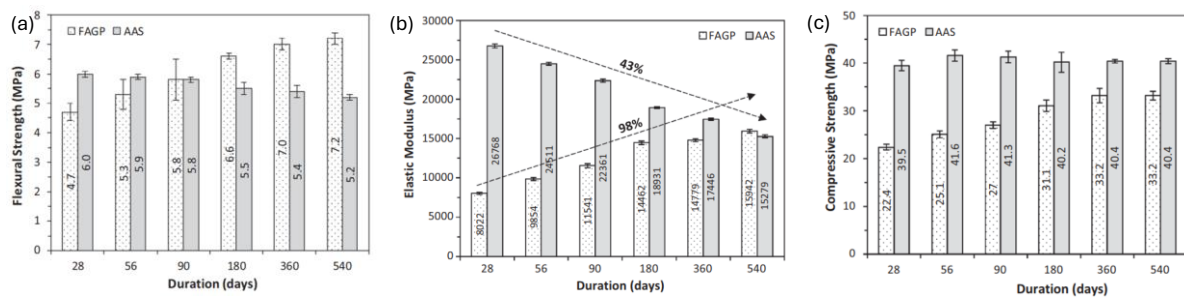


Figure 2.2: (a) Long-term flexural strength, (b) elastic modulus and (c) compressive strength of AAC [55].

Prinsse et al. [27] also examined how partially replacing slag with fly ash affects the mechanical properties of alkali-activated binders. They found that substituting 50% of the slag with fly ash (referred to as the S50 mix) resulted in lower compressive strength and a reduced elastic modulus compared to the mix made entirely with slag (S100). However, despite this drop in performance, the way the mechanical properties developed over time in the S50 blend closely followed the same trend as the S100 mix, as shown in Figure 2.3.

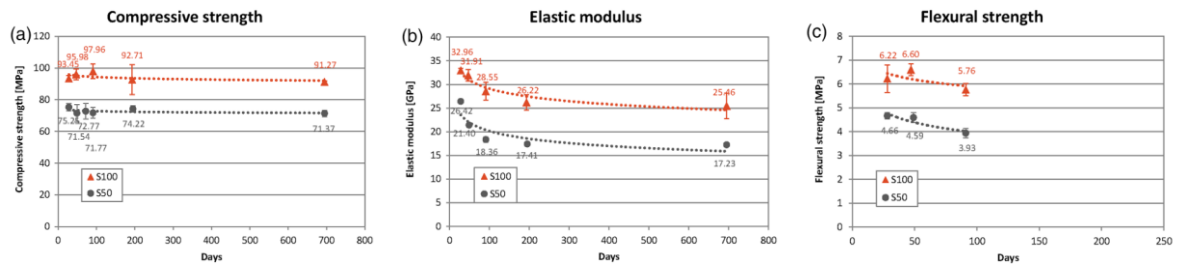


Figure 2.3: (a) Long-term compressive strength, (b) elastic modulus and (c) flexural strength of S100% slag and S50% slag and 50% fly ash [27].

Lee and Lee [56] investigated how replacing fly ash with slag affects the compressive strength of alkali-activated concrete. As shown in Figure 2.4, increasing the slag content from 10% to 15% led to a significant improvement in 28-day compressive strength from 15.5 MPa to 23.0 MPa. This strength gain is mainly attributed to the formation of calcium silicate hydrate (C-S-H) gels and a denser microstructure, both of which result from the presence of slag in the mix.

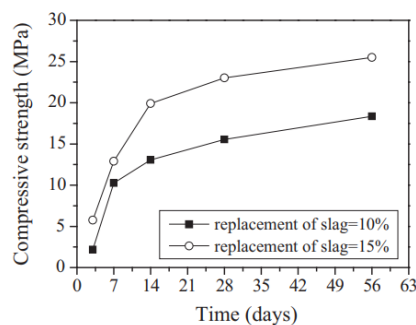


Figure 2.4: Replacement ratio of slag [56].



## 2.3. Alkaline activators

Alkali-activated slag (AAS) binders, derived from ground granulated blast furnace slag (GGBFS) activated with alkaline solutions, have garnered significant attention as sustainable alternatives to traditional Portland cement. The choice of alkaline activator, particularly between solid, liquid sodium silicate, and sodium carbonate plays a pivotal role in determining the both short-term and long-term compressive strengths of AAS.

The microstructure and therefore the performance of alkali-activated slag systems is shaped by several key factors [57]. These include the chemical and mineral makeup of the slag itself, the type and concentration of the alkaline activator used, and the curing conditions applied during processing [58, 59]. Common activators for producing slag-based binders include sodium hydroxide (NaOH), sodium silicate ( $\text{Na}_2\text{O} \cdot r\text{SiO}_2$ ), sodium carbonate ( $\text{Na}_2\text{CO}_3$ ), and sodium sulfate ( $\text{Na}_2\text{SO}_4$ ) [60, 61]. The effectiveness of an activator is largely tied to its ability to create a highly alkaline environment. This high pH is crucial for breaking down the slag particles and triggering the polymerization reactions that lead to binder formation [58, 59]. A strongly alkaline setting typically supports the formation of strength-bearing phases such as calcium–aluminosilicate–hydrate (C–A–S–H) gels [57].

However, pH isn't the only factor that determines how reactive or effective a system will be. Research has shown [62] that sodium silicate solutions even when they have a lower pH than sodium hydroxide solutions with the same  $\text{Na}_2\text{O}$  content can produce binders with better mechanical strength. This improvement is likely due to the extra silicate provided by sodium silicate, which aids in gel development and enhances interparticle bonding through electrostatic interactions [57]. These findings suggest that the specific chemical makeup of the activator particularly its anionic components is just as important as its alkalinity in controlling the reaction processes in alkali-activated slag systems.

### 2.3.1. Sodium Carbonate

Sodium carbonate has been used as an activator for blast furnace slag for more than fifty years in parts of Eastern Europe [57]. It offers a cost-effective and environmentally friendly alternative to more commonly used activators like sodium hydroxide and sodium silicate in producing alkali-activated slag-based materials [63]. Recent studies involving sodium carbonate activated slag concretes especially those incorporating fine limestone have shown encouraging early-age strength results and suggest that greenhouse gas emissions could be reduced by as much as 97% compared to traditional Portland cement systems [64].

One notable benefit of using sodium carbonate is that it produces binders with a lower pH than systems activated by NaOH or sodium silicate ( $\text{Na}_2\text{O} \cdot r\text{SiO}_2$ ) [65]. This makes it especially well-suited for specialized applications, such as encapsulating radioactive waste that contains reactive metals materials that are vulnerable to corrosion in highly alkaline environments [65]. However, despite its advantages, the structural development of carbonate-activated slag is still not well understood. These systems have been relatively under-researched, mainly because of practical challenges like delayed setting times which can stretch to five days and slower strength development compared to other alkali-activated slag mixtures [66].

Early reactions in sodium carbonate–activated slag systems tend to form calcium-based and sodium–calcium carbonate phases, a result of carbonate ions reacting with calcium released from the slag [57]. Over time, the main binding phase shifts toward calcium–aluminosilicate–hydrate (C–A–S–H) gels. Xu et al. [57] observed that aged slag systems activated with sodium carbonate or blends of sodium carbonate and NaOH developed a densely crosslinked C–A–S–H gel, with reduced calcium content near the outer matrix. Interestingly, although calcium–



sodium carbonate compounds like gaylussite were common in 28-day samples, they disappeared in long-term cured specimens [57].

It's been proposed [57] that sodium carbonate activation follows a kind of cyclic hydration mechanism. In this model, the system maintains a buffered alkaline environment through the gradual dissolution of calcium carbonate, which keeps releasing calcium ions into the pore solution. These ions then react with silicate species from the slag to form C–S–H-type gels. However, this mechanism particularly how it unfolds over the first few months remains poorly understood and lacks solid experimental confirmation.

### 2.3.2. Sodium Silicate

Sodium silicate, often referred to as water glass, is a key alkaline activator widely used in geopolymer and alkali-activated binder systems. It primarily consists of sodium oxide ( $\text{Na}_2\text{O}$ ) and silica ( $\text{SiO}_2$ ) dissolved in water, forming a viscous solution. This compound plays a critical role in initiating the polymerization of aluminosilicate materials, such as fly ash and slag by promoting the dissolution and subsequent reorganization of their molecular structure into a solid binder.

The use of solid sodium silicate as an alkali activator plays a significant role in the hydration kinetics and mechanical performance of alkali-activated slag (AAS) systems. In a study by Dong et al. [67], the impact of different dosages of solid sodium silicate on alkali-activated ground granulated blast furnace slag (GGBFS) and fly ash pastes was explored. The research found that an optimal dosage range of 50–110 g per mix improved compressive strength and shortened setting times, enhancing early-age strength. However, using too little or too much sodium silicate had negative effects, disrupting the activation process and reducing compressive strength. The study also looked at how varying the liquid-to-solid ratio (0.20–0.38) influenced strength. It was observed that higher ratios improved workability but compromised mechanical integrity.

Dong's study further compared the compressive strengths of three different activator mixes: liquid sodium silicate (M2), ground sodium metasilicate (M4), and as-received sodium metasilicate (M7) under two curing conditions: ambient and water submersion. Up to 28 days, compressive strengths were similar between ambient- and water-cured samples. However, after 28 days, the strength of the water-cured specimens started to decline, likely due to the leaching of free alkalis, which reduced pore solution alkalinity and destabilized the bonding in the material.

Even though M4 and M7 were chemically similar, M4's finer particle size led to better performance. Both M4 and M7 outperformed M1 and M2 over 90 days. This can be attributed to the partial dissolution of metasilicate particles in the mix, which initially reduced the effective water-to-binder ratio. Over time, undissolved particles absorbed moisture from the environment and gradually released more sodium silicate, further enhancing the material's strength. This trend is shown in Fig. 2.5, where submerged M4 and M7 samples outperformed their ambient-cured counterparts after 28 days. However, excessive undissolved particles, especially in M7, weakened the matrix, resulting in lower overall strength. M7 samples showed compressive strengths 21% lower than those of M4 at 28 days, indicating the negative impact of coarse metasilicate granules.

Notably, M1 showed a drop in conversion rate after three days, followed by a rise at 28 days, likely due to the slow release of hydroxide ions from calcium-based hydration and polymerization, rather than immediate alkali availability. In contrast, the conversion rates for M2 through M20 continuously increased until 90 days, indicating that the slow dissolution of

residual metasilicate particles helped moderate the reaction kinetics during initial mixing. This gradual activation is beneficial for controlling the geopolymerization process [68, 67].

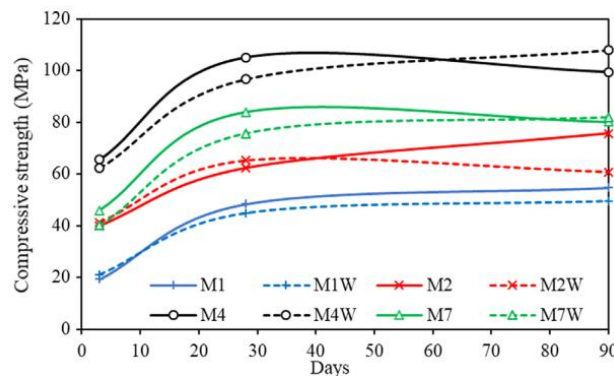


Figure 2.5 : Comparison of mixes with different types of activators and curing conditions [67].

Overall, solid sodium metasilicate provided better early-age performance compared to liquid sodium silicate. The decline in strength in water-cured samples was linked to the inherent instability of sodium-based geopolymer gels in aqueous environments. While additional alkalis helped compensate for lower calcium levels, they also increased porosity in the material.

### 2.3.3. Sodium hydroxide solution

Sodium hydroxide (NaOH) is one of the simplest and most commonly used alkali activators for GGBS, providing a high pH necessary to dissolve the glassy slag matrix, thereby releasing  $\text{Ca}^{2+}$ ,  $\text{SiO}_2$ , and  $\text{Al}_2\text{O}_3$  species. These dissolved species then reprecipitate to form C-(N)-A-S-H (calcium-(sodium)-aluminosilicate hydrate) gels and other secondary phases, which provide binding, strength, and durability [69]. The efficacy of NaOH activation depends on multiple factors, including NaOH concentration (molarity), water-to-solid ratio, slag composition (especially CaO and MgO content), curing conditions (temperature, humidity), and the presence of other activators (e.g., silicates) or supplementary materials (e.g., fly ash) [70]. High NaOH concentrations tend to accelerate reaction rate and early strength development but can raise cost, safety concerns, and risk of efflorescence or excessive shrinkage [71].

NaOH activation primarily functions by elevating pore solution alkalinity ( $\text{pH} > 13$ ), thereby promoting the dissolution of the calcium-, silicon-, and aluminum-rich glassy phases of slag. Dissolved ionic species subsequently reprecipitate to form calcium aluminosilicate hydrate (C-(A)-S-H) gels, which constitute the principal binding phase. These gels differ from Portland cement C-S-H in their higher aluminum incorporation and in chain polymerisation characteristics [72]. Secondary phases, including hydrotalcite-like double-layered hydroxides and AFm-type phases, may also be present, depending on the chemical composition of the slag and the activator concentration [73].

Aimi et al. [74] have reported that a higher sodium hydroxide molarity has been shown to promote strength development, particularly in the range of 6 M to 10 M. This improvement is attributed to the enhanced dissolution of the slag's amorphous phases in highly alkaline environments, which increases the availability of calcium, silicon, and aluminum ions for the formation of reaction products. Manjunath et al. [75] observed that higher molarity accelerates the generation of hydration products, while Sakulich et al. [76] explained that the greater concentration of hydroxide ions facilitates the breakdown of the slag structure, leading to the

formation of intermediary species that ultimately polymerize into calcium–silicate–hydrate (C–S–H) and related binding gels. Nevertheless, when the NaOH concentration exceeds 10 M, a decline in compressive strength is often reported. Fernando et al. [77] attributed this reduction to the complex nature of the hydration process at very high alkalinity, where excessive hydroxide ions impede calcium hydroxide dissolution and favour the formation of sodium-based aluminosilicate phases. This shift in reaction mechanism limits C–S–H gel development and consequently diminishes the overall strength of the AAS matrix.

One of the major limitations of NaOH-activated slag binders is their tendency to exhibit significant autogenous and dry shrinkage. As reported by Sirotti et al. [78], an increase in sodium hydroxide molarity leads to a corresponding rise in dry shrinkage. This behaviour is primarily attributed to the pronounced chemical shrinkage and capillary tension that develop within the fine pore network of the hardened matrix. Higher NaOH concentrations accelerate the reaction kinetics, which intensifies early-age autogenous shrinkage and promotes the formation of microcracks [78].

#### 2.3.4. Potassium hydroxide and silicate

Research on slag activated with potassium-based activators (such as KOH or  $K_2SiO_3$ ) remains comparatively limited when contrasted with sodium-based systems, largely due to the higher cost of potassium compounds. Fernández-Jiménez et al. [79] reported that AAM activated with potassium hydroxide exhibited a lower degree of reaction than that activated with sodium hydroxide. This difference is attributed to the distinct ionic characteristics of  $Na^+$  and  $K^+$ . According to McCormick and Bell [80], the larger ionic radius of potassium promotes the formation of associations with larger silicate oligomers, whereas sodium ions preferentially interact with smaller, monomeric silicate species. Consequently, Na-based activators facilitate a greater release of silicate and aluminate monomers during dissolution, enhancing the reactivity of aluminosilicate precursors. This distinction becomes increasingly important at higher silicate concentrations, where the nature of the cation strongly influences the gel structure and polymerization kinetics [81]. Moreover, potassium-activated aluminosilicate binders generally exhibit a lower tendency toward crystallization compared to sodium-activated counterparts [79]. Provis et al. [82] further demonstrated that sodium-based systems display higher dissolution rates and thus allow the formation of more ordered crystalline products, while potassium-based binders undergo faster polycondensation, leading to less crystalline but more cross-linked structures.

## 2.4. Curing conditions

The curing process plays a vital role in promoting the hydration of precursors in alkali-activated materials (AAM), much like in traditional concrete. Key factors such as relative humidity (RH) must be carefully controlled to optimize chemical reactions and material properties. These conditions are typically applied shortly after the AAM mixture is placed, as they significantly influence the development of the material's strength and durability. The following section explores how these factors impact the progression of AAM development.

### Relative Humidity (RH)

Relative humidity (RH) during curing is one of the most crucial factors in the microstructural development of AAM. The availability of moisture, which is directly influenced by RH levels, governs the duration of the hydration process. Higher RH levels support longer hydration periods, which in turn promote the formation of a stronger matrix. This is typically achieved through moist curing, where an impermeable membrane is used to prevent premature dry, allowing the hydration process to continue and ensuring the desired rate of strength development is maintained [83]. Sealing is another effective method to prevent moisture loss, as it creates a barrier that retains water within the system.

However, even with sealed or moist curing, exposure to environmental conditions particularly low RH environments can still negatively affect AAM. In such conditions, moisture loss can lead to cracking and other issues that hinder the material's development.

A study by Criado et al. [84] on alkali-activated fly ash (AAFA) showed the significant impact of curing conditions on both nano- and microstructural development. When cured at high relative humidity (above 90%) in airtight containers, the material became compact and dense, with improved mechanical properties over time. In contrast, curing under low RH in direct exposure to the atmosphere produced a granular, porous material with stable, aluminium-rich reaction products. While the chemical composition remained similar in both cases, the material exposed to lower RH resulted in a weaker matrix due to its less compact structure.

Liu et al. [85] investigated the influence of various curing regimes on the mechanical behaviour and durability of alkali-activated slag (AAS) mortar. The study examined five different curing environments: ambient conditions (NS\_a) with approximately 55% relative humidity, sealed curing (NS\_s) maintaining 80–95% RH, fog curing (NS\_f) with RH above 95%, full water immersion (NS\_w), and saturated limewater immersion (NS\_l), both at 100% RH. Mortar samples were activated using two alkaline solutions: sodium hydroxide and sodium silicate.

The findings revealed that early-age dry detrimentally affected nearly all measured properties, including compressive strength, elastic modulus, shrinkage, pore structure, carbonation resistance, and freeze-thaw durability. Although sealed curing enhanced strength and durability, it was accompanied by considerable shrinkage. Fog curing and water immersion effectively mitigated early shrinkage but caused leaching issues that compromised long-term durability as can be seen in Figures 2.6 and 2.7. Limewater curing provided only limited improvement relative to other high-humidity techniques. The study underscores the significant role that curing conditions play in optimizing the performance of AAS mortars. Additionally, Figures 2.6 and 2.7 illustrate that ambient curing results in a decline in mechanical properties over time, accompanied by the greatest dry shrinkage and mass variation.

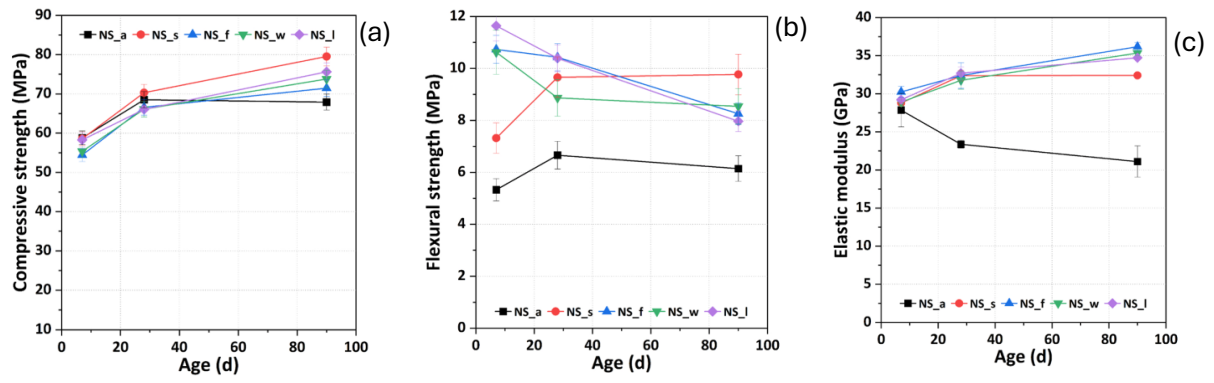


Figure 2.6: Mechanical properties of sodium silicate activated slag mortars under 5 different curing conditions, (a) compressive strength, (b) flexural strength, and (c) elastic modulus [85].

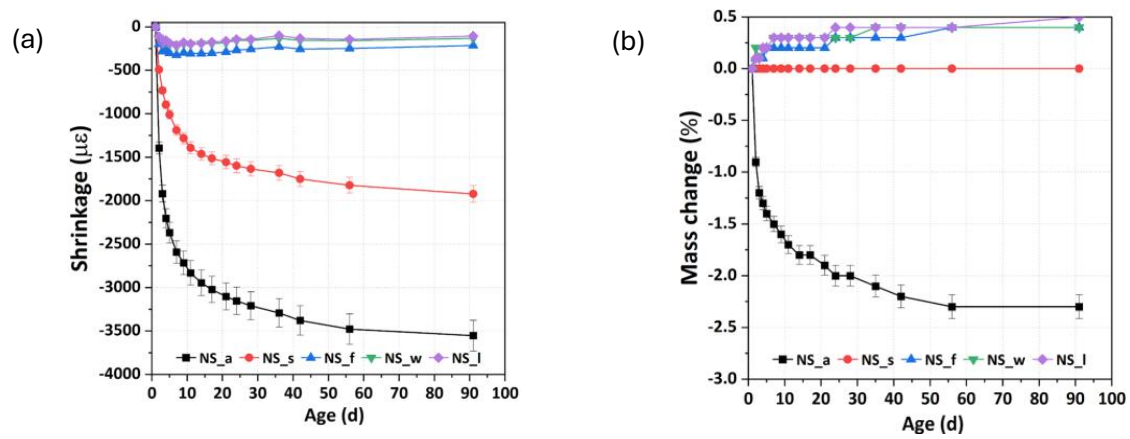


Figure 2.7: (a) Dry shrinkage and (b) mass change of sodium silicate activated slag mortars under 5 different curing conditions [43].

## 2.5. Water content

Previous research consistently demonstrates that increasing the water content in AAS systems generally results in a reduction in compressive strength [79, 86, 87]. Duxson et al. [79] emphasized that excess water weakens the structural integrity of the geopolymeric network, leading to inferior mechanical properties. Similarly, Hardjito and Rangan [86] observed a continuous decline in compressive strength with increasing water-to-solid ratio, independent of the curing temperature as can be seen in Figure 2.8. Microstructural analyses by Škvára et al. [87] further revealed that lower water contents produce a denser matrix with a finer pore size distribution, reflecting a more compact microstructure. Although this trend resembles the well-known behaviour of water in Portland cement systems, the underlying mechanisms differ markedly. In Portland cement, much of the water becomes chemically bound within the calcium–silicate–hydrate (C–S–H) gel, whereas in AAFA binders, water primarily exists as unbound or free water within the pore structure [79]. Moreover, an increase in water content dilutes the alkaline activator, thereby lowering its pH and reducing the dissolution rate of fly ash particles, which limits the formation of reaction products [79].

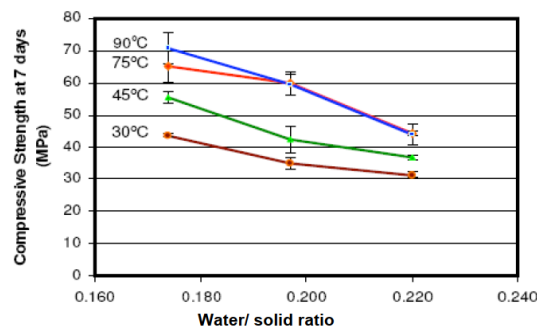


Figure 2.8: Influence of the water-to-solid ratio on the 7-day compressive strength of AAFA concrete specimens [86].

The study of Lee and Lee [56] highlighted the importance of the water-to-solid (w/s) ratio in determining mechanical properties. As illustrated in Figure 2.9, raising the w/s ratio from 0.18 to 0.22 caused a noticeable drop in compressive strength. This underlines how sensitive alkali-activated slag–fly ash concretes are to mix design parameters like water content [56]. To balance workability and mechanical properties, several studies recommend maintaining a low water-to-fly ash ratio—around 0.35—so that sufficient reactivity and a cohesive binder structure are achieved without compromising the mechanical strength.

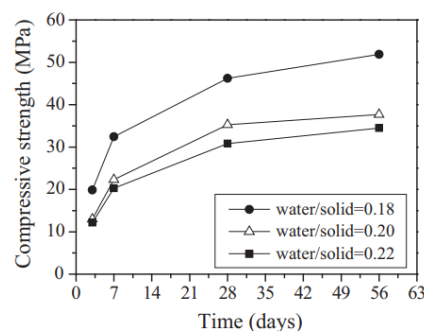


Figure 2.9: Effect of varying the water-to-solid ratio from 0.18 to 0.22 on the compressive strength [56].



## 2.6. Mechanical properties

### 2.6.1. Compressive strength

The compressive strength of AAM provides an important mechanical property which defines the how a material resists axial loads without failure. They are made to react with alkaline solution and form hardened binders. The suitable precursors include aluminosilicate fly ash, ground granulated blast furnace, metakaolin etc. These processes are known as geopolymerization or alkali-activation. The compressive strength development in AAM is influenced by several parameters such as the type of precursor, characteristics of precursor, activator composition and concentration, curing regime, and mix design. AAM can obtain compressive strengths to equal or exceed those of traditional Portland cement-based systems. Thus, they can be used as substitute materials for sustainable and high-performance applications.

Curing conditions play a pivotal role in determining the mechanical properties and microstructural development of alkali-activated slag concrete (AASC). Bakharev et al. [88] reported that heat-cured AASC specimens demonstrated significantly higher early compressive strength (1-day strength) in comparison to those cured at ambient temperature. However, the long-term strength of these heat-cured samples was slightly reduced, as illustrated in Fig. 2.10 (a). This reduction was attributed to microstructural inhomogeneity caused by the disparity between the rates of reaction and diffusion. Specifically, the accelerated hydration reactions led to the accumulation of reaction products near slag grains, leaving interstitial spaces insufficiently filled. The resulting formation of dense precipitates created diffusion barriers, thereby restricting further ion transport and compromising structural uniformity [88].

In contrast, Collins and Sanjayan [29] observed that AASC specimens subjected to bath curing displayed a continuous increase in compressive strength over an extended period, reaching up to 400 days. Meanwhile, specimens cured in sealed conditions exhibited minimal strength gain beyond 91 days. Notably, specimens exposed to ambient air conditions experienced a decline in strength over time, as shown in Fig. 2.10 (b), due to the development of microcracks within the matrix. These findings highlight the susceptibility of AASC to environmental curing conditions. Despite these insights, the influence of different alkaline activators on the long-term compressive strength of AASC has not yet been systematically investigated.

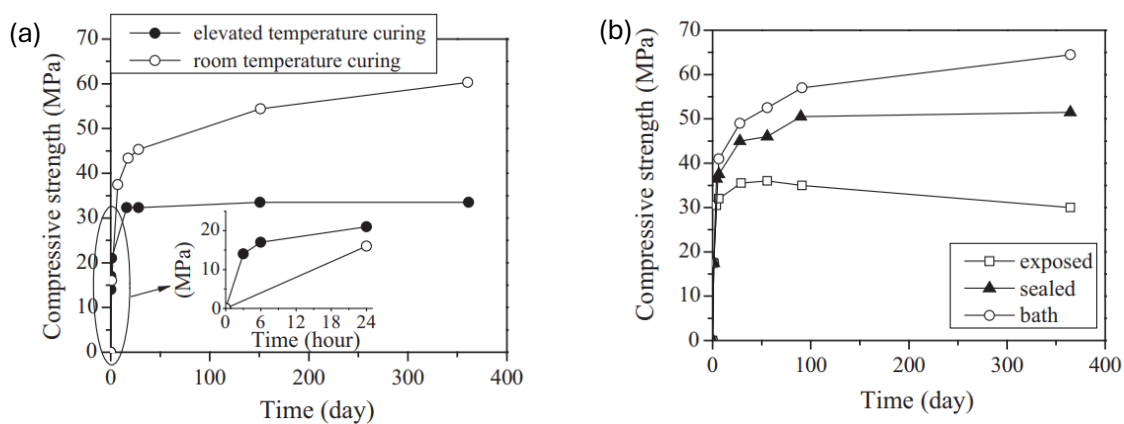


Figure 2.10: (a) Effect of curing temperature on the (a) compressive strength of AASC [88], (b) Effect of curing condition on the compressive strength of AASC [29].

Alkali-activated concrete (AAC) synthesized from fly ash (FA) generally require elevated temperatures curing for attaining sufficient early-age strength, as the activation energy of fly ash is high [89]. According to experimental results, the compressive strength decreases when the water/solids (w/s) mass ratio increases [90]. Here, water means free water and that present in solutions of sodium hydroxide and sodium silicate, while the solids fraction includes fly ash, flakes of sodium hydroxide, and solid content of sodium silicate ( $\text{Na}_2\text{O}$  and  $\text{SiO}_2$ ).

As shown in Fig. 2.11 (a), as the curing temperature increases, the compressive strength also increases but is virtually constant between 75 °C and 90 °C [90]. More studies by Joseph and Mathew [91] had shown that curing temperature could go as high as 100 °C for more strength. Although it was noted that a longer curing period enhanced the strength, the enhancement rate decreased significantly after 48 hours as demonstrated in Fig. 2.11 (b) [90, 91].

More sodium hydroxide will greatly increase the compressive strength [90]. The amelioration is due to the highly alkaline environment created by concentrated NaOH solutions, which result in the depolymerization of amorphous aluminosilicate network of fly ash. The increase in silica and alumina happening due to alkali activation gives rise to the formation of geopolymeric gel phases responsible for strength development.

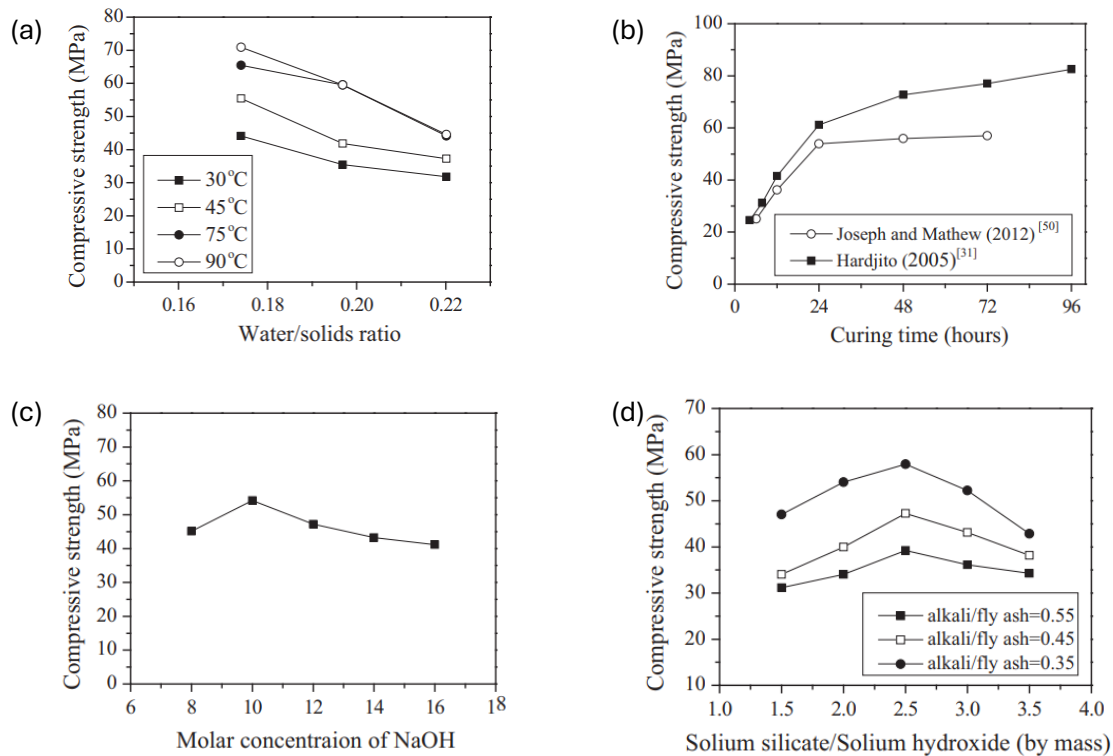


Figure 2.11: (a) Curing temperature and water/solids [61], (b) Curing time [90], (c) Molar concentration of NaOH [91], and (d) Mass ratio of sodium silicate solution [91].



According to a study conducted by Lee and Lee [56], it was looked into the compressive strength of alkali-activated concrete when slag is added by partly replacing fly ash. As shown in Fig. 2.12. According to the results of test 8 (a), 28-day compressive strength increased from 15.5 MPa to 23.0 MPa with increasing slag content from 10% to 15%. The enhancement is primarily due to the formation of calcium silicate hydrate (C–S–H) gel phases and the matrix's microstructure densification as a result of slag having reactive calcium content [92].

An examination of the water-to-solid (w/s) ratio revealed it to be yet another variable affecting mechanical performance. As illustrated in Fig. 2.12 (b), increasing the w/s ratio from 0.18 to 0.22 caused a considerable reduction in compressive strength. The decrease is likely attributed to increased porosity and reduced binder concentration, resulting in a weaker and less dense matrix.

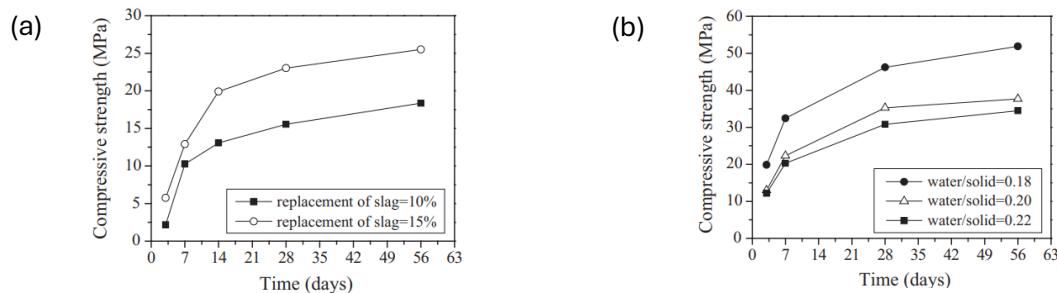


Figure 2.12: (a) Replacement ratio of slag [56], and (b) Water/solid ratio [92].

## 2.6.2. Flexural strength

The flexural strength of AAS materials depends on many interrelated factors that are the precursor type, type and concentration of alkaline activators, curing conditions, sodium hydroxide (NaOH) molarity, mass ratio of sodium silicate solution, and the water to solid (w/s) ratio. This literature review evaluates how these factors affect the early-age performance and long-term development of flexural strength in AAS systems. The studies show what designers focus on when developing mixtures (emphasis on empirical data and mechanistic insight).

### 2.6.2.1. Precursors: Alkali-Activated Slag (AAS)

AAS systems predominantly use GGBFS as their primary binder. The mechanical properties of the binder most greatly impacted by GGBFS chemical composition in terms of the concentration of calcium, silicon and aluminium oxides. Changes in the composition of steel slag may alter the response kinetics and its microstructure developments, which may affect the ultimate flexural strength of AAS systems.

The two image 9 (a) and (b) in reference [4] represents flexural and splitting tensile strength development of AAS and fly ash-based geopolymer (FAGP) concrete from 28 to 540 days. The flexural strength of FAGP concrete improved from 4.7 MPa at 28 days to 7.2 MPa at 365 days, an increase of 53.2%. On the other hand, AAS concrete has a flexural strength of 6MPa at 28 days and reduced to 5.2 MPa at 540 days, which is a decline of 13.3%. Significantly Findings of studies showed that both materials are having similar flexural strength of 5.8 MPa at the 90 days. But FAGP was continuously gaining strength after 90 days while AAS was decreasing marginally.

In terms of splitting tensile strength, AAS and FAGP concretes have lower values than flexural strength. Over a period of 28 - 540 days, the splitting tensile strength of FAGP concrete increases 2.1 MPa to 4.1 MPa, which is about 9 – 12% of compressive strength. While AAS concrete showed higher splitting tensile strength at early ages than FAGP up to 90 days, thereafter FAGP showed a remarkable improvement and attained splitting tensile strength 24.2% greater than AAS by 540 days.

GGBFS serves as the primary precursor in AAS systems. Its chemical composition, particularly the proportions of calcium, silicon, and aluminium oxides, plays a crucial role in determining the mechanical properties of the resulting binder. Variations in slag composition can influence the reaction kinetics and the development of the binder's microstructure, thereby affecting flexural strength.

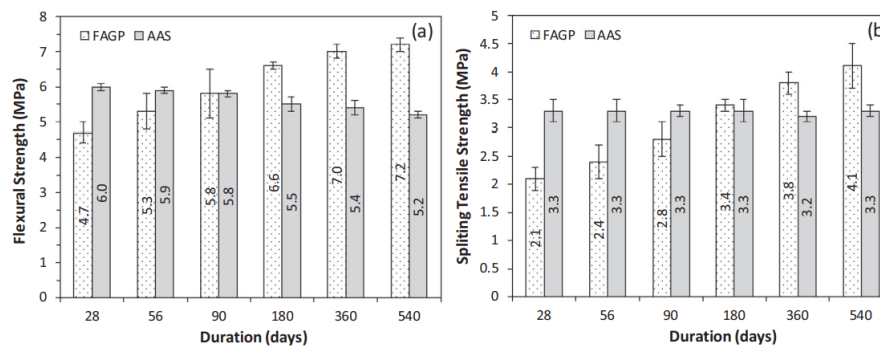


Figure 2.13: (a) Flexural strength and (b) Splitting tensile strength development vs time [4].

The study conducted by [27] investigated the long-term development of flexural and tensile splitting strengths in AAC mixtures. Figure 2.14 (a) illustrates the progression of flexural strength over time for both AAC mixtures. The S100 mixture (containing 0 kg of LCFA and 400 kg of BFS) experienced a 7% reduction in flexural strength between 28 and 91 days, while the S50 mixture (containing 200 kg of LCFA and 200 kg of BFS) exhibited a more significant decline of approximately 15%. Figure 2.14 (b) presents the development of tensile splitting strength for both mixtures. Both AAC mixtures showed a decrease in tensile splitting strength over time. Specifically, the S100 mixture recorded an 11% reduction in tensile splitting strength between 28 and 91 days, while the S50 mixture experienced a more pronounced decline of around 22%. However, the S100 mixture exhibited a subsequent increase in tensile splitting strength at both 193 and 695 days compared to the 91-day values, whereas the tensile splitting strength of the S50 mixture remained relatively stable.

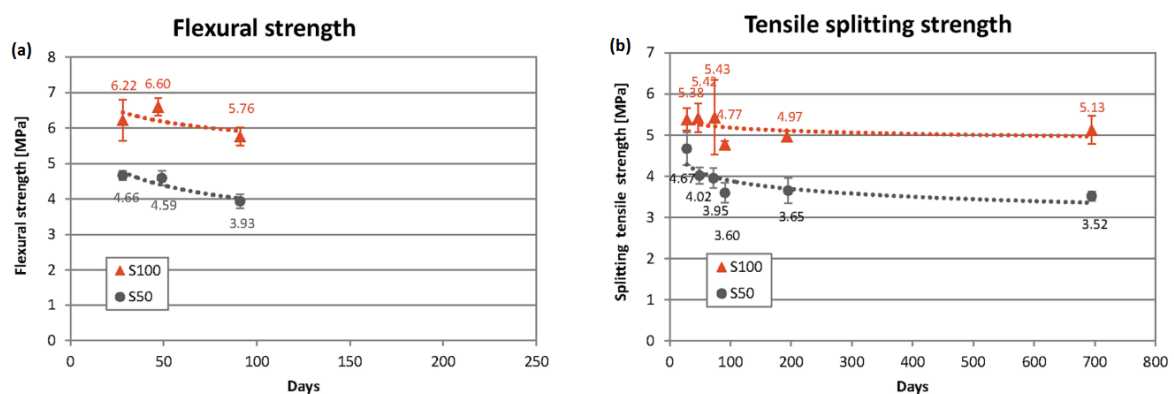


Figure 2.14: (a) Flexural strength and (b) Splitting tensile strength development vs time [27].

### 2.6.2.2. Alkaline Activators: Solid Sodium Silicate, Liquid Sodium Silicate, and Sodium Carbonate

Sodium silicate, whether solid or liquid in form and composition, as activator has considerable influence on the reaction process and properties of AAS. Although no direct comparisons have been made on flexural strength of solid and liquid sodium silicate, sodium silicate is known to be an effective activator. The combination of sodium silicate and sodium hydroxide (NaOH) has been acknowledged to improve the mechanical properties of AAS. Physical forms of sodium silicate have differential influences on flexural strength but more investigation is needed to fully understand its effects.

**Sodium Carbonate:** Several studies resulted in favourable results when sodium carbonate was used as an activator. According to studies, AAS mortars activated with sodium carbonate have a greater compressive strength than those with only NaOH activation. The improved compressive strength suggests that even though there are not many direct comparisons regarding flexural strength, it is likely to enhance the overall performance [93].

The study by Nabil Bella et al. [94] indicates that sodium carbonate concentrations of 1.5% and 2% result in similar short-term and long-term flexural strengths. However, increasing the concentration from 2.5% to 3.5% leads to a reduction in both short-term and long-term flexural strength, as illustrated in Figure 2.15.

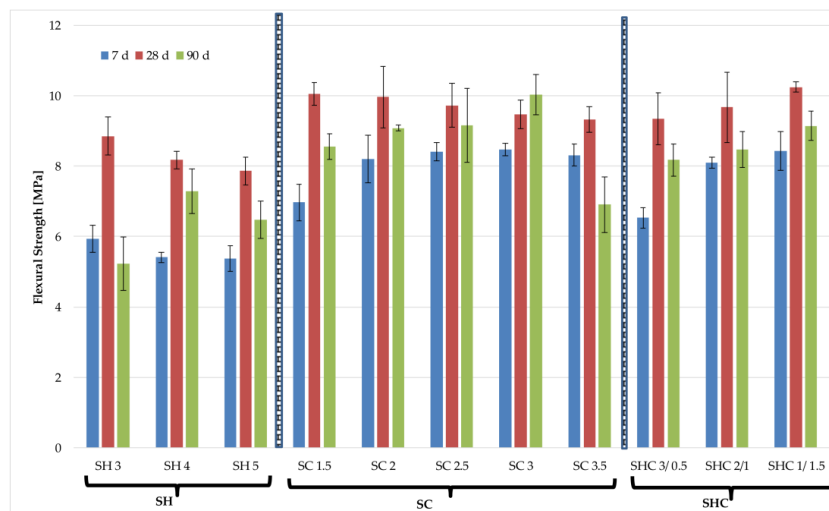


Figure 2.15: Flexural strength of mortars for 3, 28 and 90 curing days [94].

### 2.6.3. Elastic Modulus

The elastic modulus, also referred to as Young's modulus, defines a material's stiffness. It determines its resistance to deformation under forcing stresses. The elastic modulus of alkali-activated materials that form when an aluminosilicate precursor, such as fly ash, slag or metakaolin, is activated with alkaline solutions is influenced by degree of polymerization and microstructure. Most AAM have a greater elastic modulus than Portland cement that can be attributed to the formation of a dense and robust binder network upon activation. As a result of the added stiffness, the AAM can be used for applications requiring "load-bearing capacity", thus making these materials a sustainable alternative to concrete in the engineering field.

Figure 2.16 (a) from the study of [4] illustrates the development of the modulus of elasticity for AAS and FAGP concretes between 28 and 540 days. The modulus of elasticity represents the ratio between a specific range of unit stress and unit elongation within the elastic limit and is indicative of the quality of the concrete specimen. The elastic modulus of FAGP and AAS concretes ranged between 8022-15942 and 26768-15279 MPa, respectively, over the 28 to 540 day period. Notably, the AAS concrete achieved a significantly higher elastic modulus of 26768 MPa at 28 days, compared to an initial elastic modulus of 8022 MPa for the FAGP concrete.

However, the data displays contrasting trends, with the elastic modulus of the FAGP concrete increasing over time, while that of the AAS concrete decreases such that by 540 days, the FAGP concrete has a higher elastic modulus than the AAS concrete. The FAGP concrete exhibits a twofold increase in elastic modulus from 28 to 540 days, whereas the AAS concrete experiences a 43% decrease during this time interval.

The study conducted by [27] investigated the long-term behaviour of the elastic modulus. Figure 2.16 (b) illustrates the trend in elastic modulus for both AAC mixtures. It is apparent that there is a decrease in the elastic modulus over time, with the S100 mixture showing a reduction of approximately 13% and the S50 mixture showing a reduction of about 30% at 91 days. This reduction continues until the age of two years, with the elastic moduli being 23% and 35% lower compared to those at 28 days for S100 and S50 mixes, respectively.

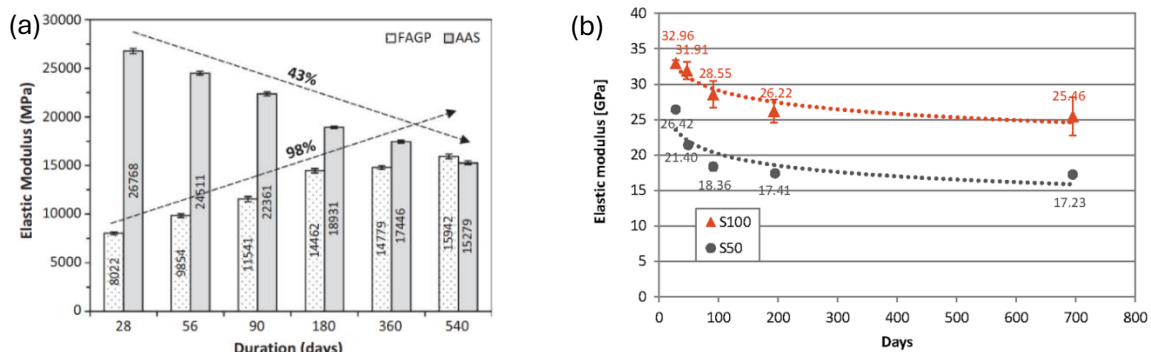


Figure 2.16: (a) Elastic modulus development vs time [27], and (b) Elastic modulus development vs time [55].

## 2.7. Dry Shrinkage

This section introduces the concept of dry shrinkage in alkali-activated materials (AAM), drawing on existing literature to elucidate its underlying mechanisms. The discussion begins with a theoretical overview of dry shrinkage, followed by an analysis of critical factors such as pore size distribution and the properties of binding gels. Particular attention is given to the unique chemical composition and microstructural characteristics of AAM, which distinguish their shrinkage behaviour from that of conventional cementitious systems.

### 2.7.1. Introduction to dry shrinkage

As the low RH (relative humidity) conditions allow moisture to evaporate, the size of cementitious materials is reduced, referred to as dry shrinkage [95, 96]. The time-dependent strain that forms in a specimen during exposure to a constant temperature and which is not restrained nor unloaded and is in both Portland cement (PC) and alkali-activated materials (AAM) [97]. The evaporation of free water takes place due to exposure to drier surroundings this process begins. Moisture loss continues giving rise to internal tensile stresses due to volumetric contraction. If the stresses exceed the strength of the material it cracks [95, 96].

There are various reasons which result in dry shrinkage in cementitious systems. These are the occurrence of capillary pressure, the disjoining pressure, solid surface energy and the migration of interlayer water [97]. In Portland cement at RH greater than 40% capillary pressure is recognized as the major mechanism [97]. This study uses capillary pressure as the main theory for interpreting dry shrinkage, which is further explained in following section.

The following sub-sections deal with the important parameters responsible for dry shrinkage such as pore size distribution, gel structure, mix design, and curing of AAM.

### 2.7.2. Primary concept of dry shrinkage

The capillary pressure theory is among the most widely accepted explanations for dry shrinkage in cementitious systems. It centres on the surface tension that develops along pore walls due to the formation of menisci as water evaporates from the pore network [98]. The capillary stress,  $\sigma_{cap}$ , is quantified using the Kelvin–Laplace equation [99]:

$$\sigma_{cap} = \frac{2\gamma \cos\theta}{r_c} = \frac{-\ln(RH)RT}{V_m} \quad (1.0)$$

Where:

- $\gamma$ : is the surface tension between vapor and pore water,
- $\theta$ : is the contact angle,
- $r_c$ : is the Kelvin radius (curvature of the meniscus),
- RH: is the relative humidity (expressed as a fraction),
- R: is the universal gas constant,
- T is the absolute temperature (in Kelvin),
- $V_m$ : is the molar volume of the liquid.

This equation shows that capillary stress increases as either the pore radius decreases or the ambient RH declines. Therefore, RH and the characteristics of the pore solution are crucial in determining the magnitude of capillary stress within the matrix [99].

As free water evaporates, internal RH drops, leading to the formation of curved liquid–vapor interfaces (menisci) inside the pores. These menisci induce capillary tension that must be counterbalanced by internal compressive stresses. The resulting internal stress causes volumetric contraction in the matrix, manifesting as dry shrinkage [100].

Moreover, Equation (1.0) emphasizes that smaller pores generate higher capillary pressures, intensifying both dry and autogenous shrinkage. As illustrated in Figure 2.17, the deepening curvature of menisci with declining RH reduces the effective capillary radius, thereby amplifying internal stress. In alkali-activated materials (AAM), the typically higher volume fraction of fine pores results in increased capillary tension exerted on the matrix. This phenomenon accounts for the generally greater dry shrinkage observed in AAM compared to conventional Portland cement systems [100].

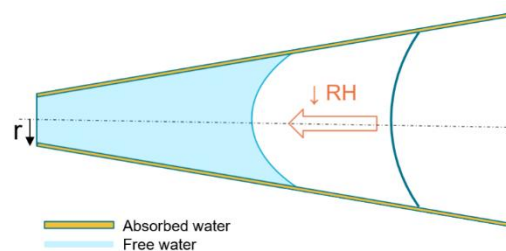


Figure 2.17: Illustrative overview showing the relationship between pore size, RH, and meniscus development during moisture loss [101].

### 2.7.3. Terminology

Dry shrinkage occurs when a material loses moisture to air, typically due to changes in relative humidity (RH). As per ASTM 596, it is defined as a shrinkage in length of a material under no external mechanical force [102]. The dimensions of this material diminish because water moves from the materials to their environment and through chemical changes occurring in the materials during hydration. In the case of materials, shrinkage tends to become worse when exposed for longer periods of time in lower RH environments. Internal stress is set up due to shrinkage when a material is restrained from moving freely, which can lead to cracking [95, 96].

Autogenous shrinkage refers to changes in volume within a material without any moisture loss to the surrounding environment. According to ASTM C1698, it is defined as the bulk strain of a sealed specimen, free from external forces, measured from the final setting time until a specified age [102]. This type of shrinkage happens due to internal dry within the material's microstructure. The mechanisms behind autogenous shrinkage can differ across materials. In Portland cement (PC), it's mainly linked to the evolution of the microstructure, relative humidity (RH), and chemical reactions. On the other hand, studies on alkali-activated materials suggest that autogenous shrinkage isn't driven by the traditional self-desiccation process, but rather by the ongoing reorganization and polymerization of the alumino-silicate gel network [100]. Despite these differences, both materials experience water consumption from hydration products during their chemical reactions.



To sum up, the autogenous shrinkage is caused by hydration reaction taking place within the concrete and consequent self-desiccation while the dry shrinkage is due to the hydration process and loss of water to the environment. Dry shrinkage has mostly been studied under external environmental conditions although both the internal and external dry may be measured [100]. To isolate and better understand the contribution of external dry shrinkage, it will help to isolate (separate) the autogenous one through measurement. As this thesis progresses, the term 'external shrinkage' will refer specifically to the loss of water to the environment surrounding it.

#### 2.7.4. Fundamental Factors Influencing Dry Shrinkage.

The dry shrinkage of both AAM and PC are related to the pore size distribution and the reaction products formed as a result. On the other hand, dry shrinkage mechanism in AAM is inherently more complicated as it is impacted by more number of variables on these mechanisms [95, 96]. In general, AAM are finer than PC. Also, high-calcium, low-calcium, and blended binders differ significantly in this characteristic. Also, dry shrinkage is considerably affected by the formation of the gel phase upon hydration. The solid skeleton in AAM is impacted by these hydration products which influences the mechanical behaviour of the paste [99]. The next sections will highlight the pore size distributions of different binders, and how the gel phase characteristics lead to dry shrinkage.

### 2.8. Dry Shrinkage Mitigation Strategies in Alkali-Activated Materials

Dry shrinkage poses a significant challenge for alkali-activated materials (AAM), often causing cracking and weakening their durability. Researchers have investigated a range of solutions, including different curing techniques, the use of chemical admixtures, choosing the right activators, adding fibre reinforcement, and optimizing the mix design.

#### 2.8.1. Air-entraining agents

Air-entraining agents (AEA) are admixtures that improve the workability and durability of cementitious materials. They help improve the resistance of concrete and mortars to shrinkage cracking. AEAs improve the material's resistance to freeze-thaw cycles and water expansion damage by introducing small air bubbles into the structure of the material. With the improved workability and reduced shrinkage enhancement features of most of the AEA products, the focus on their applications in alkali-activated materials (AAM) is increasing. AEAs can contribute to improving AAM performance. They can also be a good mechanism to help reduce their shrinkage, thus improving the long-term durability of AAM [103].

In essence, air-entraining agents create tiny air bubbles in the AAM mix that create the relief points in the matrix. When water expands, it can cause damage to the final product. This prevents that damage from occurring, so it increases durability and can lead to better strength in the long term. The agents do this by decreasing the surface tension at the water-air interface to allow air bubbles to form and stabilize through a reduction of surface tension [103].

### 2.8.2. Gypsum

The application of gypsum in cementitious systems is indispensable for controlling setting times and improving workability. Gypsum, consisting mainly of calcium sulfate, influences hydration reactions of Portland cement and AAM (alkali-activated materials). Gypsum can affect the hydration products' growth in AAM, enhance early strength, and possibly enhance long-term durability. This research paper examines the role of gypsum in alkali-activated systems with special focus on its impact on the setting time, compressive strength, shrinkage behaviour and performance. By looking into these effects, the aim of the study is to provide an insight into gypsum's potential to enhance the sustainability and practical viability of AAM [83].

### 2.8.3. Shrinkage reduction admixture (SRA)

Shrinkage of a cementitious system can lead to crack formation, reduced durability and other long-term detrimental effects on the structure. These effects may be controlled by introducing shrinkage-reducing admixtures (SRA) to minimize volume changes. These admixtures main function is to reduce the surface tension of pore water. As a result, capillary stresses which cause shrinkage are reduced. The role and efficacy of SRAs (in the context of alkali-activated materials, AAM, it is suggested they could be a sustainable alternative to Portland cement) is still being examined [104]. This research project focuses on the influence of SRAs (shrinkage reducing agents) on the shrinkage mechanism of AAM (alkali-activated materials) and the potential of these additives in improving the dimensional stability (shrinkage resistance) and durability of these emerging binder systems.

### 2.8.4. Fibre Reinforcement

Adding fibres, like polypropylene, steel, or basalt, into alkali-activated material (AAM) mixes provides mechanical support that helps prevent cracks from forming and spreading due to shrinkage stresses. These fibres enhance the material's tensile and flexural strength, allowing it to better resist the stresses caused by dry shrinkage and reducing both the number and size of cracks. Overall, incorporating fibres is a promising way to boost the toughness and dimensional stability of AAM [105].

### 2.8.5. Chemical Admixtures: Naphthalene Formaldehyde Polymers (S) and Water-Reducing Agents (WRRe)

Admixtures like naphthalene formaldehyde-based superplasticizers (S) and water-reducing agents (WRRe) have been shown to help reduce shrinkage, mainly by improving workability and allowing for lower water content in the mix. This leads to a denser, less porous hardened matrix, which in turn helps limit shrinkage. Because AAM have a highly alkaline environment, it's important that these admixtures remain compatible, and recent research confirms they can be used effectively without negatively affecting strength or durability [106].



## 2.9. Literature review on Portland-cement

This review focuses on review literature investigating hardened mechanical properties (compressive strength, flexural strength, elastic modulus) and dry/autogenous shrinkage for Portland-cement systems. It gives special attention to differences caused by curing method (sealed, fog/wet, ambient/dry) and to the roles of the admixtures on the mechanical properties and shrinkage.

### 2.9.1. Portland-cement

#### 2.9.1.1. Introduction

The hydration behaviour of cementitious materials has been a subject of extensive research since the development of Portland cement approximately 150 years ago. When cement particles come into contact with water, the resulting mixture gradually transforms into a solid, stone-like substance that forms the binding matrix of mortar and concrete. This transformation, known as the cement hydration process, involves a series of intricate chemical and physical interactions. The chemical processes govern the formation and transformation of various hydration phases, while the physical processes control the spatial distribution and microstructural evolution of these phases. The final product of hydration is a porous yet rigid solid whose characteristics fundamentally influence the mechanical performance and transport behaviour of cement-based systems [107].

Foundational overviews of cement chemistry were presented in the seminal works of Lea [108] and Taylor [109]. The evolution of microstructural understanding in cement-based materials can be traced to the pioneering investigations of Powers and Brownyard [110], followed by significant contributions from Diamond [111], Scrivener [112], Glasser [113], and Jennings [114]. Continuous advancements in this domain have been systematically documented through the periodic proceedings of the International Congress on the Chemistry of Cement [107].

#### 2.9.1.2. Hydration processes of Portland cement

##### 2.9.1.2.1. The clinker of Portland cement

Portland cement clinker primarily consists of calcium, silicon, and oxygen, with its composition typically reported in terms of the weight percentage of the corresponding oxides. The dominant oxides present in clinker are calcium oxide ( $\text{CaO}$ ), silicon dioxide ( $\text{SiO}_2$ ), aluminum oxide ( $\text{Al}_2\text{O}_3$ ), and iron(III) oxide ( $\text{Fe}_2\text{O}_3$ ). The sintered clinker phase is mainly composed of four crystalline compounds: tricalcium silicate ( $3\text{CaO}\cdot\text{SiO}_2$ , or  $\text{C}_3\text{S}$ ), dicalcium silicate ( $2\text{CaO}\cdot\text{SiO}_2$ , or  $\text{C}_2\text{S}$ ), tricalcium aluminate ( $3\text{CaO}\cdot\text{Al}_2\text{O}_3$ , or  $\text{C}_3\text{A}$ ), and calcium aluminoferrite ( $4\text{CaO}\cdot\text{Al}_2\text{O}_3\cdot\text{Fe}_2\text{O}_3$ , or  $\text{C}_4\text{AF}$ ). To regulate the setting behaviour of cement, gypsum ( $\text{CaSO}_4\cdot 2\text{H}_2\text{O}$ , or  $\text{C}\bar{\text{S}}\text{H}_2$ ) is incorporated during grinding [107].

##### 2.9.1.2.2. Chemical reactions of Portland cement

When Portland cement comes into contact with water, a series of complex chemical reactions commences. Traditionally, investigations into cement hydration have focused on the behaviour of individual, pure cement compounds, assuming that each compound hydrates independently. Although this simplification neglects potential interactions among the hydrating phases—which can significantly influence the overall process—it is often regarded as a reasonable approximation [115]. The hydration mechanisms of pure cement compounds have been systematically detailed by Odler [116] and can be summarised as follows:

1. The hydration of tricalcium silicate ( $C_3S$ ) and dicalcium silicate ( $C_2S$ ) results in the formation of calcium silicate hydrates ( $C-S-H$ ), calcium hydroxide ( $CH$ ), and the liberation of heat.
2. Tricalcium aluminate ( $C_3A$ ) reacts with gypsum in the presence of water to yield ettringite ( $AFt$ ) and heat.
3. The ferrite phase ( $C_4AF$ ) participates in two successive reactions with gypsum. Initially,  $C_4AF$  reacts with gypsum and water to produce ettringite, lime, and aluminum hydroxides.

#### 2.9.1.2.3. Hydration process

The hydration of cement represents an exothermic transformation from a thermodynamically unstable, high-energy state to a more stable, lower-energy configuration, with the surplus energy released as heat [107]. Monitoring the heat of hydration thus provides valuable insights into the chemical and physical processes occurring during cement hydration. A typical heat evolution curve, as illustrated in Figure 2.1, delineates the hydration of Portland cement paste into several distinct stages [107]:

##### 1. Pre-induction period (Stage I)

Immediately upon contact with water, cement particles begin to react. Tricalcium aluminate ( $C_3A$ ) exhibits the highest initial reactivity. During this stage, calcium ions dissolve into the aqueous phase until near saturation, while other ions such as hydroxyl ( $OH^-$ ), sulfate ( $SO_4^{2-}$ ), potassium ( $K^+$ ), and sodium ( $Na^+$ ) are also released into the solution.

##### 2. Dormant period (Stage II)

Following the rapid initial reactions, the system enters a phase of low activity known as the dormant or induction period. This stage typically lasts up to five hours, depending on factors such as temperature, particle fineness, and cement composition. The mechanisms governing this period are commonly explained by the protective membrane theory or the delayed nucleation and growth theory, as discussed by van Breugel [117]. During this phase, the paste remains plastic and workable. The end of the dormant period generally coincides with the initial setting time, which can be determined using the Vicat apparatus [118].

##### 3. Acceleration period (Stage III)

In this stage, hydration reactions intensify and the rate of heat evolution increases, reaching a peak toward the end of the phase. Odler [116] noted that the hydration of  $C_3S$  accelerates considerably, while that of  $C_2S$  becomes more pronounced. Calcium hydroxide crystals precipitate from the pore solution as hydration products accumulate. According to van Breugel [117], ion transport between the liquid phase and the surfaces of unhydrated grains occurs through an increasingly dense shell of hydration products. After approximately 12 hours, this layer reaches a thickness of about 0.5–1.0  $\mu m$ . The final setting of the paste typically occurs shortly before the peak rate of heat evolution, marking the conclusion of Stage III.

##### 4. Post-acceleration period (Stage IV)

During this final stage, the rate of heat release progressively declines as the supply of unhydrated cement diminishes. Formation of calcium silicate hydrate ( $C-S-H$ ) continues, with the contribution of  $C_2S$  hydration becoming more significant over time. This stage reflects the gradual densification and continued microstructural refinement of the hardened cement paste.

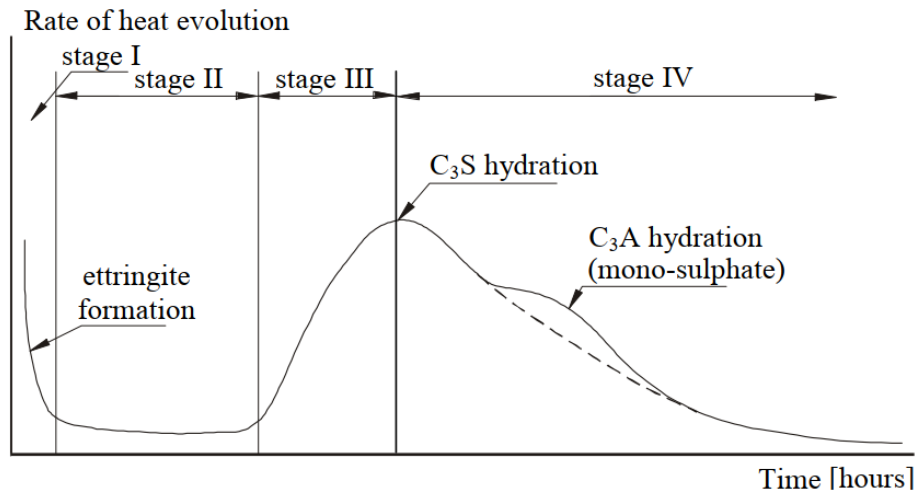


Figure 2.18: Rate of heat evolution during the hydration of Portland cement [107].

#### 2.9.1.3. Development of microstructure in hydrating cement paste

The microstructural evolution of cement paste encompasses the generation of solid hydration products and the development of a connected pore network. The principal hydration products—calcium silicate hydrates (C–S–H), calcium hydroxide (CH), and ettringite (AFt)—along with several secondary phases formed during hydration [119]. These products collectively constitute the binding matrix of the hardened paste and govern the morphology, connectivity, and characteristics of the pore structure. The key features of these hydration products, which play a decisive role in defining the physical and mechanical behaviour of cementitious materials, are outlined below.

##### 2.9.1.3.1. Solid phases

In the early hydration stage, tricalcium aluminate ( $C_3A$ ) reacts rapidly, forming an aluminate-rich gel and short ettringite rods [120]. After the dormant phase, tricalcium silicate ( $C_3S$ ) hydrates to produce “outer” calcium silicate hydrate (C–S–H) and secondary ettringite, followed by the formation of dense “inner” C–S–H. The morphology of C–S–H varies: acicular or fibrous (Type I) and honeycomb-like (Type II) structures form early from  $C_3S$ , while finer, compact forms later arise from  $C_2S$  hydration [119].

Calcium hydroxide (CH) precipitates as large hexagonal crystals in pores, and ettringite appears as needle-like crystals up to 10  $\mu\text{m}$  long [121]. Initially, cement grains are separated by water; as hydration continues, C–S–H and CH connect the grains, forming a dense, continuous solid network that gradually hardens over time.

##### 2.9.1.3.2. Pore Structure and permeability

Hardened cement paste constitutes a porous material, with its pore structure predominantly influenced by the hydration process and the water-to-cement (w/c) ratio. Various researchers have proposed classifications of pore sizes [122], with a consensus generally emerging around three primary categories: gel pores, capillary pores, and entrapped air voids.

##### Gel pore

Gel pores are an inherent feature of the calcium silicate hydrate (C–S–H) phase. They are extremely small, typically ranging from approximately 0.5 nm to 10 nm in diameter, and are beyond the resolution of conventional scanning electron microscopy (SEM). Diamond and colleagues [122] proposed that larger, “open” gel pores ( $\sim 5$  nm) are primarily found in the outer C–S–H product, whereas smaller, “dense” gel pores ( $< 0.5$  nm) are characteristic of the inner

C–S–H product. Based on nitrogen adsorption measurements, Jennings [123] further distinguished C–S–H into two forms: low-density (LD) and high-density (HD). In LD C–S–H, the particle surfaces are accessible to nitrogen, but the interior contains a substantial volume of pores that nitrogen cannot access. Conversely, HD C–S–H has surfaces that are largely inaccessible to nitrogen, with a smaller fraction of internal pores that cannot be probed by this method.

### Capillary pore

Capillary pores arise because hydration products do not completely occupy the space between particles (Figure 2.19 (a)). These pores are significantly larger than gel pores, ranging from approximately 10 nm to 10  $\mu\text{m}$ , with the larger pores being observable under scanning electron microscopy (SEM). Figure 2.19 (b) illustrates a polished surface of a 28-day-old cement paste with a water-to-cement ratio of 0.40, viewed using a backscattered electron (BSE) detector, where capillary pores appear as dark regions. The volume and size of capillary pores are influenced by both the degree of hydration and the initial water-to-cement ratio: they increase with higher w/c ratios and decrease as hydration progresses. It is important to note that the distinction between gel and capillary pores is largely conventional, as pore sizes form a continuous spectrum [107].

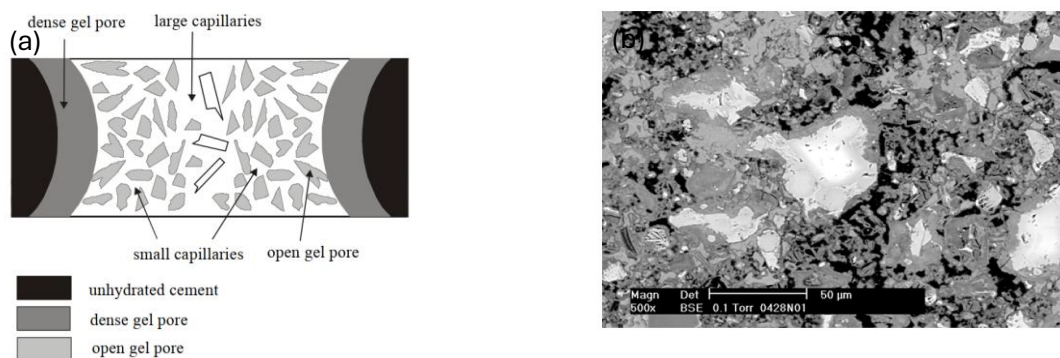


Figure 2.19: (a) Schematic depiction of porosity in cement paste; (b) Capillary porosity in hardened cement paste, with capillary pores indicated as dark areas [107].

Mindess and Young [124] emphasized that capillary pores are primarily responsible for water permeability, a critical consideration when developing permeability models. Key parameters describing pore structure include porosity (volume fraction of pores), pore size distribution, and internal surface area. While these metrics help relate porosity to mechanical strength, they are insufficient to fully characterize permeability. Initially, pores form a continuous network, but progressive hydration gradually isolates portions of the network [122]. The total capillary pore volume strongly affects transport properties, yet the connectivity and tortuosity of the pore network play a more decisive role in controlling water movement through cement paste and concrete [122].

### 2.9.2. Curing conditions

Curing is a critical process in the development of Portland cement-based materials, directly influencing hydration, microstructure formation, and mechanical properties. It involves maintaining adequate temperature and moisture conditions after casting to promote the continued hydration of cement compounds. Inadequate curing can lead to incomplete hydration, higher porosity, increased shrinkage, and reduced durability [124].

### 2.9.2.1. Mechanisms of Curing and Hydration

Hydration is the chemical reaction between Portland cement compounds ( $C_3S$ ,  $C_2S$ ,  $C_3A$ , and  $C_4AF$ ) and water. The hydration products—mainly calcium silicate hydrate (C–S–H) and calcium hydroxide (CH)—occupy the space originally filled by water, thereby strengthening the paste [125].

Curing ensures that sufficient moisture and temperature are available for these reactions. When curing is inadequate, self-desiccation and capillary tension halt hydration prematurely, leaving unhydrated cement grains and interconnected pores [125].

### 2.9.2.2. Types of Curing Conditions

#### 2.9.2.2.1. Water (Wet) Curing

Wet curing involves continuous water exposure (immersion, ponding, or sprinkling). It is the most effective method for maximizing hydration [126].

Studies show that water-cured mortars can achieve up to 40–50% higher compressive strength compared to those cured in dry air at 28 days [126]. Continuous saturation reduces internal drying and maintains high internal relative humidity (>95%), enabling formation of dense C–S–H gel and lower porosity.

#### 2.9.2.2.2. Sealed Curing

In sealed curing, specimens are wrapped or coated to prevent external moisture exchange, maintaining the original water content. Sealed curing mimics autogenous curing, where hydration depends on the initial water-to-cement ratio [127].

At low w/c (<0.40), internal drying can still occur, leading to self-desiccation and incomplete hydration [128]. Sealed conditions typically produce 10–20% lower strength and higher microcracking compared to water curing.

#### 2.9.2.2.3. Air (Ambient) Curing

Ambient curing exposes specimens to environmental conditions without moisture protection. Under ambient humidity (50–70%) and temperature (20–25°C), significant moisture loss occurs in the first few days, limiting hydration [125].

Experimental results indicate that concretes cured in air for 28 days show 25–40% lower compressive strength and up to double the sorptivity compared to continuously water-cured specimens [125]. Air curing also increases surface cracking and carbonation susceptibility.

#### 2.9.2.2.4. Steam and Heat Curing

Steam curing accelerates strength gain by elevating temperature (50–90°C) and maintaining humidity. It is widely used in precast production. However, excessive early heating can cause coarser microstructure, delayed ettringite formation, and reduced later-age strength [129].

Studies show that while 1-day strength can be increased by 2–3 times under steam curing, the 90-day strength may be 10–15% lower compared to moist-cured concrete [129].

Curing affects the evolution of pore structure. Under continuous water curing, total porosity decreases steadily as C–S–H fills capillary pores. Air curing leads to early drying and the preservation of large capillary pores, increasing permeability and chloride ingress [130]. Mercury intrusion porosimetry (MIP) data indicate that well-cured pastes can reduce critical pore diameter from ~0.1  $\mu\text{m}$  to <0.02  $\mu\text{m}$  by 28 days [125].

### 2.9.3. Admixtures for Portland cement

Admixtures — chemical and mineral additions deliberately incorporated into fresh Portland cement concrete or mortar — are essential tools for tailoring workability, setting, strength development, durability, and sustainability. Over the last decades research and industry practice have expanded the palette of available admixtures (water reducers, superplasticizers, retarders, accelerators, air-entrainers, and a wide class of supplementary cementitious materials and novel internal-curing agents), and clarified their mechanisms and practical trade-offs [131].

#### Taxonomy and short definitions

Broadly, admixtures fall into three practical groups:

- Chemical admixtures — polymers and organic/inorganic chemicals added in small dosages to modify rheology, setting, air content or hydration kinetics. Examples: water-reducing agents (plasticizers), high-range water reducers (superplasticizers), accelerators, retarders, and air-entraining agents [132].
- Mineral admixtures / Supplementary cementitious materials (SCMs) — fine powders that partially replace cement or act as pozzolans/latent hydraulic binders (fly ash, silica fume, ground-granulated blast-furnace slag (GGBS), metakaolin, natural pozzolans). These influence heat release, long-term strength, and pore structure [131].
- Functional and emerging admixtures — e.g., superabsorbent polymers (SAPs) for internal curing, nanoparticle modifiers, viscosity modifying agents, corrosion inhibitors, shrinkage-reducing admixtures, and chemical admixtures for SCC. Research on these has grown rapidly in the last decade [133].

#### Mechanisms of action

##### 1) Water reducers and superplasticizers

These work primarily through electrostatic repulsion or steric hindrance, dispersing cement particles and freeing water for workability or permitting water reduction at a given slump. Polycarboxylate ether (PCE)-based superplasticizers give large water reductions and long retention when properly formulated; their adsorption, chain architecture, and interaction with SCMs control performance [131].

##### 2) Air-entraining agents

Detergent-like molecules stabilize microscopic air bubbles in fresh concrete; those bubbles improve freeze–thaw resistance but slightly reduce compressive strength if overdosed. Compatibility with admixtures (especially superplasticizers) needs control [132].

##### 3) SCMs (pozzolanic and latent hydraulic reactions)

Silica fume and reactive pozzolans react with portlandite (CH) forming additional C–S–H, refining pore structure and improving long-term strength, and durability; GGBS contributes a latent hydraulic reaction that improves later strength and sulphate resistance. Effects depend strongly on fineness, amorphous content, and replacement level [134].

##### 4) Superabsorbent polymers (SAPs) and internal curing

SAPs absorb mix water and release it gradually during internal drying, supplying internal curing water to sustain hydration in low-w/c mixes and reduce autogenous shrinkage and early age cracking. Their effectiveness depends on chemical composition, swelling behaviour, and particle size [131].



### Effects on hardened properties and durability

- 1) Compressive strength: Water reduction via superplasticizers raises strength by lowering w/c. SCMs often reduce early strength but increase long-term strength and durability through pozzolanic/latent hydraulic reactions. Silica fume is particularly effective at increasing 28-day strength and refining pores when properly dispersed [135].
- 2) Porosity and transport properties: SCMs and internal curing agents reduce capillary porosity and refine pore size distribution, lowering permeability and chloride diffusion coefficients — a key factor for service life in aggressive environments [136].
- 3) Shrinkage and cracking: Internal curing (SAPs, saturated lightweight aggregates) demonstrably reduces autogenous shrinkage and early cracking in low w/c mixes; shrinkage-reducing admixtures and careful curing practices complement these benefits [137].

## 2.9.3. Mechanical properties

### 2.9.3.1. Compressive strength

The long-term compressive strength of Portland cement concrete, typically assessed at 90 days and beyond, is a critical indicator of structural durability and service life. Unlike early-age strength, which depends primarily on the rapid hydration of  $C_3S$  and  $C_3A$ , long-term strength is governed by continued hydration, pozzolanic reactions, microstructure densification, and pore refinement [138]. Continued hydration of unreacted cement grains produces additional calcium silicate hydrate (C–S–H), filling capillary pores and strengthening the matrix [139].

Supplementary cementitious materials (SCMs), such as fly ash, ground-granulated blast-furnace slag (GGBS), silica fume, and metakaolin, contribute further to long-term strength through pozzolanic or latent hydraulic reactions that consume calcium hydroxide and produce additional C–S–H, thereby reducing porosity and refining the microstructure [140, 141, 142]. The effectiveness of SCMs depends on type, replacement level, fineness, and curing conditions, with high-reactivity materials like silica fume and metakaolin enhancing both early and later-age strength, while fly ash and GGBS typically provide slower early gain but superior long-term performance [143].

### 2.9.3.2. Flexural strength

Usually, concrete is not designed to resist direct flexural. However, knowledge of the flexural strength is needed in order to estimate the load under which cracks will develop. For example, it is useful to understand the cracking behaviour in order to prevent corrosion of reinforcement for reinforced elements [138]. Moreover, the long-term flexural strength of Portland cement concrete is a key property for structural elements subjected to bending, such as beams, slabs, and pavements, as it governs their load-carrying capacity and crack resistance over time. Flexural strength is influenced not only by the compressive strength of the matrix but also by the quality of the interfacial transition zone (ITZ) and microcrack development. Unlike early-age strength, which depends primarily on the hydration of  $C_3S$  and  $C_3A$ , long-term flexural performance is governed by continued hydration, pozzolanic reactions, and microstructure refinement [138].

In ordinary Portland cement concrete, the flexural strength is small when compared to the compressive strength. For AAC, the flexural strength is also small when compared to the compressive strength. However, some studies indicate that AAC shows relatively higher strengths than would be predicted from OPC concretes for similar compressive strength [144, 145, 146].

### 2.9.3.3. Elastic modulus

The long-term elastic modulus of Portland cement concrete is a key mechanical property that indicates the material's stiffness and its capacity to resist deformation under sustained loading, playing a crucial role in structural design and serviceability. While the early-age modulus is largely determined by the initial hydration of  $C_3S$  and  $C_3A$  phases, the long-term modulus is influenced by continued hydration, progressive microstructural densification, and the evolution of both the cement matrix and the interfacial transition zone (ITZ) over time [138]. Ongoing hydration of unreacted cement particles generates additional calcium silicate hydrate (C–S–H), which fills capillary pores and enhances overall stiffness [143].

In conventional OPC concrete, the elastic modulus is also affected by the type and proportion of coarse aggregates. Kameswara Rao et al. [147] demonstrated that the modulus of elasticity can be reliably predicted using the elastic modulus and Poisson's ratio of both the paste and the aggregates. In contrast, alkali-activated concrete exhibits a more complex behaviour, as its elastic modulus is strongly influenced by factors such as raw material composition, microstructural characteristics, and the extent of hydration. Consequently, the stiffness of alkali-activated concrete depends on additional or different parameters compared to traditional OPC concrete [148, 149].

### 2.9.4. Shrinkage

This section seeks to elucidate the shrinkage behaviour of Portland cement concrete by examining its underlying mechanisms. It reviews the potential causes of shrinkage within concrete mixtures and provides an overview of the different shrinkage types, the factors influencing their occurrence, and the fundamental processes that govern them.

#### 2.9.4.1. Types of Shrinkage

Shrinkage in concrete is a time-dependent process characterized by a gradual reduction in volume, primarily resulting from water movement or loss within the material. This phenomenon may arise from internal mechanisms—such as autogenous and chemical shrinkage—or from external factors like water evaporation, which cause drying or plastic shrinkage. When the concrete is restrained during this volumetric change, tensile stresses develop. If these stresses surpass the material's tensile capacity, cracking can occur, compromising both the aesthetic quality and long-term durability of the structure [150].

Generally, three principal types of shrinkage are recognized in concrete due to moisture loss, whether internal or external: plastic shrinkage, autogenous shrinkage, and dry shrinkage. The magnitude of shrinkage strain is closely correlated with the degree of moisture loss [151]. Consequently, shrinkage behaviour is often described in relation to the internal relative humidity of the material. The internal relative humidity of concrete refers to the humidity of the vapor phase that is in thermodynamic equilibrium with the pore solution present in the cementitious matrix [152].

##### 2.9.4.1.1. Initial Saturation of Concrete – Plastic Shrinkage

During the initial 4 to 8 hours after mixing, depending on the mixture composition and ambient conditions, concrete remains in a plastic or semi-fluid state [153]. Plastic shrinkage occurs when the rate of water evaporation from the surface exceeds the rate of bleeding—the upward movement of pore water. This imbalance causes the evaporation of capillary water, generating tensile stresses within the surface layer of the fresh cement paste. To mitigate plastic shrinkage, measures such as proper curing, shading the surface to reduce temperature rise, and scheduling placement during cooler periods of the day are typically adopted to minimize moisture loss.



In freshly mixed concrete, water coats the cementitious particles, forming a continuous liquid film that imparts workability and fluidity to the mixture. During casting, this water occupies the voids within the solid skeleton, creating a fully saturated system where the internal relative humidity is approximately unity, as illustrated in Figure 2.20(a). At this stage, the material behaves as a viscous fluid with minimal structural rigidity, resulting in large volumetric deformations but negligible internal stresses [150].

### Influencing Factors

Plastic shrinkage is primarily governed by the rate of evaporation, the extent of the exposed surface area, and the effectiveness of the curing method employed. The evaporation rate itself is influenced by several environmental parameters, including ambient relative humidity, concrete surface temperature, and wind velocity. Higher evaporation rates and larger exposed surface areas intensify moisture loss, thereby increasing the likelihood of plastic shrinkage and the subsequent risk of surface cracking [150].

#### 2.9.4.1.2. Autogenous shrinkage

During hydration, the total volume of cement and water is greater than that of the resulting hydration products, which possess a higher density than the original constituents—a process known as chemical shrinkage [154]. In the early liquid phase, this internal volume reduction occurs freely because the material has no structural rigidity to resist deformation. Once the setting point is reached and a solid microstructure begins to form, further hydration causes changes in internal porosity without producing significant external volume change [155]. However, as hydration progresses, continuous water consumption alters the internal moisture balance, influencing overall shrinkage behaviour.

Autogenous shrinkage refers to the unrestrained deformation that occurs in sealed concrete at constant temperature [156]. This phenomenon arises because the reduction in pore volume lags behind the rate of water consumption, leaving partially empty pores. The resulting internal moisture depletion—termed self-desiccation—leads to a drop in internal relative humidity, as illustrated in Figure 2.20. The loss of capillary water generates tensile stresses within the pore structure, while the surrounding hydration products experience compressive stresses.

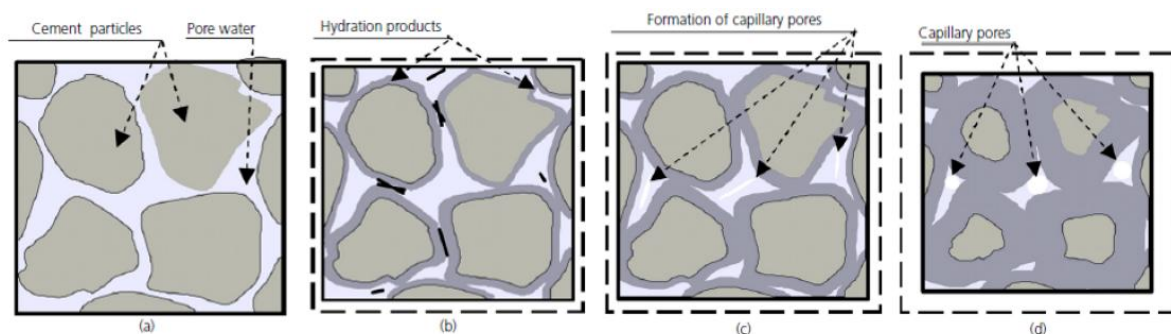


Figure 2.20: Schematic illustration of the microstructural evolution in cement paste: (a) Freshly mixed cement paste, (b) Setting stage, (c) Onset of capillary pore formation, and (d) Reduction in internal relative humidity [150].

Autogenous shrinkage occurs uniformly throughout the concrete matrix and is particularly critical during the early stages of hydration, when the mechanical properties—such as elastic modulus and fracture energy—are still developing. This early-age shrinkage can induce cracking, which negatively affects both the strength and durability of the concrete. Numerous studies [157, 158, 159] have examined the evolution of internal relative humidity over time as a result of self-desiccation.

Zhang et al. [159] investigated the distribution of internal relative humidity in ordinary Portland cement (OPC) concrete cubes ( $150 \times 150 \times 150 \text{ mm}^3$ ) with varying water-to-cement (w/c) ratios under sealed conditions. Similarly, Kim Lee et al. [157] performed experiments on smaller cubes ( $100 \times 100 \times 100 \text{ mm}^3$ ) under both sealed and unsealed conditions. Specimen with a w/c ratio of 0.30 (N30) exhibited a relative humidity reduction to approximately 85% after 28 days. The extent of internal humidity reduction was found to decrease with increasing w/c ratio, a trend also observed in the work of Jiang et al. [158].

Autogenous shrinkage is primarily governed by the intrinsic material characteristics of concrete, including the degree of binder hydration, and cement content. Several additional parameters significantly influence this behaviour:

#### Influencing Factors

Cement type and fineness: The incorporation of highly reactive supplementary cementitious materials, such as silica fume, tends to intensify autogenous shrinkage. This occurs because finer materials produce a denser pore network, leading to higher capillary stresses as water is depleted from smaller pores. Jennings et al. [160] demonstrated that increased cement fineness accelerates the hydration process, thereby reducing internal relative humidity more rapidly and amplifying shrinkage effects.

Curing temperature: Experimental findings by Bentur et al. [161] revealed that higher curing temperatures promote a coarser microstructure due to an accelerated hydration rate. The formation of larger capillary pores under these conditions results in lower capillary tension, which can partially mitigate autogenous shrinkage.

Aggregate effect: The presence of aggregates reduces autogenous shrinkage compared to that of pure cement paste with the same w/c ratio. This reduction is attributed to the restraining influence of aggregates and the lower cement content per unit volume, as reported by previous studies [162].

#### 2.9.4.1.3. Dry shrinkage

When concrete is subjected to a dry environment, it naturally seeks moisture equilibrium with its surroundings. As the cement paste undergoes drying, the internal pore relative humidity progressively declines, leading to a reduction in the curvature radius of the liquid menisci. Initially, evaporation occurs more rapidly in the larger pores connected to the exposed surface because of the higher humidity gradient. This early stage of moisture loss has minimal impact on overall volume change. As drying progresses, smaller pores that are linked to already-emptied voids begin to lose moisture, further reducing internal humidity levels.

Dry shrinkage commences once the final setting of concrete has occurred and exposure to a dry atmosphere begins. The magnitude of shrinkage increases rapidly at first and then continues to develop at a diminishing rate over the following months or years. Experimental investigations by Kim Lee et al. [157] examined variations in internal relative humidity and the associated dry shrinkage using concrete specimens of  $200 \times 100 \times 100 \text{ mm}^3$ , prepared with water-to-cement ratios of 0.28 and 0.40 and stored at 50% relative humidity and  $20^\circ\text{C}$ . Their findings indicated that relative humidity values were higher at greater depths from the exposed surface, demonstrating a moisture gradient across the specimen.

The principal parameters influencing dry shrinkage include environmental exposure, structural geometry, curing conditions, and aggregate content [150]:

**Environmental conditions:** The rate and extent of drying are primarily determined by ambient factors such as relative humidity, temperature, and wind velocity. A larger difference in relative humidity between the internal pore system and the surrounding air accelerates moisture diffusion as the system seeks equilibrium.

**Structural geometry:** The size and shape of the concrete member significantly affect the drying rate. Slender or thin elements dry faster than massive sections under identical conditions. Moreover, steep moisture gradients typically develop near the exposed surfaces compared to the inner core regions.

**Curing conditions:** The quality of curing not only governs early-age moisture retention but also influences the evolution of the pore structure. Adequate curing minimizes premature drying, promotes continuous hydration, and results in a denser and more durable microstructure.

**Aggregate content:** Similar to autogenous shrinkage behaviour, the presence of aggregates restrains dry shrinkage deformation. An increased aggregate-to-cement ratio provides greater internal restraint, thereby reducing overall shrinkage strain.

A concise overview of the different shrinkage mechanisms, their development periods, and the main influencing parameters is presented in Table 2.2.

Table 2.2: Summary of shrinkage types, development duration, and governing factors.

Type of Shrinkage	Typical Development Period	Primary Influencing Factors
<b>Plastic Shrinkage</b>	Initial few hours after casting	Curing practices, environmental conditions, , cement fineness and composition, and aggregate content
<b>Autogenous Shrinkage</b>	Several days to weeks	
<b>Dry Shrinkage</b>	Months to several years	Environmental conditions (relative humidity, temperature, and air flow), structural geometry, curing quality, and aggregate proportion

#### 2.9.4.2. Mechanisms Governing Shrinkage

Shrinkage in concrete primarily results from two concurrent processes: self-desiccation during cement hydration and moisture evaporation from pore spaces. Both mechanisms contribute to a reduction in internal relative humidity, which induces volumetric contraction. Moisture transport within the cement matrix predominantly occurs through the diffusion of water vapor across interconnected pore networks [163].

As hydration progresses or as water migrates out of the concrete, the reduction in pore water leads to the development of curved liquid–vapor interfaces (menisci), thereby lowering the internal relative humidity. The extent of this humidity decrease is directly proportional to the amount of moisture lost. Over several decades, extensive research has established a clear correlation between relative humidity reduction and shrinkage behaviour. Three principal theoretical models have been developed to explain the underlying mechanism:

1. Surface tension change, which arises due to curvature of the menisci in capillary pores;
2. Disjoining pressure, resulting from molecular interactions within thin water films; and
3. Capillary tension, caused by negative pressure in the liquid phase within unsaturated pores.

These mechanisms collectively describe the physical origin of autogenous and dry shrinkage in cement-based materials.

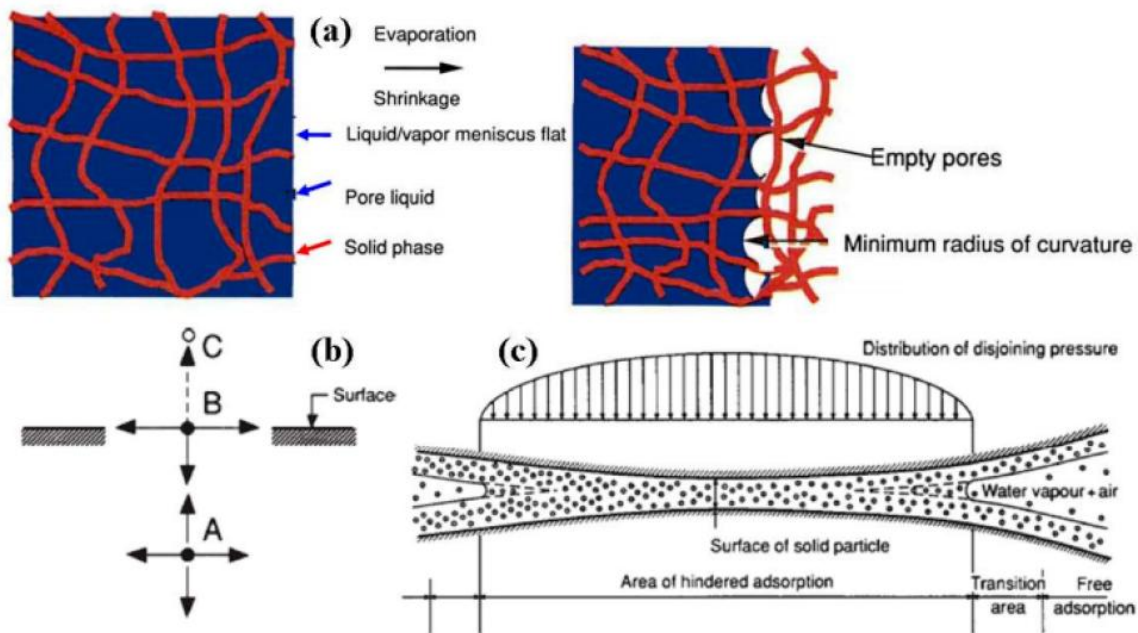


Figure 2.21: Schematic representation of the principal mechanisms contributing to shrinkage in concrete: (a) Capillary tension generated by meniscus formation within partially saturated pores; (b) Surface tension forces acting on molecule A within the solid matrix in equilibrium with molecule B at the surface, producing compressive stress; (c) Disjoining pressure resulting from molecular interactions in the confined adsorption layer. Adapted from [164].

#### 2.9.4.2.1. Surface Tension of Solid Gel Particles

In the solid gel structure, asymmetrical intermolecular forces near the surface generate surface tension. As the internal relative humidity decreases, the adsorbed water layer surrounding the solid particles becomes thinner, leading to an increase in surface tension and a consequent volumetric contraction of the cement paste. This mechanism is particularly associated with autogenous shrinkage and is considered effective primarily under low humidity conditions—typically when the internal RH drops below 40%, and in some cases, down to approximately 20% [165].

#### 2.9.4.2.2. Disjoining Pressure

Disjoining pressure arises within thin liquid films confined between solid surfaces due to molecular interactions such as van der Waals forces, electrostatic repulsion, and structural ordering effects. When the relative humidity decreases, the liquid film separating adjacent solid particles becomes thinner, increasing the disjoining pressure and thereby inducing compressive stress in the solid matrix. This mechanism contributes to shrinkage primarily at very low relative humidity levels, often below 40%, and is regarded as a key factor in nanoscale moisture–solid interactions within hardened cement paste [165].

#### 2.9.4.2.3. Capillary Tension Mechanism

In partially saturated cementitious materials, the liquid within the pores forms curved menisci as moisture evaporates, establishing a pressure difference between the liquid and vapor phases—known as capillary pressure. This negative pressure (tensile stress) in the pore fluid exerts compressive forces on the surrounding solid matrix, producing elastic shrinkage strains. The capillary tension mechanism dominates in moderate to high relative humidity conditions, typically above 40%, and serves as the principal explanation for dry shrinkage in concrete [150].

## 2.10. Knowledge gaps in long-term mechanical research

Although considerable research has been conducted on AAS systems, significant gaps remain in understanding the mechanisms responsible for the long-term reduction of mechanical properties (particularly compressive strength, flexural strength, and elastic modulus) in AAS mortars and concrete. Most existing studies have focused primarily on short-term strength development or on individual factors such as raw materials or curing regimes in isolation. There is still limited knowledge regarding the long-term mechanical properties of AAS across multiple material scales, and the influence of dry shrinkage on long-term properties remains unclear. Furthermore, well-established strategies to prevent reductions in long-term mechanical properties have not been sufficiently investigated.

To address these research gaps, a multi-scale experimental approach is adopted, progressing from paste to mortar and finally to concrete:

Paste scale: X-ray diffraction (XRD) analysis is employed in this study to elucidate the relationship between phase evolution and the long-term reduction of mechanical properties in AAS systems. Specifically, XRD provides critical information on the crystalline and semi-crystalline phases formed during hydration, their transformation over time, and their stability under varying curing regimes. By identifying reaction products, XRD helps to verify the mechanisms inferred from mechanical and shrinkage data. Furthermore, XRD allows comparison between sodium silicate- and sodium carbonate-activated binders, revealing how differences in phase assemblage influence dry shrinkage and long-term mechanical properties. Thus, XRD analysis provides the microstructural evidence necessary to link chemical phase transformations to the observed macroscopic mechanical degradation and validate the proposed reaction mechanisms underlying strength evolution and shrinkage behaviour.

Mortar scale: Studying the mortar scale is essential for bridging the gap between paste-level microstructural behaviour and concrete-level structural performance. At this scale, the effects of activator type, curing regime, and admixtures on mechanical properties can be systematically evaluated, while capturing phenomena such as microcracking, shrinkage, and aggregate–matrix interactions that are not evident in paste alone. Analysis of mortars allows researchers to link microstructural changes observed at the paste level to measurable reductions in mechanical properties, providing insight into mechanisms that also influence concrete performance. Additionally, the smaller size of mortar samples makes them easier and more cost-effective to prepare and test. Mortar studies therefore, enable optimization of the mix design, which can then be applied in subsequent concrete investigations to ensure efficient and reliable scaling of results.

Concrete scale: Mortar-based investigations offer valuable preliminary insights for optimizing mix design; however, concrete testing is crucial to assess performance under realistic conditions. Examining both mortar and concrete systems enables a comprehensive understanding of AAS behaviour, ensuring their reliable and practical application in structural engineering contexts.

By systematically progressing through these scales, the methodology ensures that the observed trends and mechanisms at the microstructural level are correlated with the mechanical behaviour at larger, application-relevant scales. This integrated approach not only addresses the identified research gaps but also provides a robust framework for proposing potential solutions to mitigate the long-term reduction in strength and stiffness of AAS systems.



### Benefits of using alkali-activated concrete

Ordinary Portland cement (OPC) systems often exhibit deterioration under chemically or physically aggressive conditions, limiting their service life in certain applications [166]. In contrast, numerous studies have demonstrated that alkali-activated binders possess superior durability characteristics, including enhanced resistance to freeze–thaw cycles and improved chemical stability in acidic environments [167]. A practical illustration of this advantage can be seen in the Netherlands, where alkali-activated concrete was used for the floor of a milk-powder production facility requiring exceptional acid resistance. The previous OPC-based floor demanded frequent replacement, while the alkali-activated alternative provided significantly greater longevity, highlighting its suitability for industrial environments exposed to aggressive agents [168].

In addition to durability, alkali-activated systems are capable of achieving high mechanical strength more efficiently than conventional OPC concrete. Wang et al. [167] reported that alkali-activated slag concretes can attain compressive strengths of 70–120 MPa, while offering cost savings of 10–40% and reductions in coal consumption of up to 80% compared to high-strength OPC concretes incorporating silica fume. Furthermore, AAC, particularly low-calcium geopolymers, exhibit superior fire resistance relative to OPC concretes. After exposure to temperatures between 800 °C and 1000 °C, OPC concretes typically retain only 20–30% of their original strength due to microstructural breakdown and dehydration [169]. In contrast, the porous structure of alkali-activated binders allows moisture to escape more effectively, mitigating thermal damage and preserving residual strength.

Nevertheless, the performance of alkali-activated concrete is highly dependent on its chemical composition and processing conditions. Unlike OPC systems, where most properties can be tailored by adjusting the water–cement ratio, alkali-activated binders are influenced by multiple variables, including the type of precursor (slag, fly ash, or their blend), the nature and concentration of the alkaline activator, and the curing regime. Each combination of materials yields a distinct reaction pathway and microstructural evolution, resulting in significant variability in mechanical and durability performance. Therefore, a comprehensive understanding of how mixture design parameters govern the mechanical properties of AAC remains essential for optimizing its use in construction applications.

## Chapter 3

### 3. Approach & Methodology

#### 3.1. Materials

This section describes the Ground Granulated Blast Furnace Slag (GGBFS) as well as the various chemical admixtures and alkaline activators that were used in the experimental program. Moreover, it includes details about mix proportions, mixing, and specimen preparation.

The main binder used in this study was GGBFS, which was obtained from Ecocem Benelux B.V. The GGBFS was tested for chemical composition using XRF, and the results are given in Table 3.1. The chemical analysis of the slag shows the oxides present in the slag that influence the reactivity of the AAM. Due to its potential to form a long-lasting and sustainable binder when activated with an alkaline solution, GGBFS can be used in place of Portland cement, as is the case in the present study [170].

Table 3.1: The chemical composition of the Blast Furnace Slag (BFS) used in this study was determined through X-ray fluorescence (XRF) analysis [47].

[%]	SiO <sub>2</sub>	Al <sub>2</sub> O <sub>3</sub>	CaO	Mg	Fe <sub>2</sub> O <sub>3</sub>	SO <sub>3</sub>	Na <sub>2</sub>	K <sub>2</sub>	TiO	P <sub>2</sub> O	L.O.I.
BFS	34.40	11.53	39.17	7.81	1.42	1.60	0.23	0.58	-	-	1.15

Two distinct alkaline activators were utilized in this investigation. The first is sodium metasilicate, characterized by a silica-to-sodium oxide (SiO<sub>2</sub>/Na<sub>2</sub>O) molar ratio of 1.0. The second activator is high-purity sodium carbonate (99–100%), also employed with a modulus (Ms) ratio of 1.0.

Three types of chemical admixtures were incorporated into the mixtures: an air-entraining agent (AEA), gypsum (G), and a shrinkage-reducing admixture (SRA). The AEA was added at dosages of 0.6%, 1.2%, and 1.8% [171]. Gypsum was introduced at concentrations of 4%, 6%, and 8% [171], while the SRA was also applied in proportions of 0.6%, 1.2%, and 1.8% [172].

#### 3.2. Mix Design

All mixtures were prepared with slag and a constant water-to-binder (w/b) ratio of 0.5, Na<sub>2</sub>O 4% and a silica modulus (Ms) of 1.0. The alkali-activated mortar and concrete mixture compositions are presented in Tables 3.2 and 3.3, respectively.

Table 3.2: Alkali-activated mortars mixtures.

	Slag	Na <sub>2</sub> SiO <sub>3</sub> · 5H <sub>2</sub> O (g)	Na <sub>2</sub> CO <sub>3</sub> (g)	Water (g)	Zand (g)	w/b
NS	1000	163.74	0.00	411.95	2500	0.5
NC	1000	0.00	68.37	500	2500	0.5



Table 3.3: TU Delft alkali-activated concrete mixtures [168].

For 1 m <sup>3</sup> concrete:	[kg]
Slag	400
Sand (0-4 mm)	761
Gravel (4-8 mm)	441
Gravel (8-16 mm)	521
Na <sub>2</sub> SiO <sub>3</sub> · 5H <sub>2</sub> O	54,8
w/b ratio	0.5

### Curing conditions

In addition, two distinct curing regimes were employed in this study. The first regime involved ambient curing (A), conducted under laboratory conditions at a relative humidity (RH) of approximately 55% and a temperature of 20 °C, representing typical field or indoor environments where moisture loss is not controlled. The second regime was fog curing (F), performed at 95% RH and 20 °C for up to seven days, followed by continued exposure to ambient laboratory conditions.

Fog curing was selected to minimize early-age moisture loss and mitigate dry shrinkage, which are known to be particularly high in alkali-activated slag systems, compared to PC due to their rapid reaction kinetics and dense gel formation [173, 174, 175]. Moreover, AAS produces a different binding gel (C–A–S–H with lower Ca/Si and different pore structure), has much larger autogenous/chemical-shrinkage components and a pore system that makes capillary-tension and carbonation effects far more sensitive to ambient RH, fog (very high RH/wetting) changes the AAS reaction path and moisture/ion transport more strongly than it does for OPC [173, 174].

The subsequent ambient exposure facilitates the evaluation of long-term mechanical properties under realistic drying conditions, which more closely reflect those encountered in engineering practice.

### Admixtures

AAS exhibits high early strength, but its practical application is often limited by high shrinkage and poor workability. To address these issues, admixtures commonly used in ordinary Portland cement (OPC) systems have been tested for their effectiveness in improving the performance of AAS mortars and concretes [171]. The selection of admixtures in this study is based on the findings of Bakharev et al. [171], who investigated the effects of a superplasticizer based on modified naphthalene formaldehyde polymers (S), an air-entraining agent (AEA), a water-reducing admixture (WRR), a shrinkage-reducing admixture (SHR), and gypsum (G) added at 6% of the slag weight. The results of Bakharev et al. showed that AEA, SHR, and G significantly reduced dry shrinkage. Based on these findings, AEA, G, and SHR were selected for use in the present study to mitigate the shrinkage of AAS mortar. Based on the experimental results on AAS mortar, the admixture that most effectively reduces the AAS mortar dry shrinkage will be selected for use in the subsequent AAS concrete mixtures.

The nomenclature adopted in this study includes abbreviations such as NS (sodium silicate), NC (sodium carbonate), AEA[x] (air-entraining agent), G[y] (gypsum), and SRA[z] (shrinkage-reducing admixture), where x, y, and z denote the dosage percentage of the corresponding admixture.

### Comparison with OPC

For reference, two ordinary Portland cement concretes (OPCCs) were included in this study to enable direct comparison with the AAS systems. The reference mixtures were selected based on information from the literature. The first reference mix consisted of a high-strength concrete produced with CEM I, designed to achieve a compressive strength comparable to that of the AAS mixture [176]. The second reference mix is CEM III, which contains a high proportion of ground granulated blast furnace slag (GGBFS) [168].

The overall mix design is illustrated in Figure 3.1, while the types and dosages of admixtures are shown in Figure 3.2.

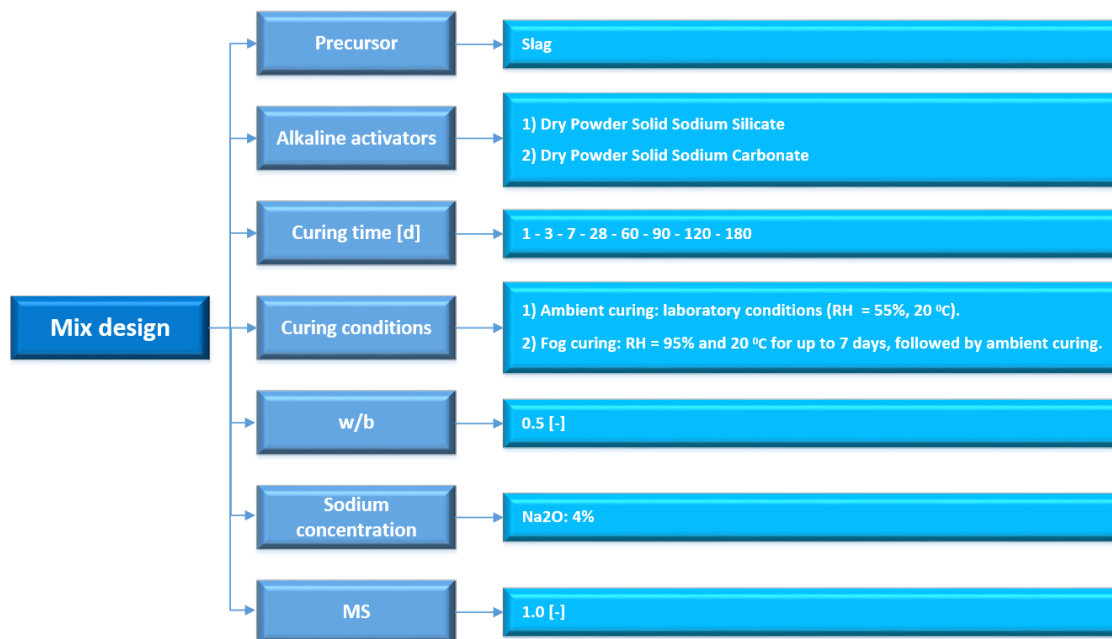


Figure 3.1: Mix design

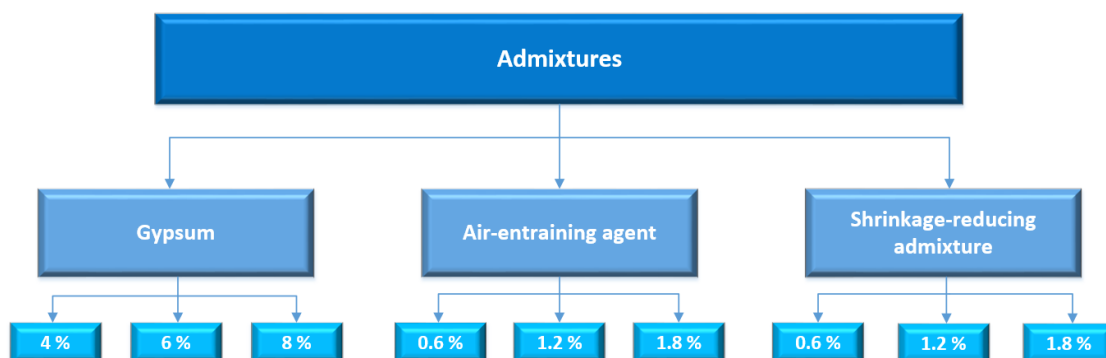


Figure 3.2: Admixtures

In this study, a total of 40 unique mixture combinations were initially designed, incorporating two types of alkaline activators, two curing conditions, and three admixture types—each applied at three dosage levels. The corresponding number of specimens required for mechanical and shrinkage testing amounted to approximately 4800 samples, based on the planned combinations for compressive strength, flexural strength, elastic modulus, and dry

shrinkage measurements across multiple curing ages. To ensure experimental feasibility, the program was refined by identifying the two most effective admixtures and their optimal dosages based on findings from the literature.

According to Bakharev et al. [171], gypsum was the most effective in mitigating long-term dry shrinkage, followed by the air-entraining agent (AEA), and then the shrinkage-reducing admixture (SRA). Additionally, Bakharev et al. [171] have demonstrated that the optimal gypsum content is approximately 6%, as this proportion fosters the highest formation of ettringite (AFt) and monosulfate (AFm) phases. When the gypsum dosage exceeds this level (such as at 8% or 10%), the available gypsum becomes fully consumed, resulting in the absence of residual gypsum and a noticeable reduction or disappearance of AFt and AFm phases. Moreover, several shrinkage-reducing admixtures (SRAs) have been reported to exhibit adverse side effects, such as a reduction in mechanical strength, when incorporated into AAMs [177, 178, 179]. For instance, Bilek et al. [180] investigated the influence of a hexylene glycol-based SRA on AAS mortar and observed a notable decline in compressive strength. Similarly, Collins and Sanjayan [173] introduced an SRA into AAS concrete to mitigate dry shrinkage; however, the admixture failed to delay cracking because it concurrently reduced the material's tensile strength.

Consequently, the experimental matrix was streamlined by excluding mixtures containing SRA and omitting the 8% gypsum level. The revised plan retained sodium silicate-activated mixtures incorporating the selected admixtures and sodium carbonate-activated mixtures without admixtures. This refinement reduced the total number of mixtures from 40 to 14, as summarized in Table 3.4.

Table 3.4: Number of mixtures

MIX no.	Alkaline activators	Curing condition	AEA [%]	G [%]	SRA [%]	MIX no.	Alkaline activators	Curing condition	AEA [%]	G [%]	SRA [%]
1	NS	Fog				1	NC	Fog			
2	NS	Fog	0.6			2	NC	Fog	0.6		
3	NS	Fog	1.2			3	NC	Fog	1.2		
4	NS	Fog	1.8			4	NC	Fog	1.8		
5	NS	Fog		4		5	NC	Fog		4	
6	NS	Fog		6		6	NC	Fog		6	
7	NS	Fog		8		7	NC	Fog		8	
8	NS	Fog			0.6	8	NC	Fog			0.6
9	NS	Fog			1.2	9	NC	Fog			1.2
10	NS	Fog			1.8	10	NC	Fog			1.8
11	NS	Ambient				11	NC	Ambient			
12	NS	Ambient	0.6			12	NC	Ambient	0.6		
13	NS	Ambient	1.2			13	NC	Ambient	1.2		
14	NS	Ambient	1.8			14	NC	Ambient	1.8		
15	NS	Ambient		4		15	NC	Ambient		4	
16	NS	Ambient		6		16	NC	Ambient		6	
17	NS	Ambient		8		17	NC	Ambient		8	
18	NS	Ambient			0.6	18	NC	Ambient			0.6
19	NS	Ambient			1.2	19	NC	Ambient			1.2
20	NS	Ambient			1.8	20	NC	Ambient			1.8

### 3.3. Experimental methods

#### 3.3.1. Alkaline-activated slag paste

##### 3.3.1.1. Mixing and curing

The required quantities of slag (Table 3.2) were accurately weighed and dry-mixed for 2 minutes to ensure homogeneity. Subsequently, the alkaline activator solution was gradually added while mixing at low speed. This was followed by an additional 1 minute of mixing at low speed and 1 minute at high speed to achieve a uniform paste. The resulting mixture was then cast into moulds, sealed to minimize moisture loss, and cured under the conditions specified in Section 3.2. The casting process is illustrated in Figure 3.3.

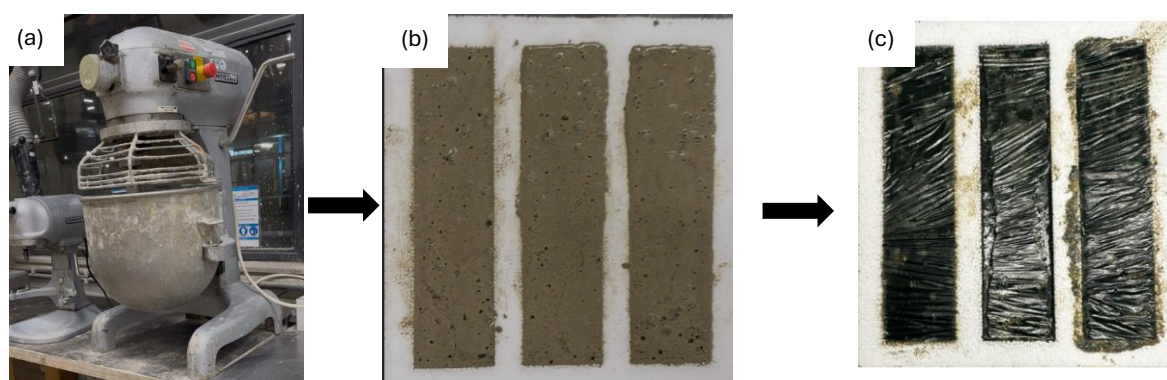


Figure 3.3: (a) Casting of AAS mortar, (b) placement into moulds, and (c) appearance of the specimen one day after casting.

To prepare the samples for X-ray diffraction (XRD) analysis, finely ground powder was made from the AAS pastes, with hydration stopped using a solvent exchange technique [181]. The process began by grinding the samples in a mortar with isopropanol to prevent carbonation. After about 30 minutes of grinding, the mixture was left to rest for 15 minutes to ensure the solvent fully replaced the water. The slurry was then filtered through paper using a vacuum pump. During filtration, the samples were rinsed multiple times with absolute ethanol, followed by a wash with diethyl ether to speed up drying. At this point, the powder looked almost dry. Finally, the powder was placed in a Petri dish and dried in an oven at 40 °C for 10 minutes before being stored in a vacuum desiccator until the XRD tests. These careful preparation steps removed free water from the samples, preserving only the chemically bound water necessary for accurate phase analysis [182].

##### 3.3.1.2. XRD measurement

XRD analysis was performed using a Bruker D8 Advance diffractometer with a CuK $\alpha$  radiation source ( $\lambda = 1.54 \text{ \AA}$ ). The solvent-exchanged powder samples were scanned across a  $2\theta$  range of 5° to 70°, using a step size of 0.02° and a dwell time of 5 seconds per step. These settings were chosen to ensure accurate peak detection and reliable phase identification [182].

#### 3.3.2. Alkaline-activated slag mortars

##### 3.3.2.1. Mixing and curing

The required quantities of sand and slag were accurately weighed and introduced into the mixing bowl of a Hobart mechanical mixer. The dry components were blended for 2 minutes to ensure uniform distribution. Subsequently, the alkaline activator was gradually added while

the mixer operated at its lowest speed, followed by 1 minute of mixing. Water was then added slowly under continued low-speed mixing for an additional minute. Finally, the mixture was blended at high speed for 2 minutes. The freshly prepared mixture was subsequently cast into moulds and subjected to vibration using a vibration table to eliminate entrapped air and ensure proper compaction.

- For samples requiring ambient curing, allow curing in laboratory air conditions at room temperature until being tested.
- For samples under fog room curing, cure samples in a controlled humidity environment with relative humidity above 95% up to 7 days. Thereafter, ambient curing until being tested.

### 3.3.2.2. Mechanical properties measurement

The mechanical properties were evaluated using the following testing procedures: a three-point bending test was performed on three specimens from each mix, in accordance with the NEN-EN 196-1 standard [183]. The tests were carried out using a hydraulic testing machine, applying a constant loading rate of 0.05 kN/s, with an initial load of 0.1 kN and a termination load set at 20% of the expected maximum load. Each specimen was positioned on the supports and loaded at mid-span to evaluate flexural performance as can be seen in Figure 3.4 (a).

Following the flexural testing, the fractured halves of each prism were used for compressive strength testing, also in accordance with NEN-EN 196-1 [183]. These tests were conducted at a loading rate of 2.4 kN/s, with a start load of 1 kN and a stop load of 20%. For both flexural and compressive strength evaluations, the average of the maximum recorded values from the three specimens was taken as the representative strength for each test. The compressive strength test set-up is given in Figure 3.4 (b).

The static elastic modulus was determined using a universal testing machine in combination with a compressometer/extensometer setup (Figure 4.3 (c)), applying a loading rate of  $0.6 \pm 0.2$  MPa/s, as prescribed by NEN-EN 12390-13:2021 [184]. More detailed information regarding the testing procedures for determining the elastic modulus can be found in Annex A.

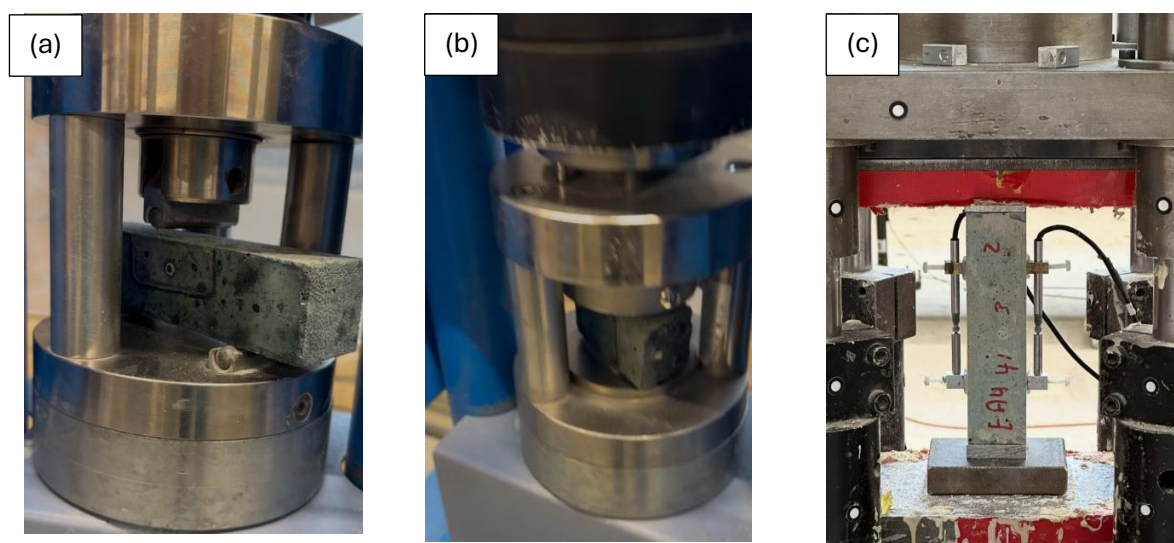


Figure 3.4: Experimental setups for mechanical testing: (a) three-point bending test, (b) compressive strength test, and (c) elastic modulus setup.



### 3.3.2.3. Dry shrinkage and weight loss measurement

Dry shrinkage can be evaluated under either restrained or unrestrained conditions. In this study, unrestrained shrinkage was examined, allowing the specimens to deform freely along their longitudinal axis without external constraints. Measurements began immediately after the designated curing period had concluded.

Length changes were tracked using a digital comparator with a measurement accuracy of 0.001 mm. The initial length of the specimen ( $L_0$ ) was established by subtracting the first recorded value from the nominal length of 160 mm. Linear dry shrinkage was then calculated based on Equation 3.1.

$$\varepsilon_L = \frac{L_t - L_0}{L_0} \quad (3.1)$$

With:

- $L_t$  = the length at time  $t$  [mm]
- $L_0$  = initial length, 160 - first measurement [mm] .

### Weight Loss

In addition to tracking shrinkage, the specimens' mass was monitored to assess moisture loss over time. The initial mass ( $m_0$ ) was defined as the specimen's weight at the end of the curing period. At each measurement interval, the current mass ( $m_t$ ) was recorded using a high-precision balance with an accuracy of 0.1 g. The percentage of moisture loss was calculated using Equation 3.2.

$$\Delta m = \frac{m_0 - m_t}{m_0} \times 100\% \quad (3.2)$$

With:

- $m_t$  = the mass at time  $t$  [g]
- $m_0$  = initial weight [g]

Figure 3.5 illustrates the experimental setup used for the measurement of dry shrinkage.

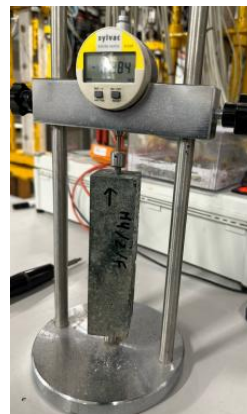


Figure 3.5: Dry shrinkage setup.

### 3.3.3. Alkaline-activated slag concrete

Mortar studies provide valuable preliminary insights and serve as an effective platform for mix design development. However, to reliably evaluate structural performance and long-term durability under real-world conditions, it is essential to validate these findings in concrete. A combined assessment of both mortar and concrete enables a more comprehensive understanding of AAS systems and supports their practical implementation in structural applications.

The most effective mix design will be initially selected based on the results of mortar samples under various curing conditions, types of activators, and admixtures. This optimized mix will subsequently be used for the preparation of concrete specimens. Following this, the differences in performance between AAS mortars and concrete will be analysed and discussed in detail.

#### 3.3.3.1. Mixing and curing

During the mixing process, the dry constituents—comprising slag, fine aggregate, and coarse aggregate—were first blended for 3 minutes to ensure uniform distribution using a 40L concrete mixer. Following this, the alkaline activator solution was gradually introduced into the dry mixture. For mixes requiring gypsum, 6% gypsum (by binder mass) was added one minute later after the activator. Mixing was then continued for an additional 3 minutes to obtain a homogeneous and workable composite. The fresh alkali-activated concrete (AAC) displayed limited workability and exhibited signs of rapid setting shortly after mixing.

The freshly prepared AAC was then placed into pre-oiled moulds positioned on a vibrating table. For the initial casting batches, oil was applied to the moulds. However, Vaseline was subsequently used in later batches due to its superior demoulding performance.

Each mould was filled in two layers. After filling the mould halfway, the mixture was compacted by vibrating for approximately 20 seconds. The remaining material was then added, followed by a second vibration cycle of equal duration to ensure proper consolidation. Once filled, the moulds were covered with plastic film to prevent moisture loss during the initial setting phase. After 24 hours, the specimens were demoulded after 24 hours and cured under fog conditions for 7 days (20°C and 95% RH), followed by ambient exposure (20°C and 55% RH) until the testing day.

#### 3.3.3.2. Mechanical properties measurement

Three-point bending tests were conducted in accordance with NEN-EN 14651+A1, with a modification to the specimen dimensions. Instead of the standard prism size (150 × 150 × 550–700 mm<sup>3</sup>), reduced-size specimens measuring 100 × 100 × 400 mm<sup>3</sup> were used. Testing was performed using an Instron universal testing machine in the Microlab at TU Delft (Figure 3.6 (a)), operating at a constant displacement rate of 0.5 µm/s. The flexural strength was calculated based on the maximum load recorded during the test, in accordance with Equation 3.3:

$$f_{flex} = \frac{M}{W} = \frac{\frac{1}{4} F \cdot L}{\frac{1}{6} b \cdot h^2} \quad (3.2)$$

With:

$f_{flex}$  = Flexural tensile strength [MPa]

$M$  = bending moment [Nmm]

$W$  = section modulus [mm<sup>3</sup>]

$F$  = Applied load [N]

$L$  = Span length between supports [mm]

$b$  = Width of the specimen [mm]

$h$  = Height of the specimen [mm]



Compressive strength tests were conducted in accordance with NEN-EN 12390-3, with a deviation from the standard specimen geometry. Instead of cylindrical samples, cube specimens measuring  $100 \times 100 \times 100 \text{ mm}^3$  were used. These cubes were obtained by wet-sawing the central section of prisms previously subjected to flexural testing. Prior to testing, all specimens were dried for a minimum of two hours. The tests were carried out using a CYBER-TRONIC compression testing machine in the Macrolab at TU Delft (Figure 3.6 (b)), with a constant loading rate of 6.5 kN/s. The compressive strength was calculated by dividing the maximum load sustained by the specimen by its loaded surface area.

The elastic modulus was determined in accordance with ISO 1920-10:2010, with a minor deviation from the standard procedure—specifically, the specimens were not re-immersed in water for 12 hours prior to testing. The specimens measured  $100 \times 100 \times 400 \text{ mm}^3$ , yielding a height-to-width ratio of 4, which meets the dimensional requirements specified in the ISO standard.

Vertical displacements were captured using four LVDTs mounted on each specimen. The tests were conducted using the TONI-BANK testing machine at the TU Delft Macrolab (Figure 3.6 (c)). The specimens were initially loaded in displacement-controlled mode until a stress level of 5 MPa was reached. The control mode was then switched to strain-controlled loading at a rate of 0.001/s, continuing until one-third of the previously measured compressive strength was achieved. This loading cycle was repeated one or two times, depending on the test setup.

The LVDT measurements provided force–displacement data, which were converted into stress–strain curves. The elastic modulus was calculated via linear regression between the stress levels of 5 MPa and one-third of the maximum compressive strength.

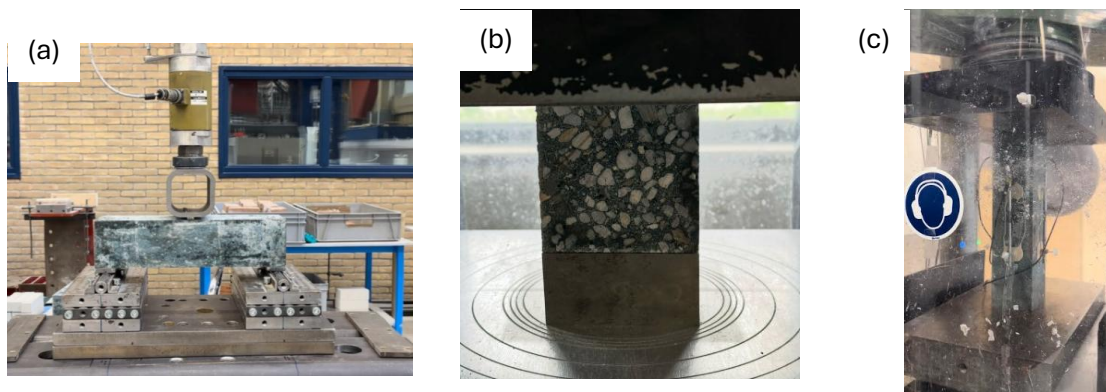


Figure 3.6: Experimental setups for mechanical testing: (a) three-point bending test, (b) compressive strength test, and (c) elastic modulus setup. Note: The photograph in Figure (a) was taken during the preparation of the experimental setup and not during the actual testing period.

#### 3.3.3.3. *Dry shrinkage measurement*

The dry shrinkage of the concrete was measured according to the procedure described in section 3.3.2.3. Figure 3.7 illustrates the experimental setup used for the measurement of dry shrinkage.

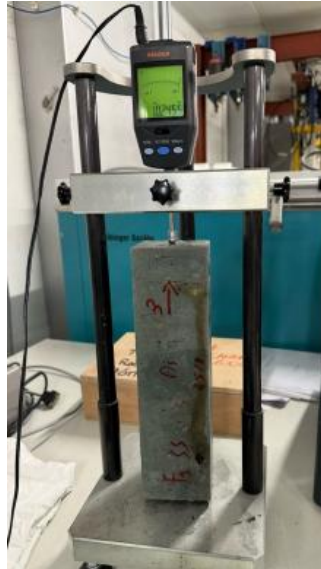


Figure 3.7: Dry shrinkage setup.

## Chapter 4

### 4. Results and Discussion

This chapter presents a detailed summary of the experimental results obtained in this study. It begins with an analysis of the mechanical performance, including compressive strength, flexural strength, and elastic modulus, for AAS mortars and concretes. This is followed by an evaluation of the dry shrinkage behaviour and corresponding mass loss. The results of this study will be compared with two reference OPC, CEM I and CEM III.

Subsequently, the outcomes of X-ray diffraction (XRD) analysis are discussed. The chapter concludes with two comparative analyses aimed at evaluating the influence of activator type, curing conditions, and admixture incorporation on mechanical properties and dry shrinkage behaviour.

#### 4.1. Compressive Strength of AAS mortars

This section presents the outcomes of the experimental investigations. The compressive strength results of AAS mortars are presented. Furthermore, the influence of different alkaline activators, curing regimes, and gypsum content on the mechanical properties is discussed in detail.

##### 4.1.1. Effect of alkaline activators

Figure 4.1 illustrates the compressive strength development of slag mortars activated with sodium silicate and sodium carbonate under the ambient curing compared to CEM I 42.5N and CEM III/B from the study of Zehrudin et al. [185]. Overall, sodium silicate-activated mixtures exhibited significantly higher compressive strengths compared to their sodium carbonate-activated counterparts. The compressive strength of sodium silicate-activated mortars increased steadily up to 180 days. In contrast, sodium carbonate-activated mortars demonstrated strength gains up to approximately 60 days, followed by a decline or plateau, suggesting potential strength degradation or stabilization over time. A continuous increase in the long-term strength was observed for NS, CEM I, and CEM III/B mortar.

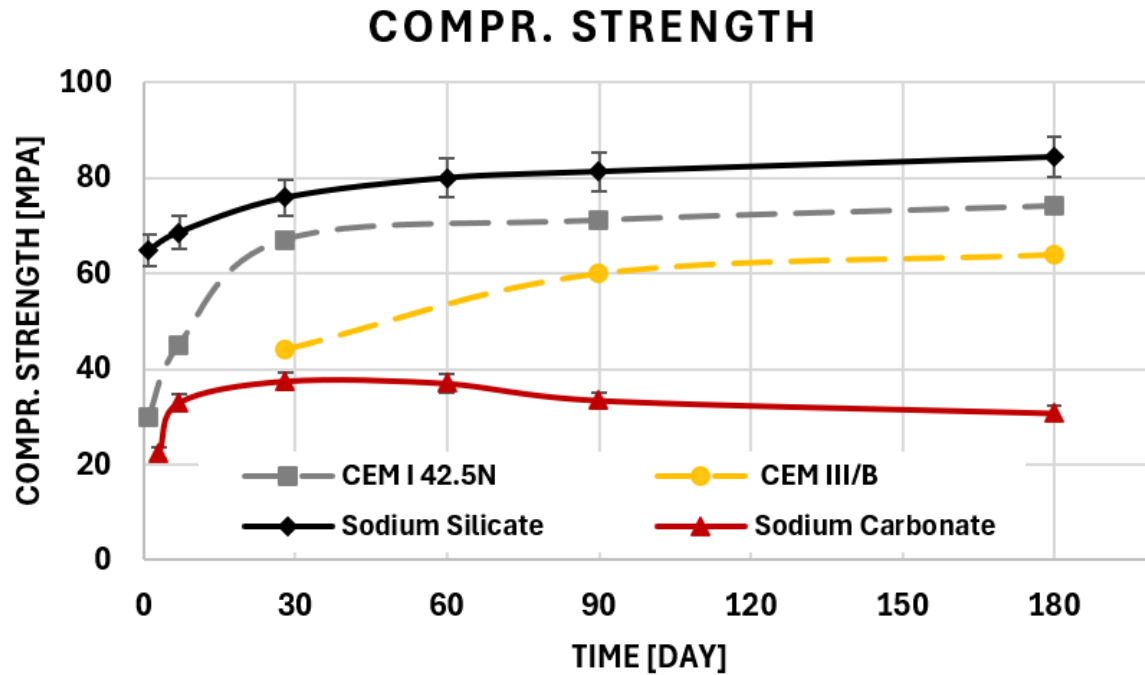


Figure 4.1: compressive strength of sodium silicate activated slag and sodium carbonate activated slag mortars compared to CEM I 42.5N and CEM III/B.

The higher compressive strength of sodium silicate-activated mortar is directly attributed to its lower porosity and greater degree of reaction [186]. Moreover, Jiménez et al. [25] attribute this behaviour to the lower pH environment created by sodium carbonate activators, which diminishes slag activation efficiency and consequently slows early-age strength development. The long-term reduction in compressive strength of sodium carbonate-activated mortars has also been reported by [94].

The  $\text{Na}_2\text{SO}_4$  (NS) mortar exhibited higher short-term compressive strength than the OP mortar, primarily due to its denser microstructure and reduced overall porosity resulting from the addition of  $\text{Na}_2\text{SO}_4$  [187]. Furthermore, the use of a one-part (solid) alkali activator (AA) in the AAS mortar contributed significantly to its early-age strength development. According to the findings of Minhao et al. [67], mortars activated with solid AAs achieved up to 20 MPa higher compressive strength than those activated with liquid AAs at comparable curing ages. This improvement was attributed to the controlled dissolution of the solid activator, which limited the availability of alkali ions in the fresh mixture and thereby reduced the likelihood of flash setting. Additionally, the structural incorporation of water within silicate crystals in the solid activator minimized pore formation during geopolymerization, resulting in a more compact matrix and enhanced mechanical performance compared to mortars prepared with liquid activators.

The compressive strength is strongly influenced by the material's porosity [188, 189]. Sodium silicate-activated mortars exhibit significantly lower total porosity, which directly enhances their load-bearing capacity compared to the more porous sodium carbonate-activated mortars. Therefore, higher compressive strength for sodium silicate-activated mortars.

#### 4.1.2. Effect of curing conditions

Figure 4.2 presents the compressive strength of sodium silicate-activated slag mortars cured (1) under ambient conditions and (2) subjected to 7 days of fog curing followed by ambient curing until testing. Samples subjected to the initial 7-day fog curing exhibited higher compressive strengths than those cured exclusively under ambient conditions. This improvement is attributed to the enhanced early-age hydration environment provided by elevated humidity, which promotes the formation of reaction products prior to exposure to drying conditions.

Collins et al. [29] further highlight the detrimental effects of curing conditions on AAS. Their mercury intrusion porosimeter (MIP) analyses revealed that exposed AAS samples developed significantly higher total porosity and a coarser pore size distribution compared to fog-cured specimens. Porosity was observed to increase progressively toward the specimen's exterior surface. Surface microcracking was prevalent in samples exposed to ambient curing, which corresponded with increased water sorptivity rates relative to fog-cured controls. This elevated sorptivity is attributed to an interconnected network of microcracks and capillary pores, which facilitates moisture ingress and contributes to reduced compressive strength. In addition, Monteiro and Kuhmar Mehta observed that compressive strength increases by approximately 15% when specimens are tested in a dry state compared to saturated conditions. This improvement is attributed to the densification of the paste matrix, likely resulting from enhanced van der Waals interactions between hydration products under dry conditions [190].

AAS are heterogeneous materials where the solid matrix carries the applied load. Fog curing reduces total porosity, thereby a greater fraction of the cross-sectional area is composed of solid phases (C-(A)-S-H gel, reaction products, and aggregates) that can resist stresses. This enhances the load-bearing capacity per unit volume. At the same time, pores act as stress concentrators under compression; a lower porosity reduces the number of such weak points, limiting microcrack initiation and propagation. As a result, increase the compressive strength. These findings highlight the importance of curing regime and moisture state in strength development. Careful control of early-age curing leads to higher compressive strength.

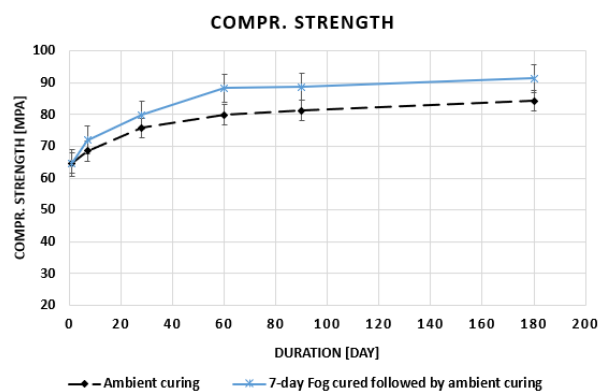


Figure 4.2: Compressive Strength of sodium silicate-activated slag mortars under 1) ambient curing, and 2) 7-day fog curing followed by ambient curing.

### 4.1.3. Effect of Admixtures

Figure 4.3 presents the compressive strength of sodium silicate-activated slag mortars with and without gypsum under ambient curing conditions and under (a) 7 days of fog curing followed by ambient curing until testing and (b) continuous ambient curing.

The addition of gypsum to the AAS system reduced early-age compressive strength. This retardation is attributed to a slower dissolution rate of slag particles: gypsum dissolves rapidly in the alkaline environment, promoting the early precipitation of portlandite and thenardite. This lowers the pH of the pore solution, which in turn slows slag dissolution and delays the formation of calcium–alumino–silicate–hydrate (C–A–S–H) gel [191, 25].

However, mortars containing gypsum exhibited a faster strength gain over time compared to gypsum-free mixtures. This is due to gypsum participating in secondary hydration reactions, forming expansive crystalline phases such as ettringite (AFt) and monosulfate (AFm) (Figure 4.3). These phases contribute to microstructural densification by filling pores, ultimately enhancing long-term compressive strength despite the initial delay.

Overall, while gypsum initially retards early-age strength development by slowing slag dissolution, it promotes long-term strength gain through secondary hydration and microstructural densification, highlighting its dual role in AAS mortars.

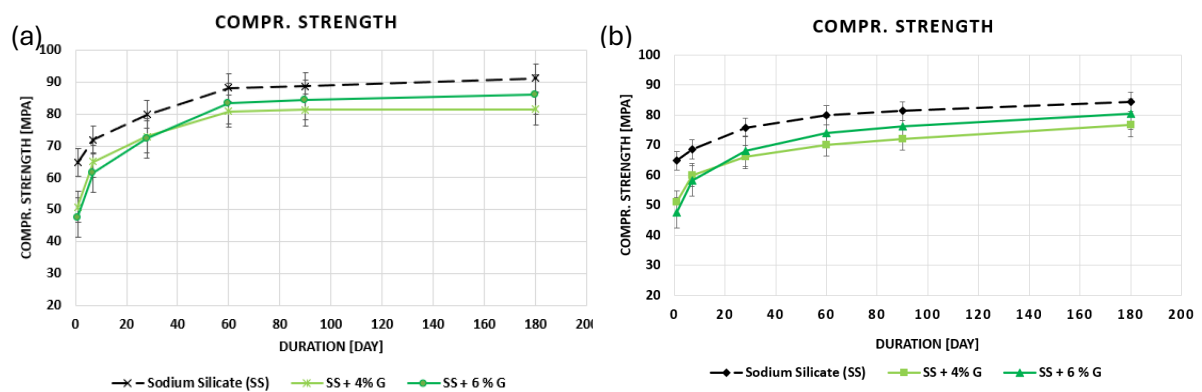


Figure 4.3: Compressive strength of sodium silicate activated slag mortar with and without gypsum, a) 7-day fog cured followed by ambient curing, and b) ambient curing.

## 4.2. Flexural strength of AAS mortars

This section presents the outcomes of the experimental investigations. The flexural strength results of alkali-activated mortars are presented. Furthermore, the influence of different alkaline activators, curing regimes, and gypsum content on the mechanical properties is discussed in detail.

### 4.2.1. Effect of alkaline activators

Figure 4.5 presents the flexural strength of slag mortars activated with sodium silicate and sodium carbonate under ambient curing compared to CEM I 42.5N and CEM III/B from the study of Zehrudin et al. [185]. It is evident that the flexural strength of sodium silicate-activated mortars is consistently higher than that of sodium carbonate-activated mortars. This improvement is attributed to the soluble Si present in sodium silicate activators, which enhances the formation of reaction products and promotes microstructural densification [192]. Moreover, sodium silicate mortars exhibit lower porosity and a more refined pore structure compared to sodium carbonate-activated mortars [186].

Porosity plays a critical role in flexural strength. Higher porosity introduces voids and weak points that act as stress concentrators, particularly under tensile stress at the outer surface during bending. These defects facilitate microcrack initiation and propagation, ultimately reducing the material's ability to sustain tensile loads and leading to premature fracture. Conversely, reducing total porosity and refining the pore structure creates a denser, more homogeneous matrix, which improves stress distribution and delays crack initiation. As a result, mortars with lower porosity generally achieve higher flexural strength.

Furthermore, sodium carbonate-activated mortars generally demonstrated lower flexural strength. This reduction is partly due to their higher dry shrinkage, which contributes to the development of microcracks. Moreover, visible surface cracks were observed in the NC mortar, whereas no surface cracking was detected in the NS mortar, as illustrated in Figure 4.4. These shrinkage-induced microcracks compromise the integrity of the matrix and reduce its ability to resist tensile stresses, thereby lowering flexural strength. Although some studies suggest that shrinkage might reduce both the number and width of microcracks under specific conditions [83], the overall effect in sodium carbonate systems appears to be detrimental to mechanical performance due to the combined influence of lower reaction rates and higher dimensional instability. The long-term reduction in flexural strength of sodium carbonate-activated mortars has also been reported by [94].

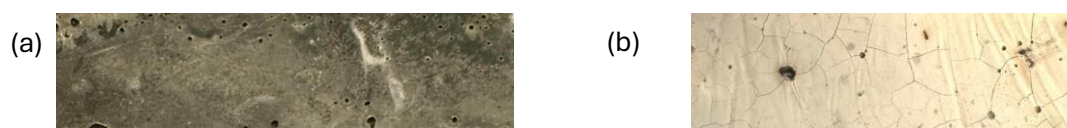


Figure 4.4: (a) No cracks visible in the sodium silicate (NS) specimens, (b) cracks visible in casted surface of sodium carbonate (NC) specimens.

The flexural strength of CEM I 42.5N and CEM III/B mortars typically increases over time, whereas in AAS systems it often stagnates or decreases at later ages. This contrast arises from differences in the hydration mechanisms, gel chemistry, and microstructural evolution of these binders. In Portland cement systems, ongoing hydration of unreacted  $C_3S$  and  $C_2S$  phases progressively produces additional calcium-silicate-hydrate (C-S-H) gel, while latent hydraulic components such as slag in CEM III/B continue to react slowly, refining the pore structure and enhancing the interfacial transition zone (ITZ) between paste and aggregate.



This continuous microstructural densification leads to a steady increase in both compressive and flexural strength over time [193, 194].

In contrast, AAS binders form a C–(A)–S–H-type gel with a lower Ca/Si ratio and higher Al incorporation, which results in a more rigid but brittle microstructure with limited long-term adaptability [195]. During early curing, AAS systems hydrate rapidly, leading to high initial strength [196]; however, at later ages, continued autogenous and dry shrinkage, microcrack formation, and limited late-age reaction potential cause a reduction in flexural strength, as can be seen in section 4.5.1.

Overall, the higher porosity of sodium carbonate-activated mortar results in lower flexural strength, whereas the lower porosity of sodium silicate-activated mortar contributes to higher flexural strength. The flexural strength of the NS mortar decreased over time, in contrast to the continuous strength gain observed in the CEM I 42.5N and CEM III/B mortars. This decline in the AAS system is primarily attributed to its higher susceptibility to dry shrinkage and the consequent formation of microcracks, which compromise the material's tensile capacity and structural integrity.

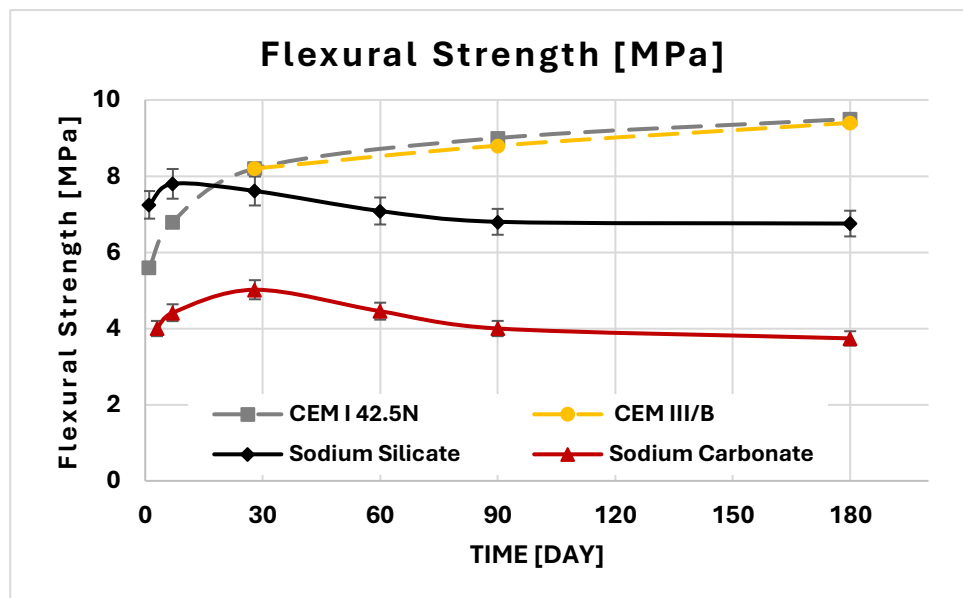


Figure 4.5: Flexural strength of both sodium silicate and sodium carbonate activated slag mortars compared to CEM I 42.5N and CEM III/B.

#### 4.2.2. Effect of curing conditions

Flexural strength increased for both curing conditions up to 7 days. Notably, mortars cured under fog conditions achieved approximately 1.5 MPa higher flexural strength at day 7 compared to those subjected to ambient curing. However, after this early-age gain, a slight decline in flexural strength was observed, resulting in similar 180-day values for both curing regimes in sodium silicate-activated mortars, as illustrated in Figure 4.6.

The superior early flexural performance of fog-cured samples can be attributed to the high relative humidity (RH), which supports more favourable hydration conditions and limits the formation of shrinkage-induced microcracks. Elevated RH has been shown to reduce both the number and width of such microcracks [83]. Moreover, slower drying rates—such as those achieved through fog curing—promote more uniform internal moisture gradients, which mitigate the development of internal tensile stresses that typically lead to microcracking and shrinkage. Previous research has confirmed that reduced drying rates are associated with decreased microcracking and shrinkage in AAS mortars [197, 198].

Moreover, the dry shrinkage of ambient-cured samples was significantly higher compared to fog-cured samples, as will be discussed in Section 4.5.2. Shrinkage plays a decisive role in the risk of cracking, particularly under restrained conditions. When volumetric changes due to moisture loss are constrained tensile stresses can develop within the matrix. If these stresses exceed the tensile strength of the material, cracking is likely to occur. Such cracks may act as pathways for the ingress of aggressive agents, including carbon dioxide and chloride ions, which can progressively undermine the structural integrity and long-term durability of the system [199].

Overall, the flexural strength of AAS materials is highly sensitive to microcracks and surface defects. Ambient curing exacerbates this vulnerability by promoting dry shrinkage, which induces crack formation. Under tensile stress, these cracks propagate, ultimately leading to premature sample failure.

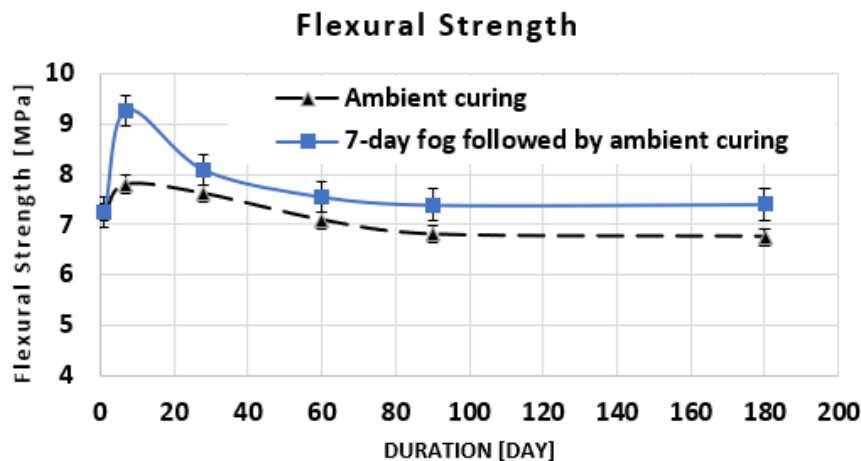


Figure 4.6: Flexural Strength of sodium silicate-activated slag mortars under 1) ambient curing, and 2) 7-day fog curing followed by ambient curing.

### 4.2.3. Effect of admixtures

Gypsum was selected as an admixture based on the findings presented in Section 4.5.3, where it demonstrated the most significant effect in reducing dry shrinkage. As shown in Figure 4.7, the incorporation of 6% gypsum into sodium silicate-activated slag mortars resulted in a reduction in 1-day flexural strength, likely due to its influence on early hydration kinetics and the delay in initial gel formation. However, by day 7, the flexural strength of gypsum-modified mortars had reached levels comparable to those of the control samples without gypsum and subsequently exceeded them slightly at 30, 60, 90, 120, and 180 days. This trend indicates a beneficial long-term contribution of gypsum to the flexural performance of the material.

The observed differences in flexural strength can be attributed to the interplay between the alkali activator type, curing regime, and the presence of gypsum, all of which affect the microstructural evolution of AAS mortars. In particular, gypsum promotes the formation of secondary hydration products, such as ettringite and monosulfate phases, which contribute to matrix densification and improved mechanical integrity over time. Additionally, flexural strength is strongly influenced by dry shrinkage behaviour, with reduced shrinkage typically correlating with enhanced tensile and flexural performance due to fewer and narrower microcracks within the binder matrix.

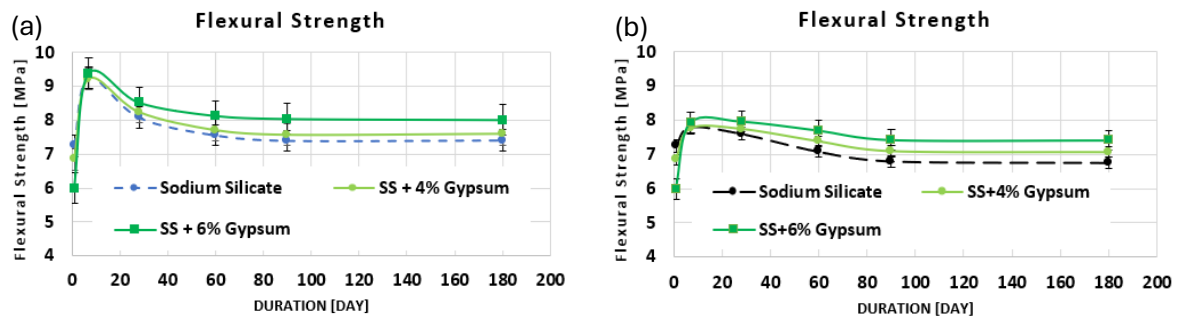


Figure 4.7: Flexural strength of sodium silicate activated slag mortar with and without gypsum, a) 7-day fog cured followed by ambient curing, and b) ambient curing.

### 4.3. E-modulus of AAS mortars

#### 4.3.1. Effect of alkaline activators

Figure 4.8 presents the elastic modulus of mortars activated with sodium silicate and sodium carbonate under ambient curing compared to CEM I 42.5N and CEM III/B from the study of the European Technical Assessment [200]. Overall, mortars activated with sodium silicate exhibited significantly higher elastic modulus values compared to those activated with sodium carbonate, due to the larger amount of reaction products and the denser pore structure formed as shown in section 4.2.1. The elastic modulus of CEM I 42.5N and CEM III/B concretes increases over time due to the continued hydration of clinker and slag phases, which progressively densifies the microstructure, fills capillary pores, and strengthens the interfacial transition zone. In contrast, AAS mortars show a reduction in modulus over time because of higher autogenous and dry shrinkage, microcrack formation, and limited late-age gel development. The C–(A)–S–H gel in AAS is brittle, and the absence of portlandite reduces buffering against carbonation and shrinkage-induced stresses, leading to stiffness loss at later ages as shown in section 4.2.1.

Mortars activated with sodium silicate exhibited lower total porosity and a finer pore structure, leading to reduced moisture loss compared to those activated with sodium carbonate [27]. Furthermore, these differences in stiffness can be primarily attributed to the greater dry shrinkage observed in sodium carbonate-activated mortars, which compromises microstructural integrity and leads to reduced stiffness [201]. Additionally, the disparity arises from the nature and extent of hydration products formed. Sodium silicate activation promotes the development of dense, well-polymerized calcium–aluminosilicate–hydrate (C–A–S–H) gel networks that enhance mechanical strength and elastic behaviour. In contrast, sodium carbonate-activated systems tend to form more porous and less cohesive matrices, with reaction products such as gaylussite and other carbonate-containing phases that contribute minimally to stiffness and overall mechanical performance.

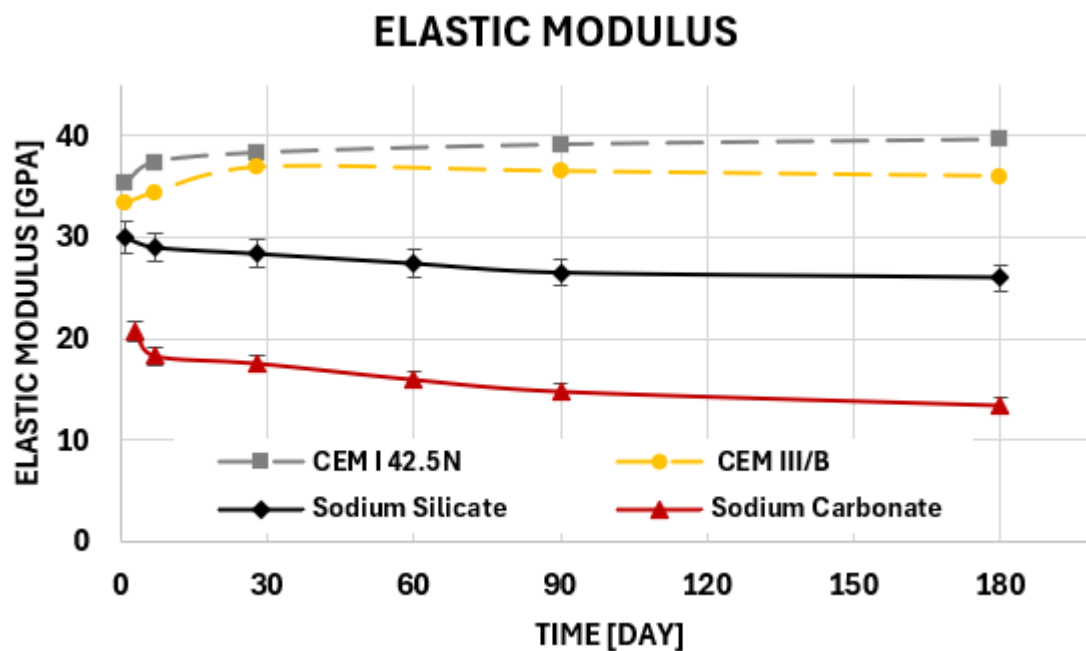


Figure 4.8: Elastic modulus of both sodium silicate and sodium carbonate activated slag mortars compared to CEM I 42.5N and CEM III/B.

### 4.3.2. Effect of curing conditions

A notable increase in elastic modulus was observed during the initial 7-day fog curing period. Specifically, fog-cured specimens exhibited an approximately 5.0 MPa higher elastic modulus at day 7 compared to those subjected continuous to ambient curing conditions. However, beyond this period, a gradual decline in stiffness was recorded. Sodium silicate-activated mortars showed a decrease in elastic modulus from 34 MPa at day 7 to 29 MPa at 180 days. In contrast, mortars continuously cured under ambient conditions demonstrated a steady reduction in stiffness beginning from day 1, consistently yielding lower values than their fog-cured counterparts, as illustrated in Figure 4.9.

Unlike compressive strength, which primarily depends on the porosity of the solid skeleton, the elastic modulus is also affected by the development of microcracking [202, 203, 204]. Under both curing conditions, a continuous decrease in elastic modulus was observed: for ambient-cured samples, this decline started after just one day, whereas for samples fog-cured for seven days and then exposed to ambient conditions, the decrease began after seven days. This reduction can be attributed to extensive cracking caused by dry shrinkage, as discussed in Section 4.2.2. Furthermore, as shown in Section 4.1.2, fog curing helps reduce porosity, which is another key factor influencing the elastic modulus.

Furthermore, the initial increase in elastic modulus during fog curing is likely attributed to reduced moisture loss and the provision of adequate humidity, which together foster more complete hydration and the uniform development of reaction products. This favourable curing environment minimizes early-age drying stresses and promotes the formation of a denser, more cohesive microstructure. The subsequent decline in elastic modulus after day 7—particularly pronounced in ambient-cured specimens—may be attributed to progressive microcracking induced by dry shrinkage and the continued lack of internal moisture, which deteriorates the microstructural integrity and diminishes overall stiffness over time.

Monteiro and Mehta [190] reported that concrete specimens tested in a saturated state exhibit an elastic modulus approximately 15% higher than that of similar specimens tested under dry conditions, irrespective of mix composition or curing duration. In a related study, the authors attributed this reduction in stiffness to microcracking within the interfacial transition zone (ITZ), which becomes more pronounced under drying conditions. A similar mechanism may be relevant to alkali-activated concrete. However, the reduction in elastic modulus observed in the present study exceeds the 15% decrease reported by Monteiro and Mehta, indicating that additional factors may be contributing to the decline in stiffness [190].

Overall, fog curing mitigates the two primary factors that govern the elastic modulus, namely microcracking and porosity. As discussed in Section 4.2.2, the reduction of dry shrinkage limits the formation of microcracks, while Section 4.1.2 demonstrated that fog curing decreases porosity. Together, these effects contribute to an overall increase in the elastic modulus during the fog curing period.

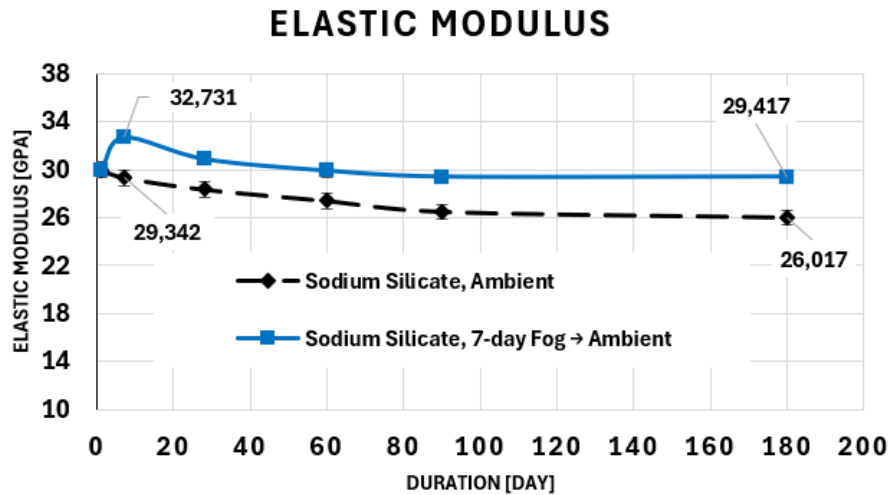
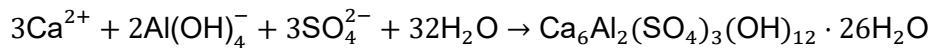


Figure 4.9: Elastic modulus of sodium silicate-activated slag mortars under 1) ambient curing, and 2) 7-day fog curing followed by ambient curing.

#### 4.3.3. Effect of admixtures

Figure 4.10 presents the elastic modulus of mortars activated with sodium silicate with and without gypsum under the two curing conditions described previously. The inclusion of 6% gypsum had minimal effect on the elastic modulus under both curing regimes. This indicates that gypsum exerts a negligible influence on the stiffness characteristics of AAS mortars.

Under alkaline conditions typical of AAS systems, the sulphate from gypsum reacts with calcium and aluminate species to form ettringite:



The formation of ettringite, whose significantly larger molar volume compared with its reactants leads to swelling pressure as the needle-like crystals precipitate and grow within the pore network; this growth fills available pores and can push against the surrounding matrix, causing measurable expansion in unrestrained conditions. Therefore, the shrinkage is reduced due to this expansion; however, the resulting expansion does not contribute to an increase in the elastic modulus.

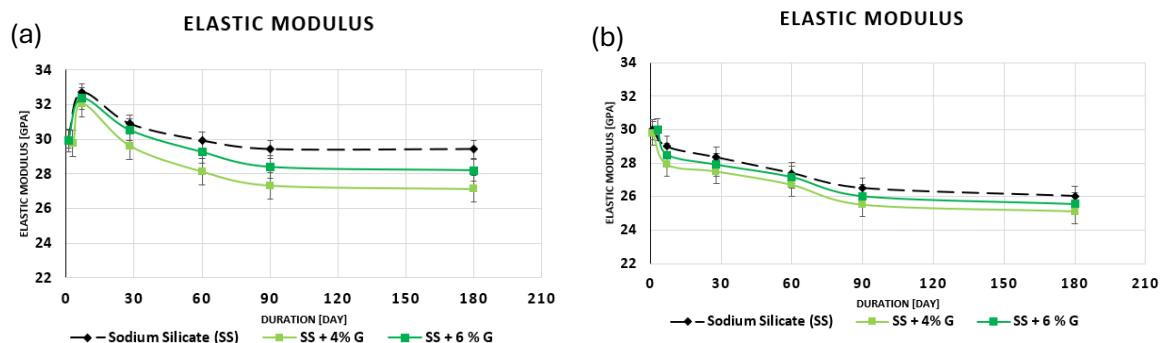


Figure 4.10: Elastic modulus of sodium silicate activated slag mortar with and without gypsum, a) 7-day fog cured followed by ambient curing, and b) ambient curing

#### 4.3.4. Comparison E-modulus with Predicted Model Codes

The experimentally measured age-dependent elastic modulus of NS mortars was compared with predictions from several widely used models, including ACI 209 [205], CEB FIP [206], B3 [207], and GL-2000 [208], as illustrated in Figure 4.11. A summary of the models recommended by these codes and researchers for elastic modulus prediction is provided in Table 4.1. This comparison allows evaluation of the accuracy of standard predictive models against the actual mechanical behaviour of alkali-activated mortars over time.

Table 4.1: Models for age-dependent static modulus of elasticity.

ACI 209 [205]	$(E_c)_t = 0.043 \sqrt{\frac{\rho^3 (f'_c)_{28} t}{4 + 0.85 t}}$
CEB-FIP [206]	$E_c = 21500 \left(\frac{(f'_c)_{28}}{10}\right)^{1/3} \sqrt{\exp\left(\frac{1}{4} - \sqrt{\frac{7}{4t}}\right)}$
B3 [207]	$(E_c)_t = 4734 \sqrt{\frac{(f'_c)_{28} t}{4 + 0.85 t}}$
GL-2000 [208]	$(E_c)_t = 3500 + 4300 \sqrt{\frac{(f'_c)_{28} t^{0.75}}{2.8 + 0.77 t^{0.75}}}$

In standard codes, the elastic modulus of OP increases rapidly during the first 28 days due to ongoing hydration and microstructural densification, with only slight increases thereafter. In contrast, AAS shows a high early-age modulus but declines continuously after 1 day, reaching approximately half the code-predicted value after 180 days. This reduction is caused by high autogenous and dry shrinkage, microcrack formation, and the brittle nature of the C-(A)-S-H gel as will be discussed in section 4.5.1.

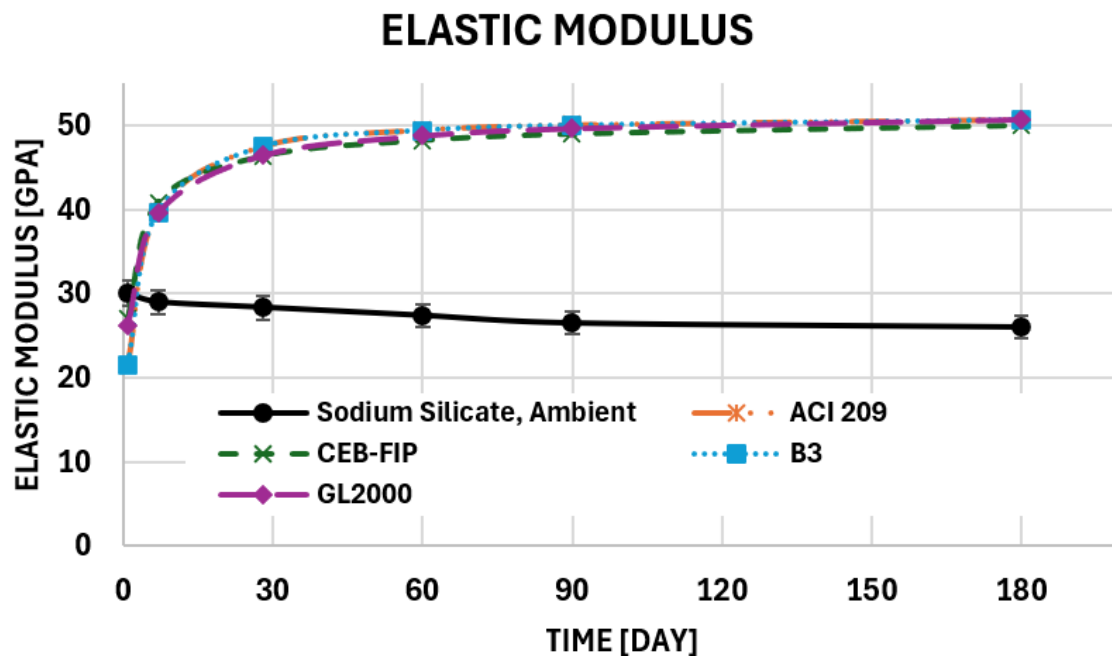


Figure 4.11: Comparison of the elastic modulus of NS mortar with predictions from various model codes.



## 4.4. Mechanical properties of alkali-activated slag concrete

### 4.4.1. Compressive strength

As shown in Figures 4.12, compared to Figure 4.3, concrete specimens exhibited higher short- and long-term compressive strengths than their mortar counterparts. This disparity is primarily attributed to the presence of coarse aggregates in concrete and their interaction with the binder matrix. The inclusion of coarse aggregates in concrete results in a denser internal structure, which effectively reduces overall porosity and enhances the material's load-bearing capacity. In contrast, mortar, lacking coarse aggregates, maintains a more homogeneous but comparatively weaker matrix, leading to lower compressive strength. This difference between the AAS mortars and concrete is consistent with the findings reported in [27, 101].

The compressive strength of the AAC was compared with that of CEM I 42.5 R-NA and CEM III/A 42.5 HSR-NA, as reported by Tomasz [185]. The compressive strength of all mixtures increased progressively over time. Notably, the AAC exhibited both higher early-age and long-term compressive strength compared to the OPC references. This enhancement is attributed to its denser microstructure and reduced overall porosity, resulting from the incorporation of  $\text{Na}_2\text{SO}_4$ , as discussed in Section 4.1.1.

The beneficial effect of 7-day fog curing was evident in both mortar and concrete samples. This curing regime facilitates early-age hydration, decreases porosity, and mitigates initial dry shrinkage, thereby promoting improved compressive strength development across both material types.

The incorporation of gypsum into AAS systems has been shown to reduce early-age compressive strength. This reduction is associated with a retardation of slag dissolution, as gypsum dissolves rapidly in the alkaline environment, promoting the early precipitation of portlandite and thenardite. The consequent reduction in pore solution pH slows down slag dissolution and delays the formation of calcium–alumino–silicate–hydrate (C–A–S–H) gel [191, 25]. Beyond the early ages, gypsum-containing samples generally develop strength at a rate comparable to mixes without gypsum. Nevertheless, the initial retardation indicates that gypsum addition has an overall adverse effect on the compressive strength development of AAS concrete.

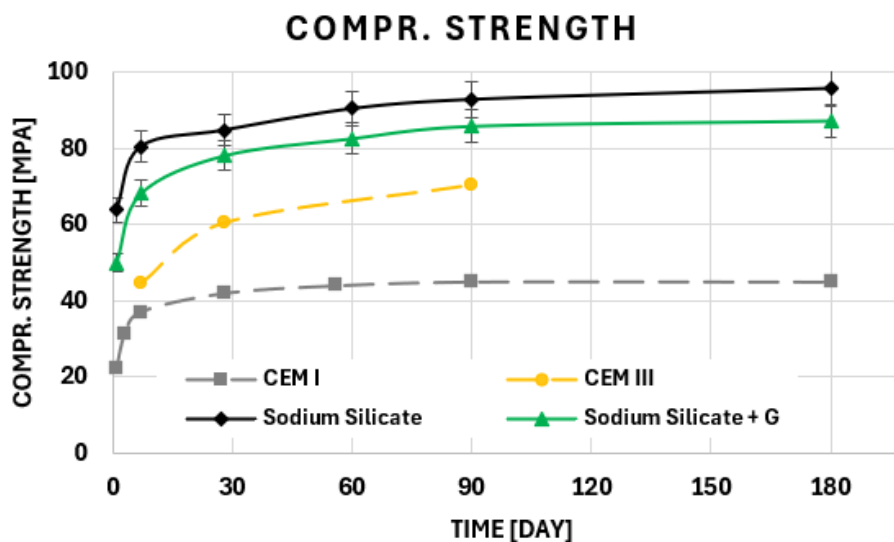


Figure 4.12: Compressive strength of sodium silicate activated concrete compared to CEM I 42.5 R-NA and CEM III/A 42.5 HSR-NA.

#### 4.4.2. Flexural strength

In contrast to compressive behaviour, flexural strength was generally lower in concrete than in AAS mortar, as illustrated in Figures 4.13 compared to Figure 4.7. This unexpected trend is largely explained by the structural differences between the two materials. Mortar, being free of coarse aggregate interfaces, offers a more uniform matrix that allows better stress distribution and crack resistance under bending. As a result, it performs more effectively in flexural loading scenarios. This difference between the AAS mortars and concrete is consistent with the findings reported in [27, 101].

In concrete, the rigid nature of coarse aggregates, while beneficial for compressive strength, restricts the binder matrix's ability to deform and bridge cracks. This leads to a reduced strain capacity and compromises flexural strength. Thus, although concrete is structurally stronger in compression, mortar can outperform it in bending due to its more homogeneous and continuous matrix.

The flexural strength of the AAC was compared with CEM I 42.5 R-NA and CEM III/A 42.5 HSR-NA, as reported by Tomasz [185]. The flexural strength of CEM I 42.5 R-NA and CEM III/A increased progressively over time. However, the flexural strength of AAC decreases over time when it was exposed to the ambient curing conditions, primarily due to continued autogenous and dry shrinkage and the resulting microcrack formation, as discussed in Section 4.2.1.

The reduction in flexural strength observed after 7 days of fog curing (when the samples are exposed to the ambient curing) may be attributed to the initiation of microcracks within the concrete matrix, primarily caused by restrained autogenous shrinkage [202]. Even though the specimens used for strength testing were not externally restrained, the aggregates themselves can act as internal restraints, limiting the shrinkage of the surrounding paste and thereby inducing localized stresses [202]. In addition, ongoing dry shrinkage (as will be discussed in Section 4.5.4) could have further contributed to microcrack formation, despite the absence of visible surface cracking. The development of microcracking can harm the (increase of) flexural strength.

Although gypsum addition may slightly delay the early-age development of flexural strength due to slower slag dissolution and the precipitation of initial reaction products, it subsequently mitigates shrinkage, reduces microcracking, and increases flexural strength.

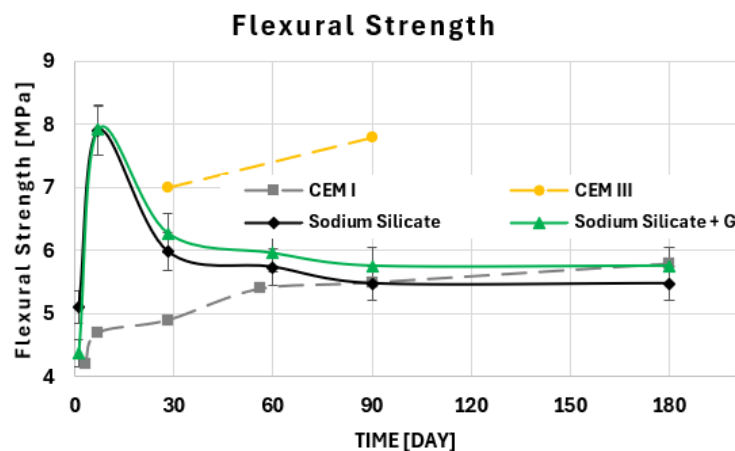


Figure 4.13: Flexural strength of sodium silicate activated concrete compared to CEM I 42.5 R-NA and CEM III/A 42.5 HSR-NA.

#### 4.4.3. Elastic modulus

Concrete also demonstrated a higher elastic modulus than mortar, as evidenced by Figures 4.14 and 4.10. This behaviour is attributed to the stiffness imparted by the coarse aggregates embedded in the concrete matrix. These aggregates act as rigid inclusions, restraining matrix deformation and increasing resistance to external loading. The result is a stiffer overall material response, with concrete exhibiting greater elastic modulus values than mortar.

The elastic modulus of the AAC was compared with CEM I/HSC [176] and CEM III/B 42.5 N [209]. The elastic modulus of CEM I/HSC and CEM III/B 42.5 N increased progressively over time. However, the flexural strength of AAC decreases over time when it was exposed to the ambient curing conditions and stabilizes after approximately three months, primarily due to continued autogenous and dry shrinkage and the resulting microcrack formation, as discussed in Section 4.3.1.

The impact of fog curing was again beneficial, enhancing early hydration and matrix densification in both materials. Additionally, the presence of gypsum has only a minor effect on the stiffness behaviour of AAS mortars. While its incorporation can influence shrinkage and early-age expansion through the formation of ettringite (AFt) and monosulfate (AFm), these phases appear to interact only marginally and for a limited duration with the main load-bearing C–A–S–H network. As a result, their contribution to the development of elastic stiffness is negligible, leading to little or no improvement in the overall modulus.

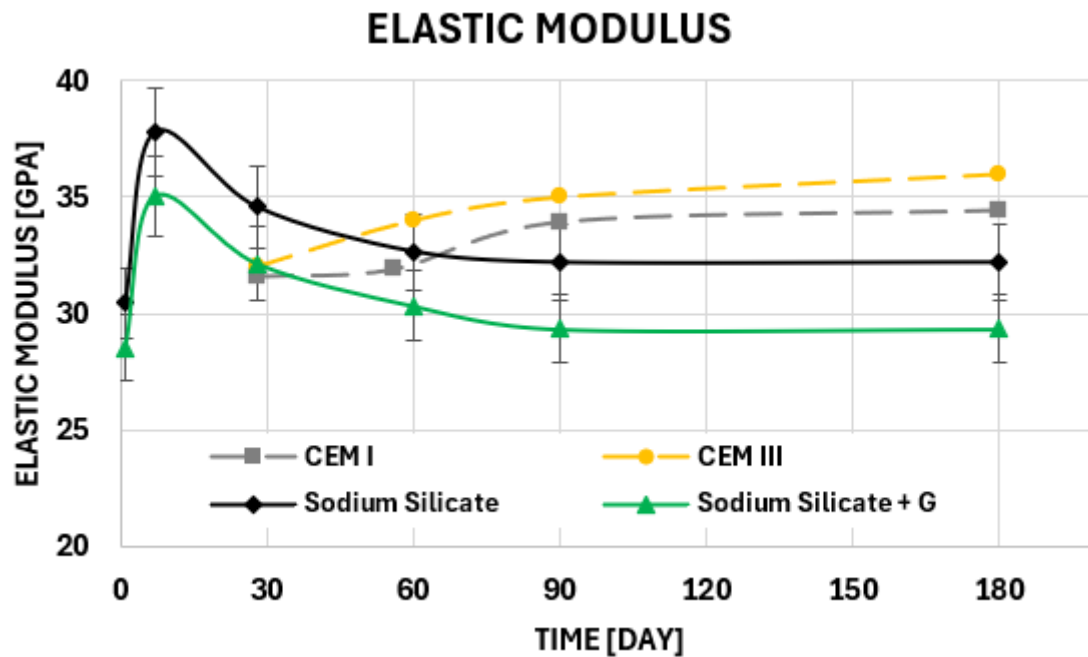


Figure 4.14: Elastic modulus of sodium silicate activated concrete compared to CEM I/HSC and CEM III/B 42.5 N.

#### 4.4.4. Correlation between compressive strength and flexural strength & modulus of elasticity

##### Correlation between compressive strength and modulus of elasticity for AAS and CEM I 42.5N mortars

Figure 4.15 (a) show the correlation between compressive strength and modulus of elasticity for AAS, CEM I 42.5N, and CEM III/B mortars and (b) show the effects of initial 7-day curing. The relationship between elastic modulus (E-modulus) and compressive strength differs among CEM I and NS mortars due to differences in hydration mechanisms, microstructure evolution, and shrinkage behaviour.

In CEM I mortar, the elastic modulus increases alongside compressive strength because ongoing hydration of clinker phases (mainly  $C_3S$  and  $C_2S$ ) produces additional C–S–H gel, which densifies the microstructure (section 4.3.1). In the case of NS mortar, the E-modulus decreases over time despite increasing compressive strength under ambient curing. This is due to the combined effect of autogenous and dry shrinkage, microcracking, and the brittle nature of the C–(A)–S–H gel, which reduces the material's ability to resist elastic deformation. However, when fog curing is applied for the first 7 days, the E-modulus initially increases because the high humidity reduces early-age drying, mitigates shrinkage, and promotes more complete early gel formation, resulting in a temporarily denser and stiffer microstructure (section 4.3.1 and 4.3.2).

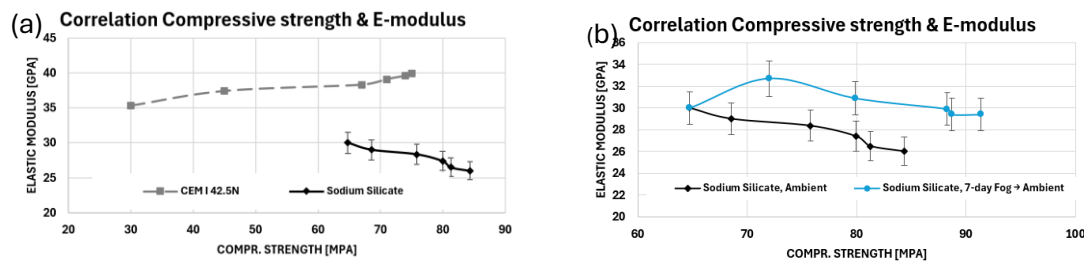


Figure 4.15: (a) Correlation between compressive strength and elastic modulus for AAS and CEM I 42.5N mortars; (b) effect of the initial 7-day curing on the elastic modulus.

##### Correlation between compressive strength and modulus of elasticity for AAS and CEM I 42.5N mortars

Similar to the previous section, Figure 4.16 presents the correlation between compressive and flexural strength for AAS and CEM I 42.5N mortars. The results indicate increases in compressive strength correspond to higher flexural strength for CEM I 42.5N. However reduction in flexural strength for AAS mortar. These trends and the associated discussion are consistent with those presented in the preceding section, highlighting the influence of microstructural development and binder type on mechanical performance.

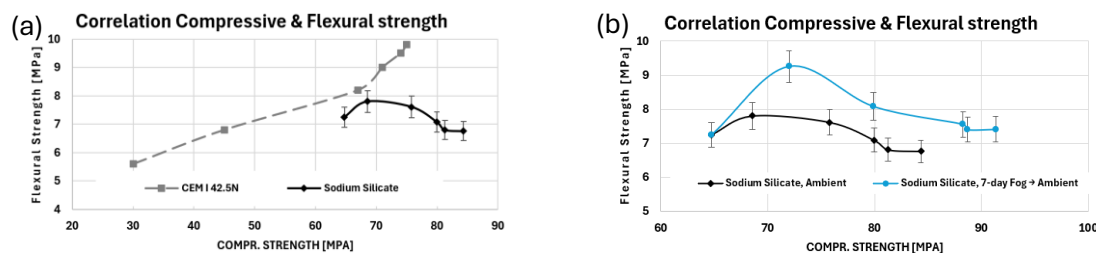


Figure 4.16: (a) Correlation between compressive strength and flexural strength for AAS and CEM I 42.5N mortars; (b) effect of the initial 7-day curing on the elastic modulus.

## 4.5. Dry shrinkage and weight loss of AAS mortars

This section presents the findings on dry shrinkage, focusing on the effects of alkaline activators, curing conditions and admixture incorporation. The influence of these variables on shrinkage behaviour and moisture loss is first examined. Based on the outcomes, the most effective curing conditions and admixture combinations are identified for further analysis. The results of this study will be compared with two reference OPCCs, CEM I and CEM III.

### 4.5.1. Effect of the alkaline activators

Based on the results presented in the previous section, a curing regime consisting of 7 days of fog curing followed by either ambient or sealed curing was selected for further investigation. This regime was identified as the most effective in reducing long-term dry shrinkage.

This section examines the dry shrinkage and mass loss behaviour of alkali-activated slag (AAS) mortar samples prepared using two types of alkaline activators: sodium silicate and sodium carbonate. The samples were subjected to the following curing conditions:

- Fog curing for 7 days followed by ambient exposure
- Fog curing for 7 days followed by sealed curing<sup>1</sup>

<sup>1</sup>The samples were fully covered with plastic film and secured with adhesive tape to ensure an airtight seal. The weight of each sample was recorded both before and after sealing. The reduction in weight loss due to sealing was determined by comparing the measured weight change after sealing.

Figure 4.17 illustrate the evolution of dry shrinkage and mass loss, respectively, over a period of 180 days for both activator systems. As shown in Figure 4.13 (a), negligible shrinkage occurred during the initial 7-day fog curing period due to the high humidity environment, which effectively prevented moisture evaporation. However, upon exposure to ambient conditions, all specimens exhibited a gradual increase in shrinkage over time.

Simultaneously, as depicted in Figure 4.17 (b), the sodium carbonate-activated samples experienced significantly greater mass loss—approximately 5.1% by day 180—compared to their sodium silicate-activated 1.05 % counterparts. Correspondingly, sodium carbonate samples exhibited substantially higher shrinkage values, reaching approximately 2900  $\mu\text{m/m}$ , nearly twice the shrinkage measured in sodium silicate samples, which remained around 1500  $\mu\text{m/m}$ . The high dry shrinkage observed with sodium carbonate samples is consistent with previous research [57, 63, 188].

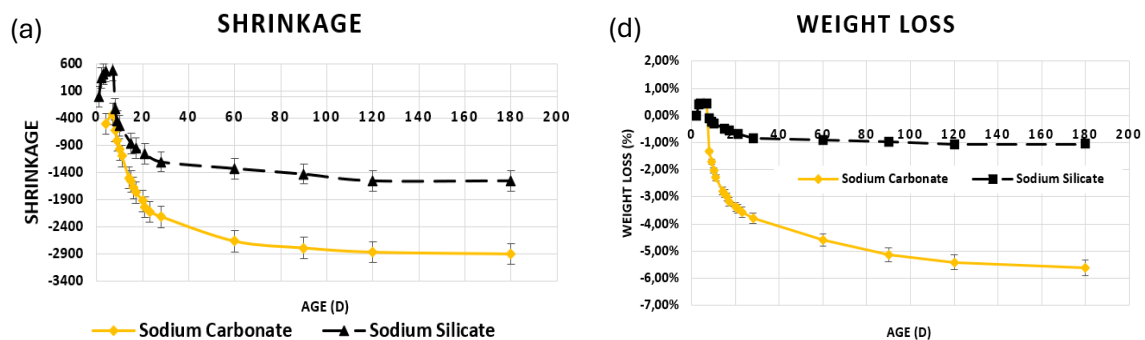


Figure 4.17: (a) Dry shrinkage and (b) weight loss of samples activated with sodium silicate and sodium carbonate under 7-day fog curing followed by ambient curing.

The reduced dry shrinkage observed in sodium silicate-activated samples is primarily attributed to the formation of a denser and more cohesive reaction gel in sodium silicate-based systems, which limits moisture transport and suppresses the development of capillary stresses. In contrast, sodium carbonate-activated mixtures demonstrated higher porosity and cumulative moisture loss, resulting in nearly double the long-term shrinkage relative to the sodium silicate samples.

The increased dry shrinkage observed in sodium carbonate-activated systems can be attributed to their inherently more porous microstructure and slower reaction kinetics, which delay the formation of stable binding phases. This prolonged reaction period extends the duration over which shrinkage occurs. Additionally, XRD analysis (section 4.6) confirmed the presence of gaylussite, a thermodynamically unstable phase under dry conditions, which gradually decomposes over time. This decomposition releases bound water, increases porosity, and accelerates moisture loss, thereby intensifying shrinkage. The instability and breakdown of gaylussite, as reported by Yuan et al. [189], contribute not only to greater dimensional instability but also to reduced mechanical performance through elevated shrinkage levels.

Moreover, in the early stages of sodium carbonate activation, calcium ions ( $\text{Ca}^{2+}$ ) preferentially react with carbonate ions ( $\text{CO}_3^{2-}$ ) to form calcium carbonate and gaylussite. While the aluminosilicate component of the slag—particularly the Al–Si–O network that gradually dissolves under the mildly alkaline conditions—reacts independently with sodium ions ( $\text{Na}^+$ ) from the activator. This reaction promotes the nucleation and growth of zeolitic phases, such as zeolite NaA [57]. However, these early-age reaction products offer limited contribution to mechanical strength development due to the relatively slow reaction kinetics imposed by the moderate pH environment of sodium carbonate solutions [189, 188]. The results from an additional set of specimens sealed after the initial fog curing period are presented in Figures 4.18.

As expected, the sealed samples exhibited no further weight loss following curing (Figure 4.18 b), due to the absence of external moisture evaporation. Nevertheless, a measurable degree of shrinkage was still observed (Figure 4.18 a). Although the shrinkage was lower than that observed in the unsealed samples, its persistence indicates that internal mechanisms—namely chemical shrinkage and self-desiccation—continue to contribute to volumetric changes, even in the absence of external drying. These phenomena result from ongoing hydration reactions and progressive microstructural densification, which are particularly characteristic of alkali-activated slag systems. Therefore, dry shrinkage in such binders is governed not only by environmental humidity but also by intrinsic chemical and physical processes within the material matrix.

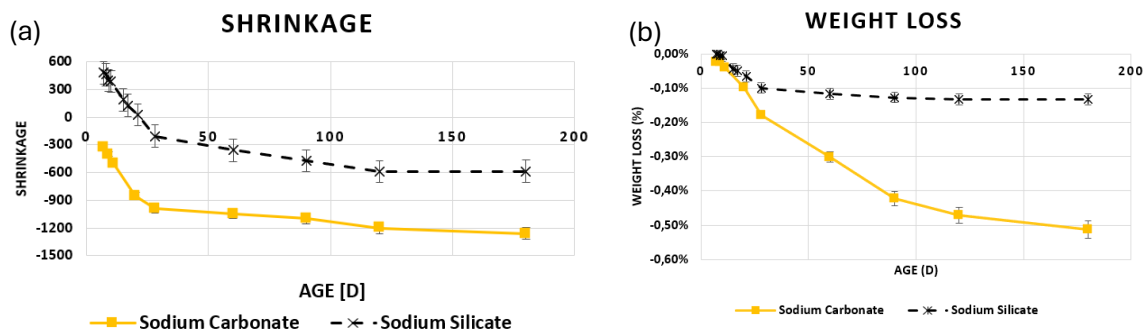


Figure 4.18: (a) Dry shrinkage and (b) weight loss of samples activated with sodium silicate and sodium carbonate under 7-day fog curing followed by sealed curing.



The dry shrinkage of the NS mortar was compared to CEM I and CEM III [210], as can be seen in Figure 4.19. The dry shrinkage of AAS activated by  $\text{Na}_2\text{SO}_4$  (NS) is reported to be approximately 4.4 times higher than that of ordinary Portland (OP) mortar, as indicated by the ratio 2900/660. This pronounced difference arises from the rapid early-age reaction kinetics and the nature of the C-(A)-S-H gel formed in AAS systems. The C-(A)-S-H gel has a lower Ca/Si ratio and a more disordered structure compared to the C-S-H gel in OPC, which makes it more susceptible to autogenous shrinkage due to self-desiccation during hydration [211].

In addition, AAS binders generally have higher chemical shrinkage and less free portlandite, which reduces the material's ability to buffer internal stresses. Under ambient drying, these effects are compounded, resulting in substantial microstructural contraction. In contrast, OP mortars benefit from a more gradual hydration and a more robust pore structure, which limits total shrinkage. The addition of  $\text{Na}_2\text{SO}_4$  accelerates the reaction and densifies the matrix, but it also increases capillary tension and thus amplifies dry shrinkage, resulting in a significantly higher dry shrinkage in the AAS than in OP mortar [212].

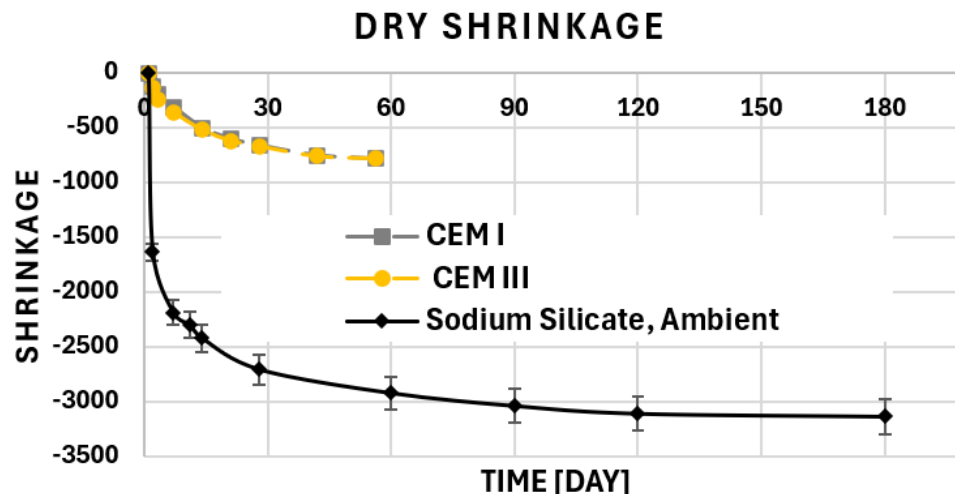


Figure 4.19: Dry shrinkage of NS, CEM I and CEM III mortar.

### **Mechanism of autogenous shrinkage of OPC**

Chemical shrinkage refers to the intrinsic volume reduction that occurs during the chemical reactions responsible for forming the binder phase in cementitious materials [213]. In Portland cement systems, hydration leads to a net decrease in volume because the solid hydration products occupy less space than the original reactants—cement and water [214]. Prior to setting, this reduction manifests as external shrinkage through paste collapse. Once the hydration products interconnect and create a rigid skeletal framework, further chemical shrinkage generates gas-filled voids within the paste matrix. As hydration progresses, continued water consumption causes capillary pores to empty, resulting in self-desiccation characterized by decreasing meniscus radii. The curvature of these menisci induces capillary tension, which contributes to autogenous shrinkage [214].

Wittmann et al. emphasized the importance of disjoining pressure as an alternative explanation for autogenous shrinkage during self-desiccation [215]. Although there remains ongoing debate regarding the dominant driving mechanism, several studies suggest that

capillary tension and disjoining pressure are interdependent or may act concurrently throughout this process [216]. Van Breugel [217] further noted that both mechanisms share mathematically similar formulations for describing volume change. Consequently, autogenous shrinkage in ordinary Portland cement can be effectively interpreted in terms of variations in either capillary tension or disjoining pressure—two interrelated phenomena intrinsically linked to self-desiccation [214].

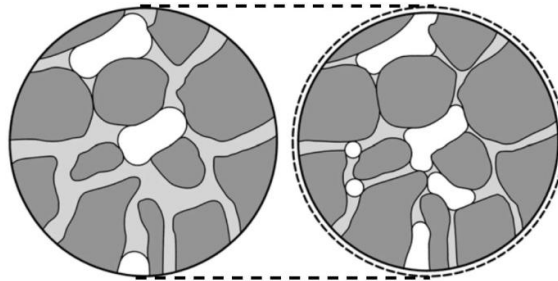


Figure 4.20: Schematic of hydrating cement paste. Left: low hydration degree; Right: high hydration degree. Dark grey denotes solids (hydrates and unhydrated cement), light grey indicates pore water, and white represents empty pores [214].

The reduction in internal relative humidity (RH) is widely recognized as a primary indicator of self-desiccation in cementitious materials. This internal RH is influenced by two key factors: the curvature of the liquid–vapor menisci within the pores and the ionic concentration of the pore solution [214], as expressed in Equation (4.1).

$$RH_K = \frac{RH}{RH_S} \quad (4.1)$$

Here, RH denotes the overall internal relative humidity of the paste,  $RH_S$  represents the relative humidity depression due to dissolved salts in the pore solution, and  $RH_K$  corresponds to the effect of meniscus curvature at the gas–liquid interface.

The meniscus radius can be determined using the Kelvin equation (Equation 4.2), which establishes the relationship between relative humidity and capillary pressure. Once the Kelvin radius is known, the tensile stress within the pore fluid can be evaluated using the Laplace equation (Equation 4.3).

$$r = \frac{2\gamma V_w}{\ln(RH_K) RT} \quad (4.2)$$

$$\sigma = -\frac{2\gamma}{r} \quad (4.3)$$

In these equations,

- $\sigma$  represents the tensile stress within the pore fluid (Pa)
- $r$  is the meniscus radius (m)
- $\gamma$  is the surface tension of the pore solution (N/m)
- $V_w$  is the molar volume of water ( $\text{m}^3/\text{mol}$ )
- $R$  is the universal gas constant ( $\text{J}/\text{mol}\cdot\text{K}$ )
- $T$  is the absolute temperature (K).

Bentz et al. [127] proposed that the linear autogenous shrinkage of cement paste subjected to capillary pressure can be expressed by Equation 4.4.

$$\varepsilon_{lin} = \frac{S \sigma}{3} \left( \frac{1}{K} - \frac{1}{K_s} \right) \quad (4.4)$$

In these equations,

- $S$  denotes the saturation degree (the ratio of liquid-filled to total pore volume)
- $\sigma$  represents the pore pressure (MPa)
- $K$  is the bulk modulus of the porous composite (GPa)
- $K_s$  refers to the bulk modulus of the solid phase (GPa).

It is important to note that this relationship primarily describes the elastic component of deformation and, therefore, provides only an approximation of the actual shrinkage behaviour [218].

### **Mechanism of autogenous shrinkage of AAS**

Given the structural resemblance between C–A–S–H and C–S–H gels [219], several researchers have proposed that similar mechanisms govern shrinkage behaviour in AAS systems [214, 220]. Consequently, the autogenous shrinkage of AAS has been interpreted through parameters such as pore size distribution, surface tension, degree of saturation, and elastic modulus.

Collins and Sanjayan [220] linked the pronounced autogenous shrinkage in AAS to its compact pore structure. Their study revealed that approximately 80% of the pores in  $\text{Na}_2\text{SiO}_3$ -activated AAS paste were mesopores (1.25–25 nm), compared to only 36.4% in OPC, which contained a higher proportion of macropores (25–5000 nm). This finer pore network in AAS leads to smaller meniscus radii and, therefore, higher capillary pressures [221]. Similar findings were reported by Lee et al. [157], who also confirmed the predominance of mesopores in AAS. Additionally, Ballekere Kumarappa et al. [222] observed that AAS pore solutions exhibit higher surface tension than OPC due to elevated ion concentrations, further amplifying the resulting capillary pressure (see Equation 4.3).

Beyond the influence of capillary pressure, both the degree of saturation and the stiffness of the cementitious matrix play crucial roles in determining autogenous shrinkage (see Equation 4.4). Cartwright et al. [223] demonstrated that AAS systems exhibit higher saturation levels and lower elastic moduli than OPC, resulting in greater autogenous shrinkage. From a microstructural standpoint, Ye and Radlińska [224] proposed that the significant shrinkage of AAS arises from the behaviour of the C–A–S–H gel. The incorporation of alkali cations was found to weaken the gel network, making it more prone to collapse and rearrangement under stress, thereby enhancing the viscoelastic and viscoplastic deformation of AAS.

While these studies differ in their perspectives, they generally share the assumption that capillary pressure serves as the principal driving force behind AAS autogenous shrinkage, similar to OPC. However, other researchers have challenged this view. Ma and Dehn [225] argued that self-desiccation alone cannot fully account for the substantially higher shrinkage observed in AAS compared with high-strength OPC, though they did not propose an alternative explanation. Uppalapati [226] suggested that shrinkage might also be linked to silica polymerization during the formation of C–A–S–H gels. Yet, previous studies [227, 228] indicate that the degree of silicon polymerization in C–A–S–H typically corresponds to  $Q^2$  units, comparable to those in C–S–H. Consequently, this mechanism appears insufficient to explain the markedly greater autogenous shrinkage of AAS.

#### 4.5.2. Effects of curing conditions

Figure 4.21 represent the dry shrinkage of sodium silicate-activated mortar samples under:

- Ambient curing from casting until the time of testing
- Fog-cured for 7 days followed by **ambient** curing until the time of testing
- Fog-cured for 7 days followed by **sealed** curing until the time of testing

Compared to the samples fog-cured for 7 days and then ambient-cured, continuous ambient curing led to approximately 202.7% (3138 / 1548) higher dry shrinkage at 180 days. Moreover, continuous sealed curing resulted in about 429.3% (3138 / 731) lower shrinkage compared to the ambient cured samples.

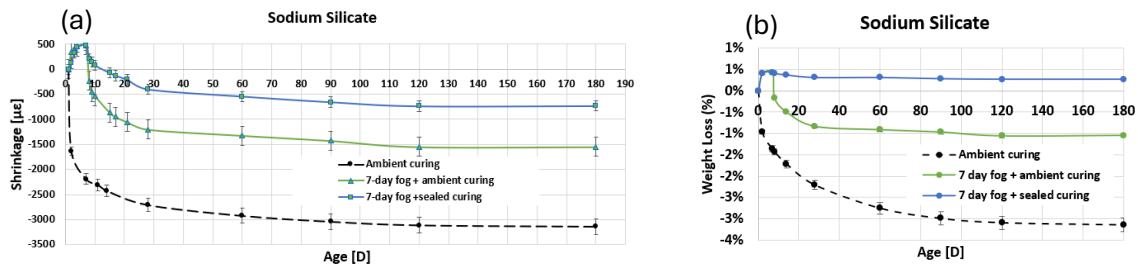


Figure 4.21: (a) Dry shrinkage and (b) weight loss of sodium silicate-activated samples under 1) ambient curing, 2) fog-cured for 7 days followed by ambient curing, and 3) fog-cured for 7 days followed by sealed curing over 180 days.

The results demonstrate that early-age curing has a significant influence on the long-term dry shrinkage of AAS. Specimens subjected to fog curing (relative humidity > 95%) for 7 days, followed by exposure to ambient conditions, exhibited markedly lower shrinkage compared to those continuously cured under ambient conditions. This observation is consistent with previous research [83, 229, 230, 84, 182, 106, 94, 230], which has shown that high-humidity environments help preserve pore water and suppress capillary stresses, thereby mitigating early-age shrinkage.

Dry shrinkage is strongly influenced by the relative humidity (RH) of the surrounding environment. A reduction in RH increases the vapor pressure gradient between the pore water and the ambient atmosphere, thereby accelerating moisture loss from the pore network. This intensified moisture loss induces higher capillary tension within the pores, ultimately leading to greater dry shrinkage. At RH levels below 50%, water in the finer capillary pores evaporates rapidly, generating tensile stresses along the pore walls that result in significant shrinkage. In contrast, high RH conditions ( $\geq 80\%$ ) slow down evaporation rates, reducing both the extent and severity of shrinkage-induced microcracking in terms of number and crack width. Furthermore, the reduced evaporation rate under these conditions contributes to a lower overall shrinkage magnitude [83].

Capillary tension is directly related to the relative humidity (RH) of the surrounding environment, as described by the Kelvin equation:

$$p = \frac{RT}{V_m} \ln(RH)$$

where,

- $R$  is the ideal gas constant [J/mol-K]
- $T$  is the absolute temperature [K]
- $RH$  is the relative humidity in the capillary pores [-]
- $V_w$  is the molar volume of water (m<sup>3</sup>/mol).

At low RH, water evaporates more rapidly from the pores, causing menisci to become more curved (smaller radius) and generating higher capillary tension, which leads to greater shrinkage. Conversely, at high RH, the meniscus radius is larger (flatter), producing lower capillary tension and reduced shrinkage. For example, at RH = 98%,  $\ln(0.98) = -0.02$ , whereas at RH = 55%,  $\ln(0.55) = -0.58$ ; this demonstrates that low RH produces significantly higher capillary tension compared to high RH. In AAS mortars, this effect contributes to the pronounced dry shrinkage observed under ambient curing, as the high capillary tension at lower humidity accelerates microstructural contraction and microcrack formation.

Figure 4.22 illustrates the relationship between relative humidity and the capillary tension generated within the pore liquid at a curing temperature of 20 °C. This curve was derived by combining the Laplace (4.3) and Kelvin equations (4.5) [231].

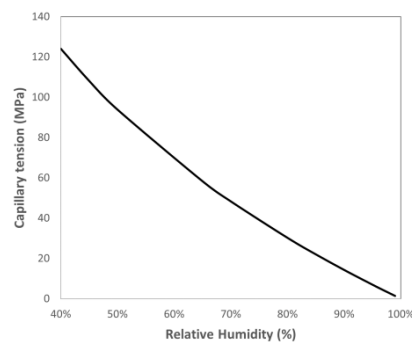


Figure 4.22: Relationship between relative humidity and capillary tension in the pore liquid, computed using the Kelvin–Laplace equation at 20 °C [231].

Additionally, sealing the samples immediately after fog curing effectively eliminated external moisture loss, as evidenced by negligible mass change. Nevertheless, shrinkage persisted under sealed conditions, indicating that internal mechanisms—such as chemical shrinkage and self-desiccation associated with ongoing hydration reactions and microstructural densification—also play a significant role in volumetric reduction, even in the absence of external drying (section 4.5.1). These findings underscore the importance of controlling both internal and external moisture dynamics during the early stages of curing to minimize dry shrinkage and improve dimensional stability in AAS systems.

### 4.5.3. Effect of the admixtures

#### 4.5.3.1. Gypsum

Figure 4.23 illustrates the effect of gypsum on the dry shrinkage of AAS mortars activated with sodium silicate under ambient curing.

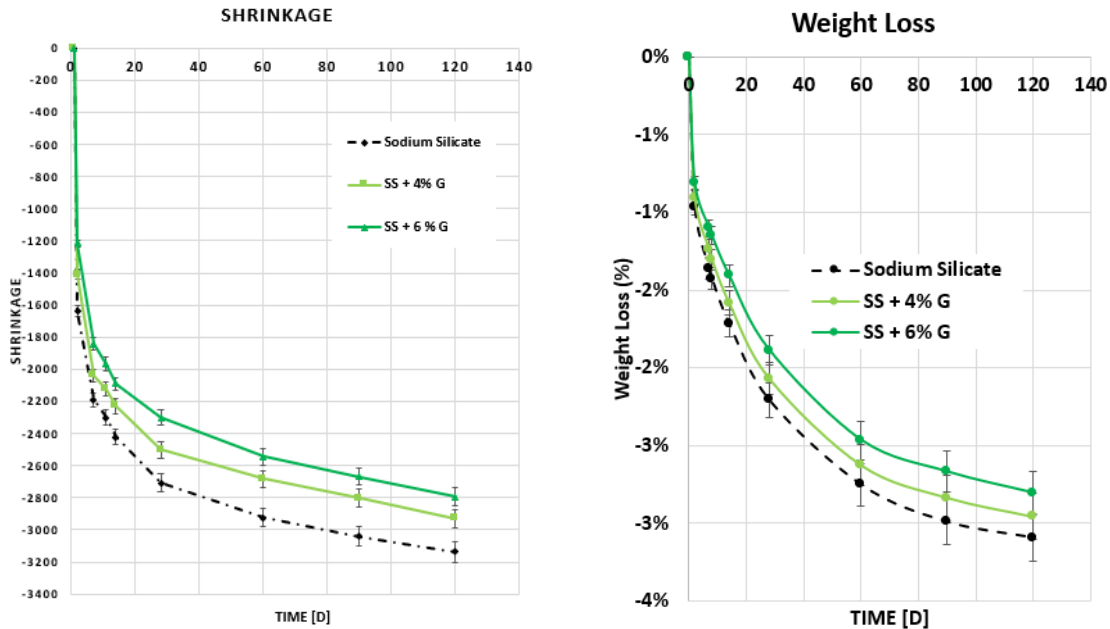


Figure 4.23: (a) Dry shrinkage and (b) weight loss of sodium silicate with and without gypsum under ambient curing condition.

Adding 6% gypsum reduces the dry shrinkage by an average of 30%, where gypsum-modified mortars exhibit slightly lower moisture loss over time. The reduction in dry shrinkage observed with gypsum addition is consistent with previous research [41, 191]. Gypsum supplies additional calcium ( $\text{Ca}^{2+}$ ) and sulfate ( $\text{SO}_4^{2-}$ ) ions, which react with available aluminat species to form ettringite (AFt) and monosulfate (AFm) phases. These expansive hydration products help offset shrinkage-related volume reductions while also filling capillary pores. Their precipitation refines the pore structure, reducing pore connectivity and permeability, which in turn suppresses internal moisture transport, capillary stress development, and subsequent dry shrinkage [232]. Moreover, the porous nature of ettringite enables additional water retention, slowing moisture loss under drying conditions. In  $\text{CO}_2$ -rich environments, calcium ions released from gypsum may precipitate as calcium carbonate ( $\text{CaCO}_3$ ), further densifying the matrix and improving volumetric stability by providing slight expansion that counteracts shrinkage.

Additionally, gypsum enhances the incorporation of  $\text{SO}_4^{2-}$  ions, which not only combine with  $\text{Na}^+$  from the activator or dissolved slag to form sodium sulfate ( $\text{Na}_2\text{SO}_4$ ) crystals [84], but also promote ettringite formation through reaction with  $\text{Al}^{3+}$  released from slag. This expansion mechanism has been consistently confirmed in previous studies [191, 25]. The samples in Figures 4.24 are identical to those in 4.23 but subjected to different curing regimes: 7-day fog curing followed by ambient curing in (a, b), and 7-day fog curing followed by sealed curing in (c, d).



The sealed samples maintained a constant weight over time, confirming effective isolation from external drying and retention of internal moisture. Consequently, sealed curing samples exhibit lower dry shrinkage than samples exposed to ambient conditions, as the absence of external water loss suppresses capillary stress development and thus reduces shrinkage.

The sealed samples exhibit shrinkage despite maintaining a constant weight, as the reaction between the alkaline activator and slag induces autogenous shrinkage due to the chemical reactions between the alkaline activator and the slag. Upon activation, the alkaline solution rapidly dissolves calcium, silicon, and aluminum species from the slag, which then recombine to form hydration products such as calcium (alumino)silicate hydrate (C-(A)-S-H) gel and hydrotalcite-like phases. The precipitation of these phases consumes water from the pore solution, binding it chemically and physically within the hydration products. This reduction in free pore water lowers the internal relative humidity of the system, leading to self-desiccation. As hydration progresses in a fine pore network, capillary stresses develop due to the menisci formed in partially saturated pores. These stresses generate internal tensile forces that drive volume reduction, manifesting as autogenous shrinkage, even under sealed conditions without external moisture loss. The effect is particularly pronounced in AAS due to its rapid reaction kinetics and highly refined pore structure [202, 233, 234].

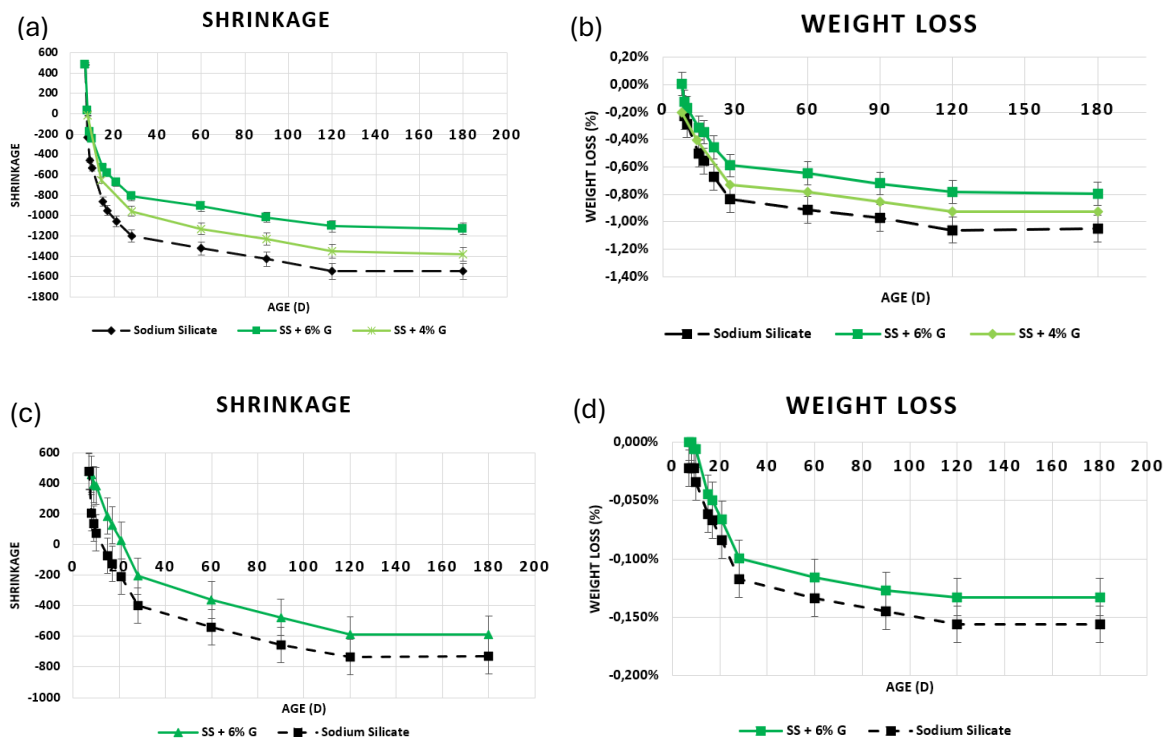


Figure 4.24: Dry shrinkage and weight loss of sodium silicate-activated samples with/without gypsum under 7-day fog curing followed by (a, b) **ambient** curing conditions and (c, d) **sealed** curing conditions.

#### 4.5.3.2. Air-entraining agent

Figure 4.25 illustrates the dry shrinkage behaviour of sodium silicate–activated samples with and without the incorporation of an air-entraining agent (AEA) over a 120-day period. All samples underwent 7 days of fog curing, followed by ambient exposure until the time of testing. The results demonstrate that the inclusion of AEA resulted in only minor reductions in dry shrinkage over the duration of the study.

The principal mechanism through which air-entraining agents (AEA) reduce dry shrinkage is by alleviating capillary pressure within the pore structure. As AAS dries, the evaporation of pore water creates curved liquid–air menisci within the capillaries. The curvature of these menisci generates a negative capillary pressure (suction) that draws the solid matrix inward, causing volumetric contraction. This pressure is described by the Laplace equation  $[\Delta P = 2 \cdot \gamma \cdot \cos(\theta) / r]$ , indicating that finer pores with smaller radii ( $r$ ) produce higher tensile stresses in the solid skeleton [235].

The incorporation of AEA introduces a uniformly distributed system of microscopic, discrete air bubbles—typically ranging from 10 to 300  $\mu\text{m}$ —that interrupt the continuity of the capillary pore network [236]. These air voids, being non-water-filled, act as breaks in the capillary channels, preventing the formation of long, continuous menisci and thereby reducing the capillary tension developed during drying. The bubbles serve as stress-relief points within the pore system, limiting the transmission of negative pressure and mitigating the resulting tensile stress within the matrix [236].

The reduction in mass loss is closely related to the decrease in effective capillary porosity and the mitigation of internal capillary stresses, both of which help retain moisture within the matrix [237]. Therefore, AEA reduces dry shrinkage and mass loss of AAS primarily by lowering capillary pressure.

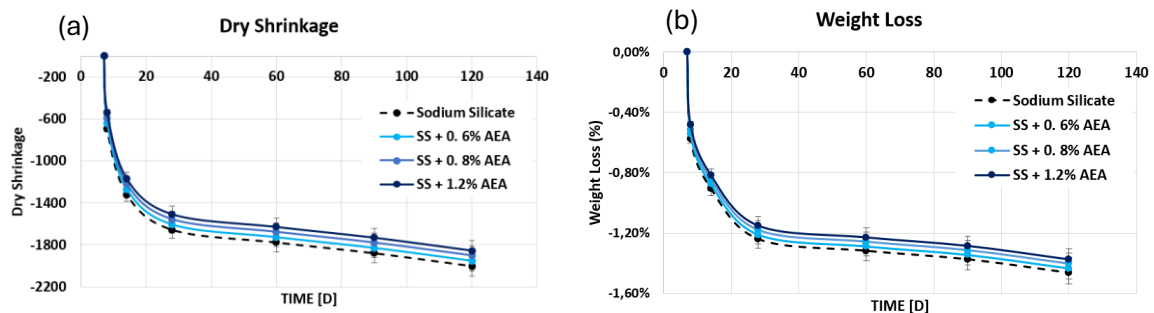


Figure 4.25: (a) Dry shrinkage and (b) weight loss of sodium silicate activated samples under 7-day fog curing followed by ambient curing condition with and without air-entraining agent.

#### 4.5.3.3. Shrinkage reduction admixtures

Figure 4.26 presents the dry shrinkage behaviour of sodium silicate–activated samples with and without the addition of a shrinkage-reducing admixture (SRA) over a 120-day period. All specimens were fog-cured for 7 days and subsequently exposed to ambient conditions until testing. The results indicate that incorporating SRA led to only a slight decrease in dry shrinkage throughout the observed period.

SRA mitigates dry shrinkage and mass loss in AAS systems primarily through modification of the pore solution's surface tension, thereby reducing capillary pressure that develops as water evaporates from the microstructure. In AAS binders, the fine pore network—typically dominated by mesopores in the range of 10–100 nm—creates strong capillary stresses during drying due to meniscus formation within the pores. These stresses lead to volumetric contraction of the solid matrix, resulting in dry shrinkage. SRA, which often consist of non-ionic surfactants such as polypropylene glycol or polyether derivatives, lower the surface

tension ( $\gamma$ ) of the pore liquid and consequently reduce the capillary pressure ( $P_k$ ), as described by the Laplace equation  $[\Delta P = 2 \cdot \gamma \cdot \cos(\theta) / r]$ , where  $\theta$  is the contact angle and  $r$  is the pore radius. By reducing  $\gamma$ , the internal suction forces are decreased, directly diminishing the driving force for shrinkage [238].

In alkali-activated materials, SRA also influence the hydration kinetics and gel formation. The presence of SRA molecules at the solid–liquid interface can adsorb onto slag particles and hydration products, thereby modifying dissolution rates and the morphology of calcium–aluminosilicate–hydrate (C–A–S–H) gels. This can slightly retard reaction rates and alter the connectivity of the pore network [239]. Despite this, the reduction in internal capillary tension generally leads to lower shrinkage values, especially in AAS systems where capillary stresses are more severe than in Portland cement due to finer gel pore structures [240]. In summary, SRAs reduce dry shrinkage and mass loss in AAS by lowering surface tension and mitigating capillary-induced stresses during moisture loss.

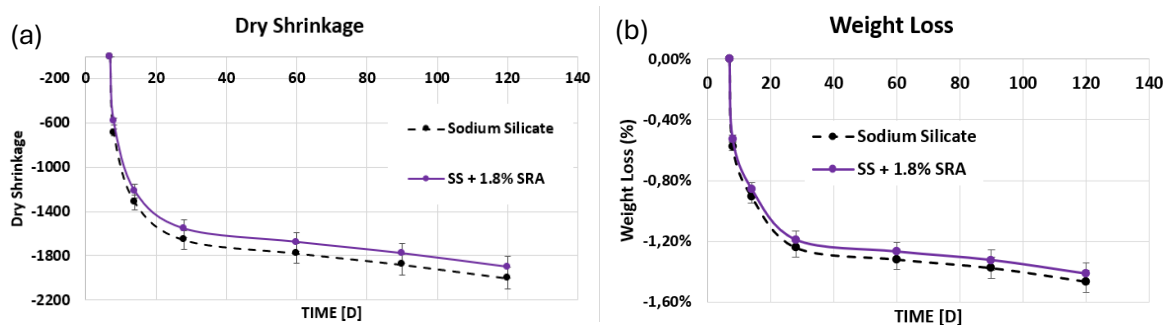


Figure 4.26: (a) Dry shrinkage and (b) weight loss of sodium silicate activated samples under 7-day fog curing followed by ambient curing condition with and without shrinkage-reducing admixture.

#### 4.5.4. Dry shrinkage and weight loss of AAS concrete

As established in Section 4.5.1, sodium silicate–activated slag exhibits significantly lower dry shrinkage compared to sodium carbonate–activated systems. Among the tested curing regimes, fog curing for 7 days proved to be the most effective in mitigating shrinkage. Additionally, the incorporation of 6% gypsum was identified as the most beneficial admixture for shrinkage reduction. Accordingly, this section focuses on sodium silicate–activated samples with and without 6% gypsum, all subjected to 7 days of fog curing followed by both sealed and ambient curing. Ambient curing was selected for subsequent testing to reflect conditions commonly encountered in practical engineering applications.

The dry shrinkage and weight loss results of the concrete specimens are presented in Figure 4.27. As shown in Figures 4.20 (a) and (b), the observed trends are similar to those in the mortar samples, indicating that curing conditions and gypsum addition have a comparable effect on shrinkage and moisture loss, consistent with the findings in Sections 4.5.3. Nonetheless, the dry shrinkage of concrete specimens is consistently lower than that of their mortar counterparts. After 180 days of curing:

- Concrete without gypsum exhibited a dry shrinkage of approximately 900  $\mu\text{m/m}$ , whereas the equivalent mortar sample reached around 1500  $\mu\text{m/m}$ .
- Concrete with 6% gypsum showed a reduced shrinkage of about 700  $\mu\text{m/m}$ , while the corresponding gypsum-modified mortar reached approximately 1100  $\mu\text{m/m}$ .

This significant reduction in shrinkage of AAC compared to AAS mortar is primarily attributed to the presence of coarse aggregates within the concrete matrix. These aggregates introduce mechanical restraint, reduce the volume of shrinkage-susceptible binder, and disrupt capillary continuity, thereby limiting dimensional changes under drying conditions. Additionally, the extent of shrinkage is influenced by the surface area exposed to drying. Slender or small members lose moisture faster than larger, thicker elements over the same drying duration. Additionally, the moisture gradient is typically more pronounced near the surface compared to the interior of the member. While gypsum continues to improve shrinkage resistance through its chemical and microstructural effects, its relative impact is less pronounced in concrete due to the mitigating influence of aggregates.

The difference in dry shrinkage behaviour between sodium silicate-activated mortar and concrete can be mainly attributed to a combination of factors, including mix design, pore structure, and internal stress distribution. Concrete contains a substantially higher volume of coarse aggregates than mortar, providing internal stiffness and mechanical resistance to volumetric deformation. These rigid inclusions interrupt the continuity of the binder matrix and reduce the overall shrinkage strain by redistributing stresses generated by drying [86]. Moreover, Coarse aggregates enhance the redistribution of internal stresses, lowering the risk of cracking due to localized strain concentrations.

As a result, concrete exhibits improved dimensional stability during drying compared to mortar. Furthermore, The interfacial transition zone (ITZ) between the binder and coarse aggregates in concrete influences moisture transport and shrinkage development. Although the ITZ is often more porous, the presence of large aggregates disrupts capillary networks and reduces moisture migration, thereby mitigating tensile stress accumulation and subsequent shrinkage [87, 29].

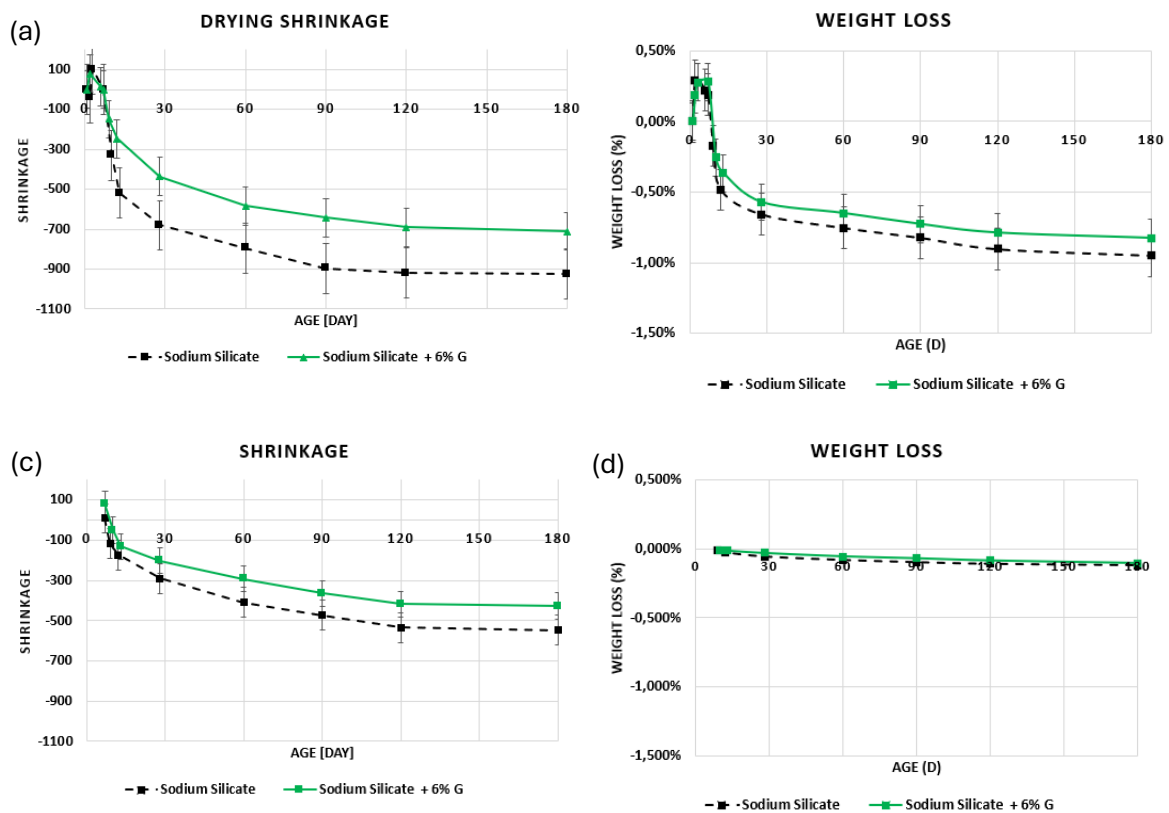


Figure 4.27: Dry shrinkage and weight loss of sodium silicate-activated concrete with/without gypsum under 7-day fog curing followed by (a, b) **ambient** curing conditions and (c, d) **sealed** curing conditions.

The dry shrinkage of the NS mortar was compared to CEM I [241], under 7-day fog curing followed by ambient curing, as can be seen in Figure 4.28. The 180-day dry shrinkage of alkali-activated concrete (AAC) was approximately 2.4 times higher than that of ordinary Portland cement (OPC), as indicated by the ratio 925 / 383. This substantial difference arises from the distinct microstructural characteristics and shrinkage mechanisms of AAC compared to OPC. AAC develops a C-(A)-S-H gel with a lower Ca/Si ratio and a more disordered structure than the C-S-H gel in OPC. This gel structure is more prone to autogenous shrinkage due to self-desiccation during early hydration and exhibits higher capillary stresses under drying conditions (section 4.5.1). Additionally, AAC lacks the portlandite buffering present in OPC, which normally mitigates microcrack formation and volumetric contraction (section 4.5.2). As a result, under ambient curing, the combination of high autogenous shrinkage, microcrack development, and capillary tension leads to a dry shrinkage that is significantly greater than that observed in OPC systems.

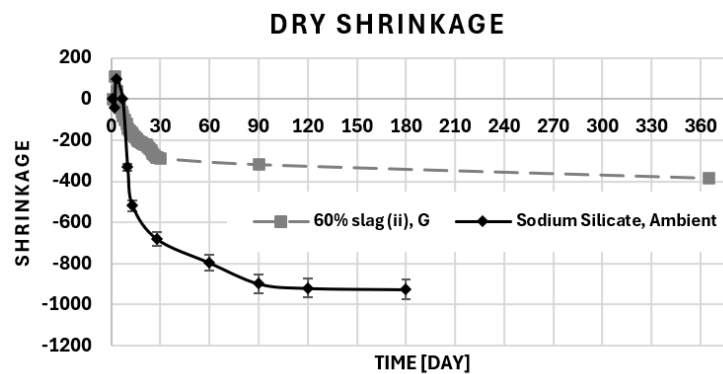


Figure 4.28: Dry shrinkage of OPC and AAC.

#### 4.5.5. Comparison dry shrinkage with Predicted Model Codes

The experimentally measured age-dependent dry shrinkage of AAS mortars and concrete was compared with predictions from several widely used models, including ACI 209 [205] and CEB 90 [206], as illustrated in Figure 4.29 and 4.30. A summary of the models recommended by these codes and researchers for dry shrinkage prediction is provided in Table 4.2. This comparison allows evaluation of the accuracy of standard predictive models against the actual dry shrinkage behaviour of AAC over time.

Table 4.2: Models for age-dependent dry shrinkage [242].

ACI 209 [205]	$\varepsilon_{sh}(t) = 1.54 \frac{t}{35+t} \varepsilon_{sh}(u)$
CEB 90 [206]	$\varepsilon_{sh}(t) = 1.75 \frac{t}{32+t} \varepsilon_{sh}(u)$

The predictions of ACI 209 for long-term dry shrinkage are reasonably consistent with the experimental results for AAS mortars under both curing conditions (ambient curing and 7-day fog curing followed by ambient curing), as illustrated in Figures 4.29 and concrete (7-day fog curing followed by ambient curing) Figure 4.30. This suggests that, despite being developed primarily for Portland cement-based systems, the ACI 209 model can capture the general trend of long-term shrinkage in AAS.

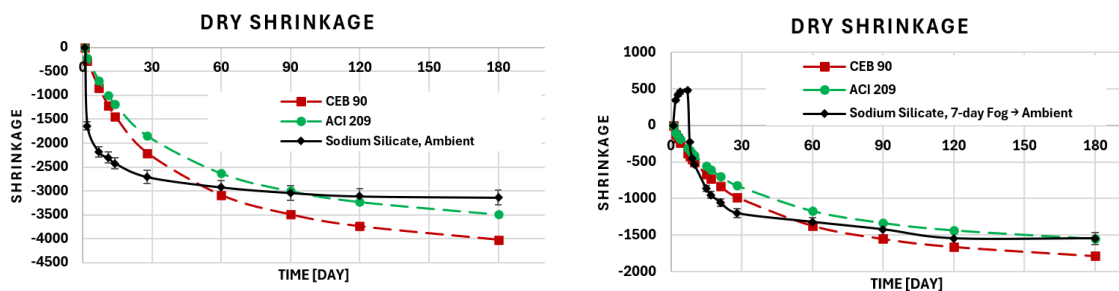


Figure 4.29: Comparison of the dry shrinkage of AAS mortar with predictions from various model codes under (a) ambient curing and (b) 7-day fog curing followed by ambient curing.

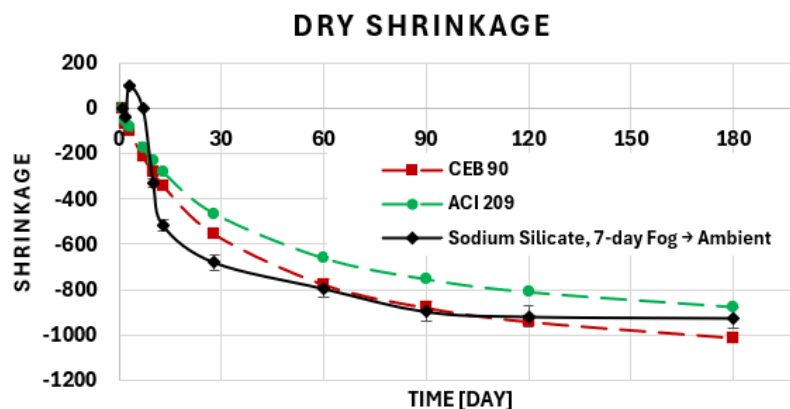


Figure 4.30: Comparison of the dry shrinkage of AAC with predictions from various model codes under 7-day fog curing followed by ambient curing.



#### 4.5.6. Correlation between dry shrinkage and flexural strength & modulus of elasticity

Figure 4.31 illustrates the correlation between dry shrinkage and the mechanical properties (elastic modulus (E-modulus) and flexural strength) of AAS mortar subjected to 7-day fog curing followed by ambient curing. During the first 7 days, fog curing maintains a high relative humidity, which reduces early-age moisture loss. This prevents the formation of microcracks and promotes the development of a denser microstructure, resulting in simultaneous increases in E-modulus and flexural strength while dry shrinkage reduces.

When the specimens are subsequently exposed to ambient curing, the relative humidity decreases, leading to gradual dry shrinkage. This shrinkage induces tensile stresses within the matrix, which can cause microcracking or opening of previously formed pores. Consequently, the growth of elastic modulus and flexural strength reduces, reflecting a slight loss of mechanical stability.

Over longer periods, between 120 and 180 days, both dry shrinkage and mechanical properties stabilize. This stabilization occurs because the ongoing hydration and polymerization of C–A–S–H gel continues to densify the microstructure, filling capillary pores and mitigating further shrinkage. Additionally, the internal stresses generated by early-age shrinkage are partially relieved over time as the material accommodates volume changes, allowing the mechanical properties to plateau.

Overall, this figure demonstrates that early-age curing under high humidity reduces shrinkage-induced microcracking, supporting stronger and stiffer AAS mortars. Later ambient drying leads to minor reductions in properties, but long-term stabilization reflects the interplay between ongoing hydration, microstructural densification, and stress redistribution within the material.

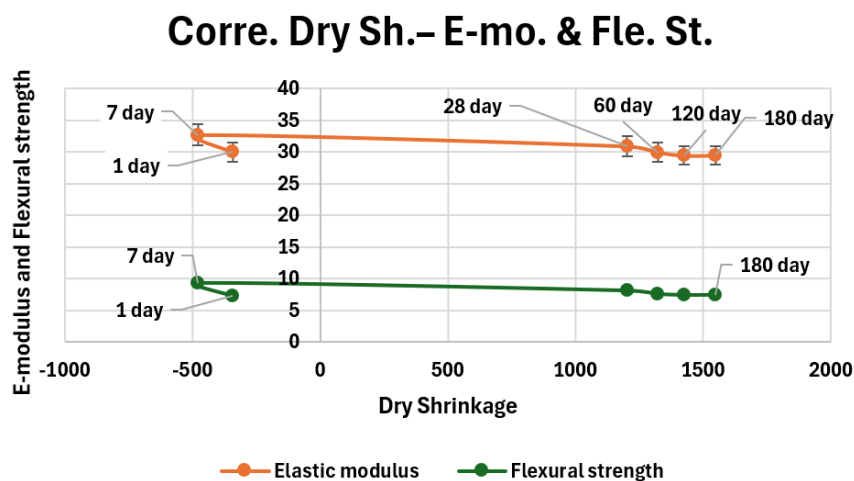


Figure 4.31: Correlation between dry shrinkage and flexural strength & modulus of elasticity.

## 4.6. XRD analysis

Figure 4.32 (a) presents the X-ray diffraction (XRD) patterns of sodium silicate-activated samples cured under ambient conditions, while Figure 4.32 (b) displays the corresponding results for samples subjected to a 7-day fog curing regime. Figure 4.32 (c) illustrates the XRD results of sodium silicate-activated samples with an additional 6% gypsum content, also fog-cured for 7 days. Figure 4.32 (d) shows the XRD patterns for sodium carbonate-activated samples subjected to the same fog curing treatment.

The phase assemblage of sodium silicate-activated samples was largely consistent across both curing conditions, predominantly comprising calcite, amorphous gels, and hydrotalcite phases. The addition of 6% gypsum induced the formation of additional crystalline phases, notably fayalite, ettringite, and gypsum. In contrast, sodium carbonate-activated samples exhibited distinct phase development, including the presence of zeolite, gaylussite, and vaterite.

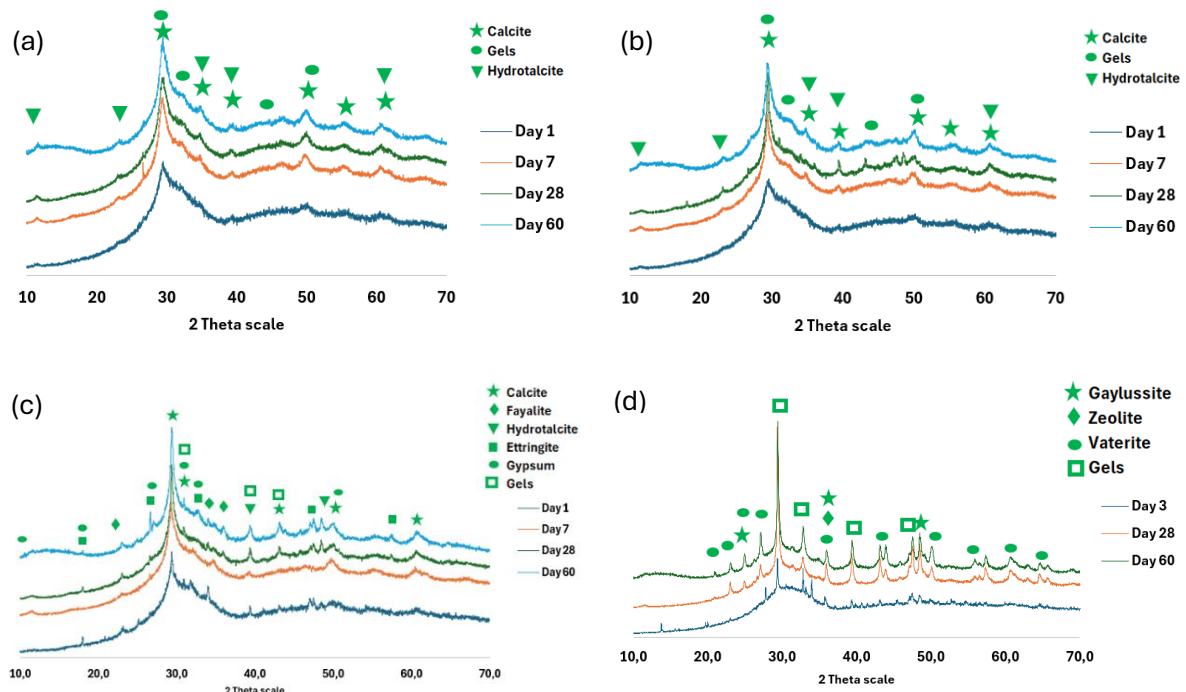
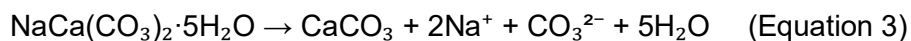


Figure 4.32: XRD patterns of sodium silicate activated mortar under (a) ambient curing, (b) 7-day fog curing, (c) 7-day fog curing with 6% gypsum, and (d) sodium carbonate activated mortar under 7-day fog curing.

In the early stages of the reaction, calcium ions ( $\text{Ca}^{2+}$ ) preferentially interact with carbonate ions ( $\text{CO}_3^{2-}$ ) supplied by the sodium carbonate activator, leading to the precipitation of calcium carbonate and gaylussite. Simultaneously, the aluminosilicate phase of GGBFS reacts with sodium ions from the activator to form zeolite NaA. However, these early reaction products provide limited cohesion, resulting in slow development of early-age mechanical strength due to the moderate pH environment established by  $\text{Na}_2\text{CO}_3$ . Once the carbonate ions are depleted, the reaction mechanism transitions to one similar to that observed in NaOH-activated slag binders, producing characteristic binder phases such as calcium aluminium silicate hydrate (C-A-S-H), hydrotalcite, and Ca-heulandite, a calcium- and aluminium-rich zeolitic phase [83].

The decomposition of gaylussite significantly contributes to increased porosity and the release of chemically bound water, both of which exacerbate dry shrinkage over time [188, 189]. This enhanced shrinkage arises from elevated water evaporation, sourced from residual unreacted water due to dilution and from water released by the breakdown of crystalline phases like gaylussite. Gaylussite—a common secondary phase in sodium carbonate-activated slag systems—is thermodynamically unstable under drying conditions and undergoes dehydration as represented by the reaction:



This reaction liberates chemically bound water, leading to mass loss and increased dry shrinkage [189]. Yuan et al. [188] corroborate the progressive decomposition of gaylussite and the consequent release of free water, which negatively impacts mechanical properties by elevating shrinkage.

The addition of gypsum promotes the formation of ettringite, which has been associated with improved compressive strength due to its expansive nature. Ettringite crystals fill pore spaces and refine the microstructure, and their porous morphology enables retention of additional water, thereby potentially reducing moisture loss in drying conditions. However, gypsum incorporation may also retard compressive strength development. This retardation is linked to the slower dissolution of slag particles, as gypsum reduces the system's pH through its conversion into more stable phases such as portlandite and sodium sulfate under highly alkaline conditions. The consequent decrease in pH impedes slag dissolution and delays the precipitation of calcium-aluminium-silicate-hydrate (C-A-S-H) gel, thus reducing early strength gain [84]. Despite this delay, the early formation of ettringite—a sulfate-rich expansive hydration product—partially counteracts dry shrinkage through its pore-filling and expansive effects.

## 4.7. Summary and limitations

### 4.7.1. Summary Tables

The following tables provide a comprehensive comparative summary of the key findings from this study, highlighting the influence of activator type, curing regime, and admixture use on the dry shrinkage and mechanical properties of AAS systems. Table 4.3 summarizes the effects of sodium silicate versus sodium carbonate activation, fog and ambient curing, and 6% gypsum addition on dry shrinkage, compressive and flexural strength, elastic modulus, and microstructural mechanisms. Table 4.4 compares the performance of AAS mortar and concrete, illustrating the role of coarse aggregates in mitigating shrinkage and enhancing stiffness. Table 4.5 extends the comparison to conventional ordinary Portland cement concretes (CEM I and CEM III), providing mechanistic explanations for differences in shrinkage behaviour, strength development, and elastic properties. Finally, Table 4.6 presents correlations between mechanical properties and dry shrinkage under different curing conditions, highlighting how early-age humidity control influences the evolution of strength, stiffness, and dimensional stability. Collectively, these tables synthesize the experimental results and mechanistic insights, providing a clear framework for understanding the interrelated effects of mix design, curing, and microstructure on the long-term performance of AAS systems.

Table 4.3 summarizes the effects of activator type, curing regime, and gypsum addition on the dry shrinkage, mechanical properties, and microstructure of AAS mortars.

Table 4.3: Comparative Summary: AAS Shrinkage & Mechanical Properties.

Category	Sodium Silicate (NS)	Sodium Carbonate (NC)	Fog Curing (7 days)	Ambient Curing	6% Gypsum Addition
<b>Dry Shrinkage</b>	Lowest shrinkage due to dense C–A–S–H network; reduced porosity and limited microcracking	Highest shrinkage due to higher porosity & moisture loss	Strongly reduces shrinkage; high RH suppresses capillary tension and microcracking	Highest shrinkage due to moisture loss and higher capillary tension	Significantly reduces shrinkage via formation of Aft/AFm and pore refinement; possible slight expansion
<b>Compressive Strength</b>	Highest strength; strong gel formation and rapid polymerisation	Lowest strength; insufficient C–(A)–S–H formation	Increased strength; reduced microcracking and improved hydration	Lower strength; continuous moisture loss induces microcracks	Slight early delay, but increases over time due to densified microstructure
<b>Flexural Strength</b>	Higher because dense matrix limits crack growth	Lower due to weak matrix and microcracking	Increased flexural strength due to reduced shrinkage cracking	Reduced over time; cracking dominates	Improves long-term flexural strength through shrinkage reduction
<b>Elastic Modulus</b>	Highest E-modulus due to dense, cohesive microstructure	Lowest E-modulus due to porosity and microcracks	Increased stiffness; moisture retention reduces microcracking	Reduced stiffness followed by slight recovery	Minimal impact; gypsum does not significantly stiffen the primary C–A–S–H skeleton
<b>Microstructure Mechanisms</b>	Well-polymerised C–A–S–H, refined pores, high cohesion	Poorly formed gels, high porosity, weak matrix	Maintained RH → suppressed capillary tension → pore refinement	Rapid drying → capillary tension, microcracking, pore coarsening	Aft/AFm fill pores; microstructure densifies over time
<b>Overall Performance Rating</b>	Best overall	Poorest overall	Best curing regime	Weakest curing regime	Beneficial for shrinkage

Table 4.4 compares the mechanical performance and shrinkage behaviour of AAS mortar and concrete, highlighting the influence of coarse aggregates on stiffness and dimensional stability.

Table 4.4: Comparative Summary: AAS Mortar vs Concrete.

	Dry Shrinkage	Compressive Strength	Flexural Strength	Elastic Modulus	Microstructure Mechanisms
<b>AAS Mortar</b>	Highest shrinkage due to lack of coarse aggregates	Moderate strength; matrix-dominated behaviour	Often higher flexural than concrete due to uniform matrix	Lower E-modulus due to paste-dominated behaviour	More porous; microcracks more pronounced
<b>AAS Concrete</b>	~30–40% lower shrinkage than mortar across curing regimes; aggregates provide restraint	Higher strength due to aggregate interlock and stress redistribution	Lower than mortar; aggregates disrupt matrix continuity	Higher E-modulus; aggregates carry load and provide stiffness	Strong aggregate–matrix interaction limits deformation

Table 4.5 presents a comparison between AAS and ordinary Portland cement systems (CEM I and CEM III), with mechanistic explanations for differences in shrinkage, strength development, and elastic modulus.

Table 4.5: Comparative Summary: AAS vs OPC (Mortar & Concrete).

Property	AAS (Na <sub>2</sub> SO <sub>4</sub> Activated)	OPC (CEM I, CEM III)	Key Reason / Mechanistic Explanation
<b>Dry Shrinkage (Mortar)</b>	Very high: ~4.4× higher shrinkage than OPC mortar (2900 vs 660 µstrain).	Much lower dry shrinkage.	<ul style="list-style-type: none"> <li>AAS has finer mesopores (1.25–25 nm) → high capillary tension.</li> <li>Higher surface tension of pore solution.</li> <li>Lower stiffness &amp; no portlandite to buffer shrinkage.</li> </ul>
<b>Dry Shrinkage (Concrete)</b>	~2.4× higher 180-day shrinkage than OPC concrete (925 vs 383 µstrain).	Lower shrinkage due to gradual hydration & more stable pore structure.	<ul style="list-style-type: none"> <li>AAS: high autogenous shrinkage + microcracks + high capillary tension.</li> <li>OPC: robust pore structure + portlandite buffering + lower capillary stresses.</li> </ul>
<b>Compressive Strength (Mortar)</b>	<ul style="list-style-type: none"> <li>Higher early-age strength than OPC.</li> <li>Enhanced by Na<sub>2</sub>SO<sub>4</sub> addition and solid (one-part) activators → up to <b>20 MPa</b> higher early strength than liquid AA</li> </ul>	Lower early-age strength, but strong continuous long-term development (due to C <sub>3</sub> S, C <sub>2</sub> S hydration and slag reaction in CEM III).	<ul style="list-style-type: none"> <li>Solid AA dissolves gradually → prevents flash setting, reduces pore formation.</li> <li>Na<sub>2</sub>SO<sub>4</sub> densifies matrix; OPC develops slower but stable C–S–H gel over time.</li> </ul>
<b>Compressive Strength (Concrete)</b>	<ul style="list-style-type: none"> <li>Higher early and long-term strength than OPC concrete.</li> <li>Denser microstructure due to Na<sub>2</sub>SO<sub>4</sub> addition.</li> </ul>	Strength increases steadily with time for both CEM I and CEM III.	AAS forms compact C–(A)–S–H rapidly; OPC gains strength through progressive clinker and slag hydration.
<b>Flexural Strength (Mortar)</b>	<ul style="list-style-type: none"> <li>Often decreases over time.</li> <li>NS mortar declines due to shrinkage and microcrack formation.</li> </ul>	Increases steadily (CEM I 42.5N and CEM III/B).	<ul style="list-style-type: none"> <li>AAS gel is brittle, higher shrinkage → loss in tensile capacity.</li> <li>OPC gains flexural strength due to ongoing C–S–H formation and ITZ improvement.</li> </ul>
<b>Flexural Strength (Concrete)</b>	Decreases over time under ambient curing (AAC), stabilising after ~3 months.	Increases with age (CEM I 42.5 R-NA, CEM III/A 42.5 HSR-NA).	AAS undergoes continued autogenous & dry shrinkage → microcracks.
<b>Elastic Modulus (Mortar)</b>	Decreases over time.	Increases continuously over time (CEM I & CEM III/B).	<ul style="list-style-type: none"> <li>AAS: high autogenous &amp; dry shrinkage → microcracks reduce stiffness.</li> <li>OPC: continued hydration refines microstructure → stiffer matrix.</li> </ul>
<b>Elastic Modulus (Concrete)</b>	Lower E-modulus long-term due to shrinkage-induced microcracks.	Strong increase in E-modulus over time	AAS C–(A)–S–H is brittle; OPC hydration fills pores and strengthens ITZ.
<b>Sensitivity to Curing (Concrete)</b>	Shrinkage significantly lower than AAS mortar, but still higher than OPC.	Less dependent on controlled early curing.	Capillary stresses and self-desiccation are higher in AAS (NS) due to a denser microstructure.
<b>Microstructure</b>	<ul style="list-style-type: none"> <li>C–(A)–S–H gel: lower Ca/Si, highly cross-linked, brittle.</li> <li>High mesopore fraction (~80% in Na<sub>2</sub>SiO<sub>3</sub> systems).</li> </ul>	C–S–H gel: gradual densification; more macropores initially.	AAS microstructure more susceptible to self-desiccation and cracking
<b>Autogenous Shrinkage Mechanism</b>	<ul style="list-style-type: none"> <li>Dominated by capillary pressure in fine pores.</li> <li>Higher surface tension &amp; saturation → more shrinkage</li> </ul>	Capillary tension and disjoining pressure contribute, but magnitude is smaller; buffered by portlandite.	AAS has finer pores, higher internal stresses, weaker gel → larger autogenous shrinkage.

Table 4.6 illustrates the relationships between dry shrinkage and key mechanical properties under different curing conditions..

Table 4.6: Correlations Between Mechanical Properties and Dry Shrinkage for AAS.

Correlation Type	Curing	Trend	Mechanistic Explanation
<b>Compressive Strength vs. E-Modulus</b>	Ambient	Compressive strength increases; E-modulus decreases	Autogenous and dry shrinkage induce microcracks; brittle C–(A)–S–H gel reduces ability to resist elastic deformation
	7-day fog curing + ambient	Both increase initially; slight decrease in E-modulus under ambient curing	Early fog curing reduces shrinkage and microcracking, promoting initial gel formation; later ambient drying induces minor microcracks
<b>Compressive Strength vs. Flexural Strength</b>	Ambient	Compressive strength increases; flexural strength decreases	Microcracking from dry and autogenous shrinkage reduces tensile capacity
	7-day fog curing + ambient	Flexural strength increases initially, then, small reduction and stabilizes over 90 day.	Fog curing limits early microcracking; ambient drying induces minor crack formation
<b>Dry Shrinkage vs. E-Modulus &amp; Flexural Strength</b>	Ambient	Increasing shrinkage corresponds to decreasing E-modulus and flexural strength	Shrinkage-induced tensile stresses cause microcracking, reducing stiffness and tensile performance
	7-day fog curing + ambient	Minimal shrinkage during fog curing; E-modulus and flexural strength increase; later ambient shrinkage induces slight reductions	Early-age humidity reduces shrinkage and microcracking; later ambient drying allows minor cracking, but long-term hydration densifies microstructure and stabilizes properties

#### 4.7.2. Limitations of the Study

Despite providing valuable insights into the shrinkage and long-term mechanical behaviour of AAS mortars and concretes, this study has several limitations:

- 1) **Microstructural Analysis:** Variability in slag composition and the limited scope of microstructural techniques, such as MIP, may influence the generalizability of the observed pore structure–property relationships.
- 2) **Scale-Up Effects:** All experiments were conducted on laboratory-scale specimens. The performance of larger structural elements may differ due to factors such as internal restraint, heat evolution, and differential curing.
- 3) **Environmental Exposure:** The study focused on controlled curing conditions and did not account for long-term environmental effects, including temperature fluctuations, wetting/drying cycles, or exposure to aggressive chemicals.
- 4) **Time Frame:** The study tracked properties for up to six months; longer-term behaviour, particularly beyond one year, remains to be evaluated.

Acknowledging these limitations highlights areas for future research and provides context for interpreting the applicability of the findings.



## Chapter 5

### 5. Conclusion and recommendations

#### 5.1 Conclusions

This research has comprehensively examined the dry shrinkage behaviour and mechanical performance of alkali-activated slag (AAS) systems, with specific attention to the influence of curing conditions, activator type, and gypsum addition. Both mortar and concrete compositions were investigated, providing a holistic understanding of how these variables affect the dimensional stability and strength of AAS materials. The results highlight the potential of optimised mix designs and curing regimes to effectively mitigating shrinkage and enhancing performance in sustainable construction applications.

##### 5.1.1. Activator Type

The type of alkaline activator exerts a significant influence on the dry shrinkage, strength, and elastic modulus of AAS mortars. Mortars activated with sodium silicate consistently outperformed those activated with sodium carbonate across all mechanical properties due to the formation of a denser and more cohesive microstructure. Sodium silicate promotes the rapid development of well-polymerized calcium–aluminosilicate hydrate (C–A–S–H) gels, which reduce porosity, limit moisture loss, and suppress microcracking, thereby minimizing dry shrinkage and increasing both strength and stiffness.

In contrast, the relatively low alkalinity of the sodium carbonate activator limits the dissolution of slag components, reducing the formation of hydration products such as calcium (alumino) silicate hydrate (C-(A)-S-H) gel. As a result, the microstructure remains more porous, with fewer solid products to fill the voids. This porous structure, coupled with a higher susceptibility to microcracking, leads to a lower elastic modulus and reduced strength compared to mortars activated with stronger alkaline solutions, such as sodium silicate.

These findings highlight that the choice of alkaline activator is critical for reducing dry shrinkage and increasing the mechanical properties of AAS, with sodium silicate proving superior under the curing conditions investigated.

##### 5.1.2. Curing Conditions

The results clearly demonstrate that early-age curing conditions have a significant influence on the dry shrinkage, compressive strength, flexural strength, and elastic modulus of AAS mortars. Fog curing, particularly during the first seven days, substantially reduces dry shrinkage by maintaining high relative humidity, which limits moisture loss and suppresses the development of shrinkage-induced microcracks. This reduction in microcracking, combined with lower porosity resulting from reduced moisture evaporation during hydration, contributes to higher compressive and flexural strengths, as well as increased elastic modulus, compared to samples cured continuously under ambient conditions.

While ambient curing leads to a higher shrinkage and microcracking, resulting in lower mechanical properties, the application of sealed curing after fog treatment further minimizes external moisture loss, highlighting the combined role of internal and external moisture control in achieving dimensional stability and durability. Overall, these findings underscore the critical importance of optimising early-age curing regimes to improve the long-term mechanical properties and structural integrity of AAS.

### 5.1.3. Admixtures

The incorporation of gypsum as an admixture in sodium silicate-activated slag mortars significantly influences dry shrinkage and mechanical properties. The addition of 6% gypsum effectively reduces dry shrinkage by promoting the formation of expansive secondary hydration products, such as ettringite (AFt) and monosulfate (AFm), which fill capillary pores, refine the microstructure. Meanwhile, the formation of ettringite, which has a significantly larger molar volume than its reactants, causes expansion of the samples.

While the incorporation of gypsum slightly delays early-age compressive and flexural strength due to slower slag dissolution and initial precipitation reactions, it enhances long-term strength through ongoing microstructural densification. Flexural strength benefits from the reduced shrinkage and refined pore structure, resulting in improved tensile resistance and crack control over time. In contrast, adding gypsum exhibits minimal impact on the elastic modulus, indicating that its expansive hydration products contribute little to the stiffness of the primary C–A–S–H network. Overall, these findings demonstrate that gypsum serves a dual role in alkali-activated slag mortars—mitigating shrinkage and enhancing long-term strength—while having a limited effect on elastic stiffness.

### 5.1.4. Mortar vs. Concrete Behaviour

AAS Concrete consistently exhibited lower dry shrinkage and higher compressive strength and elastic modulus compared to mortar, primarily due to the presence of coarse aggregates, which provide internal restraint, restricts the deformation of the matrix, reduces the volume of the paste, and redistribute stresses. In contrast, mortar, lacking coarse aggregates, demonstrated higher shrinkage and lower compressive stiffness but generally achieved higher flexural strength owing to its more uniform matrix that allows better stress distribution under bending. Although the addition of gypsum still contributes to the production of expansive hydration products and refinement of the pore structure, the relative effect of gypsum reduces in aggregate-rich systems due to their lower shrinkage potential.

The concrete with sodium silicate activation has about 30-40% lesser dry shrinkage as compared to mortar in all curing regimes and gypsum conditions. The behaviour mainly relies on the higher coarse aggregate content in its concrete, which restricts the deformation of the matrix, reduces the volume of the paste, and improves the distribution of internal forces. Although the addition of gypsum still contributes to the production of expansive hydration products and refinement of the pore structure, the relative effect of gypsum reduces in aggregate-rich systems due to their lower shrinkage potential.

### 5.1.5. AAS vs. OPC

Overall, the results clearly demonstrate that AAS systems exhibit fundamentally different mechanical and deformation behaviours compared to ordinary OPC. AAS mortars and concretes develop higher early-age compressive strength than OPC, particularly when activated with sodium sulphate or solid activators, which promote rapid formation of a dense C–(A)–S–H gel. However, despite their strength advantages, AAS binders show substantially higher autogenous and dry shrinkage (up to 4.4 times greater in mortar and 2.4 times greater in concrete) primarily due to their finer mesopore structure and the associated increase in capillary tension. This elevated shrinkage leads to microcracking, which negatively affects long-term elastic modulus and flexural strength, in contrast to OPC, which exhibits steady increases in stiffness and tensile capacity due to continuous hydration.

The sensitivity of AAS to curing conditions is considerably higher, with prolonged moist curing significantly reducing both shrinkage and stiffness loss, whereas OPC remains less affected

by the curing regime. Furthermore, the presence of aggregates mitigates shrinkage in AAS concrete compared with AAS mortar, but OPC still performs better in terms of dimensional stability. Collectively, these findings underscore that while AAS offers promising strength characteristics and potential sustainability benefits, its shrinkage-related behaviour remains the primary challenge in comparison to conventional OPC systems.

#### 5.1.6. Correlations and Comparison with Model Predictions

In AAS mortars, correlations reveal that increasing dry shrinkage corresponds to reductions in both elastic modulus and flexural strength, while compressive strength may still increase under ambient curing. In contrast, Portland cement mortars (CEM I and CEM III) show simultaneous increases in compressive strength, elastic modulus, and flexural strength due to ongoing hydration and microstructural densification. Early-age fog curing in AAS mitigates shrinkage and microcracking, maintaining higher stiffness and flexural strength, with long-term stabilisation occurring as hydration densifies the microstructure.

Comparisons with standard predictive models (ACI 209, CEB-FIP, B3, GL-2000) indicate that OPC-based models overestimate AAS elastic modulus, though ACI 209 reasonably predicts long-term shrinkage trends. These results highlight the importance of curing and binder selection in controlling long-term mechanical performance in AAS systems.

#### 5.1.7. Suggestion to improve long-term mechanical properties

Based on the experimental findings of this study, several targeted and practical strategies can be recommended to improve the long-term strength and stiffness of AAS mortars and concrete. The recommendations emphasise actionable curing durations, activator options, and admixture combinations suitable for laboratory and field application.

##### 1) Extended Fog Curing (Recommended Duration: 60–90 days)

Optimised early-age curing is the most effective strategy for mitigating shrinkage and improving long-term mechanical properties. Maintaining a fog-cured environment during the first 60–90 days significantly reduces dry shrinkage and suppresses early microcracking, leading to a denser and more stable microstructure. Although a temporary reduction in elastic modulus and flexural strength occurs upon transition from fog to ambient curing, both properties stabilise between 60 and 90 days and remain substantially higher than in continuously ambient-cured conditions. For field application, a minimum fog-curing duration of 28 days is recommended, with extended curing to 60–90 days in structural elements where long-term stiffness and tensile performance are critical.

Extended moist curing periods (60–90 days) can be realistically applied in several practical contexts, particularly where controlled curing environments are already feasible or where structural demands justify prolonged moisture retention. Examples include precast elements, which can be kept in fog-curing chambers or humidity-controlled curing rooms; bridge components such as girders, decks, and piers, where temporary curing enclosures or automated misting systems can be installed; and large pours in hot or arid climates, where long-term water-retaining systems (ponding, soaker hoses, insulated curing blankets, or curing tents) are commonly used to prevent thermal cracking and excessive drying.

##### 2) Optimised Activator Selection

Mechanical properties can be improved by reducing porosity and mitigating shrinkage-induced microcracking through appropriate activator design. Solid Sodium silicate (one-part alkali solution) offers the best performance among the activators studied; however, blended activators (e.g., sodium silicate + sodium sulphate, or sodium silicate + minor silicate

additions) may provide a balanced combination of reduced shrinkage, improved workability, and enhanced long-term stiffness.

### 3) Admixture Combinations to Enhance Densification and Shrinkage Control

Improving the long-term strength and elastic modulus requires simultaneously densifying the matrix and reducing shrinkage. This can be achieved through a combined admixture strategy:

- Silica fume or nano-silica (2–8%) to enhance packing density and promote additional gel formation.
- Fine limestone powder (5–15%) to improve particle packing and reduce capillary pore volume.

Using these admixtures together provides a synergistic improvement, offering both pore structure refinement and microcrack suppression.

### 4) Incorporation of Steel Fibres for Crack Control

Steel fibres serve as effective crack-bridging agents, limiting the propagation of shrinkage-induced microcracks and improving tensile and flexural performance. A dosage of 0.5–1.0% by volume is recommended to significantly enhance strain capacity, flexural strength, and post-cracking behaviour. Fibre reinforcement is particularly beneficial for AAS systems exposed to drying conditions or where long-term stiffness is critical.

## 5.2. Recommendations

The following topics are proposed for future research on shrinkage and mechanical properties of AAS systems:

- This study evaluated AAS activated with sodium silicate and sodium carbonate; therefore, expanding the investigation to alternative activator systems could yield deeper insights into their effects on long-term behaviour and durability.
- Only gypsum, SRA, and AEA were assessed as admixtures in the present work. Future studies should examine additional shrinkage-mitigation strategies, including nanoparticles, internal curing agents such as superabsorbent polymers (SAPs), and lightweight aggregates (e.g., pumice or expanded clay). The inclusion of fibres (polypropylene, steel, or basalt) is also recommended, as they can enhance tensile capacity and limit cracking induced by shrinkage stresses.
- While shrinkage was the primary focus of this research, the contribution of creep to long-term deformation and mechanical performance remains insufficiently understood. Further studies should therefore characterise creep behaviour in AAS and its interaction with shrinkage.

All experiments in this thesis were conducted at a constant curing temperature of 20 °C. Future research should consider the influence of temperature-dependent deformation and cracking, particularly under restrained or (semi-)adiabatic conditions, which are relevant for massive concrete elements prone to thermal stresses.

## References

- [1] F. T. Short and H. A. Neckles, "The effects of global climate change on seagrasses," [Online]. Available: <https://www.sciencedirect.com/science/article/pii/S030437709800117X> . [Accessed 1 April 1999].
- [2] R. M. Andrew, "Global CO<sub>2</sub> emissions from cement production, 1928–2017," 10 December 2018. [Online]. Available: <https://essd.copernicus.org/articles/10/2213/2018/>.
- [3] J. Rogelj, M. den Elzen and N. Höhne , "Paris Agreement climate proposals need a boost to keep warming well below 2 °C," [Online]. Available: <https://pubmed.ncbi.nlm.nih.gov/27357792/>.
- [4] A. Wardhono, C. Gunasekara, D. W. Law and S. Setunge, "Comparison of long term performance between alkali activated slag and fly ash geopolymer concretes," in *Construction and Building Materials*, Indonesia, University of Surabaya, 2017, pp. 272-279.
- [5] IPCC's, "Climate Change 2014 Synthesis Report Summary for Policymakers," 2014. [Online]. Available: [https://www.ipcc.ch/site/assets/uploads/2018/02/AR5\\_SYR\\_FINAL\\_SPM.pdf](https://www.ipcc.ch/site/assets/uploads/2018/02/AR5_SYR_FINAL_SPM.pdf) .
- [6] C. Shi , A. Fernández Jiménez and A. Palomo, "New cements for the 21st century: The pursuit of an alternative to Portland cement," in *Cement and Concrete Research*, Madrid, ScienceDirect, 2011, pp. 750-763.
- [7] J. L. Provis and S. A. Bernal, "Geopolymers and Related Alkali-Activated Materials," [Online]. Available: <https://www.annualreviews.org/content/journals/10.1146/annurev-matsci-070813-113515>.
- [8] M. Fawer , M. Concannon and W. Rieb, "Life Cycle Inventories for the Production of Sodium Silicates," 1999. [Online]. Available: chrome-extension://efaidnbmnnnibpcajpcglclefindmkaj/[https://doc.rero.ch/record/321980/files/s/11367\\_2008\\_Article\\_BF02979498.pdf](https://doc.rero.ch/record/321980/files/s/11367_2008_Article_BF02979498.pdf).
- [9] C. Shi, D. Roy and P. Krivenko, *Alkali-Activated Cements and Concretes*, CRC press, 2003.
- [10] O. Petropavlovsky, "Slag alkaline binding systems and concretes based on steelmaking," 2021. [Online]. Available: chrome-extension://efaidnbmnnnibpcajpcglclefindmkaj/[https://research.tudelft.nl/files/88165772/Phd\\_thesis\\_of\\_zhenming\\_final.pdf](https://research.tudelft.nl/files/88165772/Phd_thesis_of_zhenming_final.pdf).
- [11] M. Pavlin , K. KÖnig, J. König and U. Javornik, "Sustainable Alkali-Activated Slag Binders Based on Alternative Activators Sourced From Mineral Wool and Glass Waste," 2014. [Online]. Available:

<https://www.frontiersin.org/journals/materials/articles/10.3389/fmats.2022.902139/full>.

- [12] M. Nedeljković, Z. Li and G. Ye, "Setting, Strength, and Autogenous Shrinkage of Alkali-Activated Fly Ash and Slag Pastes: Effect of Slag Content," 29 October 2018. [Online]. Available: <https://www.mdpi.com/1996-1944/11/11/2121>.
- [13] M. Nedeljković, Y. Zuo, K. Arbi and G. Ye, "Carbonation Resistance of Alkali-Activated Slag Under Natural and Accelerated Conditions," in *Journal of Sustainable Metallurgy*, Delft, TU Delft, 2018, pp. 33-49.
- [14] S. A. Bernal and J. L. Provis, "Durability of Alkali-Activated Materials: Progress and Perspectives," in *Journal, Ceramics*, 2014.
- [15] D. L.Y. Kong and J. G. Sanjayan, "Effect of elevated temperatures on geopolymer paste, mortar and concrete," in *Cement and Concrete Research*, Australia, ScienceDirect, 2010, pp. 334-339.
- [16] H. Reinhardt, "2 - Factors affecting the tensile properties of concrete," in *Understanding the Tensile Properties of Concrete*, ScienceDirect, 2013, pp. 19-51.
- [17] V. Mohan Malhotra, M.-H. Zhang, P. H. Read and J. Ryell, "Long-term mechanical properties and durability characteristics of highstrength/high-performance concrete incorporating supplementary cementing materials under outdoor exposure," January 2000. [Online]. Available: [chrome-extension://efaidnbmnnnibpcajpcglclefindmkaj/https://www.researchgate.net/profile/Min-Hong-Zhang/publication/250613848\\_Long-term\\_mechanical\\_properties\\_and\\_durability\\_characteristics\\_of\\_high-strengthhigh-performance\\_concrete\\_incorporating\\_supplement](chrome-extension://efaidnbmnnnibpcajpcglclefindmkaj/https://www.researchgate.net/profile/Min-Hong-Zhang/publication/250613848_Long-term_mechanical_properties_and_durability_characteristics_of_high-strengthhigh-performance_concrete_incorporating_supplement).
- [18] S. Khatibmasjedi, F. De Caso and A. Nanni, "Redefining Sustainable Concrete," 11 August 2016. [Online]. Available: [chrome-extension://efaidnbmnnnibpcajpcglclefindmkaj/https://www.researchgate.net/profile/Morteza-Khatib/publication/316596996\\_SEACON\\_Redefining\\_Sustainable\\_Concrete/links/59137ded4585152e199a8e4b/SEACON-Redefining-Sustainable-Concrete.pdf](chrome-extension://efaidnbmnnnibpcajpcglclefindmkaj/https://www.researchgate.net/profile/Morteza-Khatib/publication/316596996_SEACON_Redefining_Sustainable_Concrete/links/59137ded4585152e199a8e4b/SEACON-Redefining-Sustainable-Concrete.pdf).
- [19] S.-y. Jia, M.-h. Liu, B. Han and H.-b. Xie, "An Elastic Modulus Developing Model of Fly Ash Concrete under Sustained Load," in *KSCE Journal of Civil Engineering*, Beijing, ScienceDirect, 2018, pp. 2417-2424.
- [20] J. Ma and F. Dehn, "Shrinkage and creep behavior of an alkali-activated slag concrete," 04 May 2017. [Online]. Available: <https://onlinelibrary.wiley.com/doi/abs/10.1002/suco.201600147>.
- [21] J. Davidovits, "Geopolymer chemistry and sustainable Development. The Poly(sialate) terminology : a very useful and simple model for the promotion and understanding of green-chemistry," 2005. [Online]. Available: <chrome-extension://efaidnbmnnnibpcajpcglclefindmkaj/https://www.researchgate.net/profile/Joseph->



Davidovits/publication/284514069\_Geopolymer\_chemistry\_and\_sustainable\_development/links/5bfed378299bf1a3c1555b37/Geopolymer-chemistry-and-sustainable-developme.

- [22] A. R. Sakulich, E. Anderson, C. Schauer and M. W. Barsoum, “Mechanical and microstructural characterization of an alkali-activated slag/limestone fine aggregate concrete,” in *Construction and Building Materials*, United States, ScienceDirect, 2009, pp. 2951-2957.
- [23] R. Shrestha, D. Baweja, K. Neupane, . D. Chalmers and P. Sleep, “Mechanical Properties of Geopolymer Concrete: Applicability of Relationships Defined by AS 3600,” 2013. [Online]. Available: <https://opus.lib.uts.edu.au/handle/10453/32589>.
- [24] B. V. Rangan, “Fly Ash-Based Geopolymer Concrete,” in *Geopolymer Cement and*, 2010, pp. 68-106.
- [25] A. Fernández-Jiménez, J. Palomob and F. Puertasa, “Alkali-activated slag mortars Mechanical strength behaviour,” in *Cement and Concrete Research*, Madrid, Cement and concrete research, 1999, p. 1313–1321.
- [26] N. Awasthy , E. Schlangen , D. Hordijk , B. Savija and M. Lukovi ´ c, “The role of eigenstresses on apparent strength and stiffness of normal, high strength, and ultra-high performance fibre reinforced concrete,” in *Developments in the Built Environment*, Delft, ELSEVIER, 2023.
- [27] S. Prinsse, D. A. Hordijk, G. Ye, P. Lagendijk and M. Lukovic, “Time-dependent material properties and reinforced beams behavior of two alkali-activated types of concrete,” in *Structural Concrete fib*, Delft, 2020, pp. 642-658.
- [28] E. O. L. Lantsoght, C. van der Veen, A. de Boer and H. van der Ham, “Long-term material and structural behavior of high-strength concrete cantilever bridge: Results of 20 years monitoring,” in *Structural concrete*, Onlinelibrary, 2018, pp. 1079-1091.
- [29] F. Collins and J. Sanjayan, “Microcracking and strength development of alkali activated slag concrete,” in *Cement and Concrete Composites*, Australia, 2001, pp. 345-352.
- [30] J. Asselanis, P.-C. Aitcin and P. Mehta, “Effect of Curing Conditions on the Compressive Strength and Elastic Modulus of Very High-Strength Concrete,” in *Cement Concrete and Aggregates*, ASTM, 1989, pp. 80-83.
- [31] D. Kocab, B. Kucharczykova, P. Misak, P. Zitt and M. Kralikova, “Development of the Elastic Modulus of Concrete under Different Curing Conditions,” in *Procedia Engineering*, Czech Republic, ScienceDirect, 2017, p. 96 – 101.
- [32] A. H. Hameed, “THE EFFECT OF CURING CONDITION ON COMPRESSIVE STRENGTH IN HIGH STRENGTH CONCRETE,” in *Diyala Journal of Engineering Sciences*, Diyala, Diyala University, 2009, pp. 35-48.
- [33] A. Logan, W. Choi, A. Mirmiran, S. Rizkalla and P. Zia, “Short-Term Mechanical Properties of High-Strength Concrete,” in *ACI Mater*, 2009, p. 413–418. .



- [34] J. L. Provis, "Alkali-activated materials," in *Cement and Concrete Research*, University of Sheffield, Sheffield S1 3JD, UK, 2018, pp. 40-48.
- [35] Y. Mugahed Amran, . R. Alyousef, H. Alabduljabbar and M. El-Zeadani , "Clean production and properties of geopolymer concrete; A review," in *Journal of Cleaner Production*, 2020.
- [36] M. Amran, R. Fediuk, G. Murali, N. Vatin, M. Karelina, T. Ozbakkaloglu, R. S. Krishna, A. K. Sahoo, . S. Kumar Das and J. Mishra, "https://www.mdpi.com/2073-4352/11/2/168," 8 February 2021. [Online].
- [37] A. Cherki El Idrissi, M. Paris, E. Rozière, D. Deneele, S. Darson and A. Loukili, "Alkali-activated grouts with incorporated fly ash: From NMR analysis to mechanical properties," in *Materials Today Communications*, France, 2018, pp. 225-232.
- [38] J. L. Provis and S. A. Bernal, "Geopolymers and Related Alkali-Activated Materials," July 2014. [Online]. Available: <https://www.annualreviews.org/doi/10.1146/annurev-matsci-070813-113515>.
- [39] A. M. Rashad, "A comprehensive overview about the influence of different admixtures and additives on the properties of alkali-activated fly ash," in *Materials & Design*, Building Materials Research and Quality Control Institute, Housing & Building National Research Center, HBRC, Cairo, Egypt, 2014, pp. 1005-1025.
- [40] "Slag valorisation in construction material," [Online]. Available: <https://slideplayer.com/slide/5269327/> . [Accessed 15 April 2015].
- [41] J. Liu , L. Hu, L. Tang, E. Qingnan Zhang and J. Ren, "Shrinkage behaviour, early hydration and hardened properties of sodium silicate activated slag incorporated with gypsum and cement," in *Construction and Building Materials*, ELsevier, 2020.
- [42] M. Al-Jabari, "Introduction to concrete chemistry," in *Integral Waterproofing of Concrete Structures*, Hebron, ScienceDirect, 2022, pp. 1-36.
- [43] M. Li, Y. Lu, Y. Liu , J. Chu, T. Zhang and W. Wang, "Influence of the Steel Slag Particle Size on the Mechanical Properties and Microstructure of Concrete," 2 March 2024. [Online]. Available: <https://www.mdpi.com/2071-1050/16/5/2083>.
- [44] P. Awoyera and A. Adesina, "A critical review on application of alkali activated slag as a sustainable composite binder," in *Case Studies in Construction Materials*, Canada, ScienceDirect, 2019.
- [45] J. L. Provis and S. A. Bernal, "Geopolymers and Related Alkali-Activated Materials," 03 February 2014. [Online]. Available: <https://www.annualreviews.org/content/journals/10.1146/annurev-matsci-070813-113515>.
- [46] C. Winterman, "Understanding the Mechanism of Drying Shrinkage in Alkali-Activated Binders," 29 Januar 2024. [Online].

- [47] F. Pacheco-Torgal, "1 - Introduction to Handbook of Alkali-," in *Handbook of Alkali-activated Cements, Mortars and Concrete activated Cements, Mortars and Concretes*, Guimarães, University of Minho, Guimarães, Portugal, 2015, pp. 1-16.
- [48] S. Chen, S. Ruan, Q. Zeng, Y. Liu, M. Zhang and Y. Tian , "Pore structure of geopolymer materials and its correlations to engineering properties: A review," in *Construction and Building Materials*, ScienceDirect, 2022.
- [49] Y. Ma, "Microstructure and Engineering Properties of Alkali Activated Fly Ash," Wuhan University, 2013.
- [50] P. Duxson , J. L. Provis, G. C. Lukey , S. W. Mallicoat, W. M. Kriven and J. S.J. van Deventer , "Understanding the relationship between geopolymer composition, microstructure and mechanical properties," in *Colloids and Surfaces*, ELSEVIER, 2005, p. 47–58.
- [51] R. D. Kalina, S. Al-Shmaisani, R. Douglas and M. C. G. Juenger, "False Positives in ASTM C618 Specifications for Natural Pozzolans," 2019. [Online]. Available: chrome-extension://efaidnbmnnnibpcajpcgclefindmkaj/https://forensixconsulting.com/wp-content/uploads/2020/11/Kalina-et-al-2019-1.pdf.
- [52] P. Duxson and J. L. Provis, "Designing Precursors for Geopolymer Cements," 15 December 2008. [Online]. Available: <https://ceramics.onlinelibrary.wiley.com/doi/10.1111/j.1551-2916.2008.02787.x>.
- [53] T. Hemalatha and A. Ramaswamy, "A review on fly ash characteristics e Towards promoting high volume utilization in developing sustainable concrete," in *Journal of Cleaner Production*, India, ELSEVIER, 2017, pp. 546-559.
- [54] C. Turan, A. A. Javadi and R. Vinai, "Effects of Class C and Class F Fly Ash on Mechanical and Microstructural Behavior of Clay Soil—A Comparative Study," 1 March 2022. [Online]. Available: <https://www.mdpi.com/1996-1944/15/5/1845>.
- [55] A. Wardhono, C. Gunasekara, D. W. Law and S. Setunge, "Comparison of long term performance between alkali activated slag and fly ash geopolymer concretes," in *Construction and Building Materials*, ScienceDirect, 2017, pp. 272-279.
- [56] N. Lee and H. Lee, "Setting and mechanical properties of alkali-activated fly ash/slag concrete manufactured at room temperature," in *Construction and Building Materials*, South Korea, Elsevier, 2013, pp. 1201-1209.
- [57] S. A. Bernal, J. L. Provis, R. J. Myers, R. San Nicolas and J. S. J. van Deventer, "Role of carbonates in the chemical evolution of sodium carbonate-activated slag binders," in *Materials and Structures*, Deventer, 2015, p. 517–529.
- [58] S. Dong Wang, X. Cheng Pu and K. L. Scrivener, "Alkali-activated slag cement and concrete: a review of properties and problems," in *Advances in Cement Research*, ICE Virtual Library, 2015, pp. 93-102.

- [59] John L. Provis, "Alkali-activated materials," in *Cement and Concrete Research*, UK, ScienceDirect, 2017, pp. 40-48.
- [60] M. Juenger, F. Winnefeld, J. Provis and J. Ideker, "Advances in alternative cementitious binders," in *Cement and Concrete Research*, Texas, ScienceDirect, 2011, pp. 1232-1243.
- [61] V. Živica, "Effects of type and dosage of alkaline activator and temperature on the properties of alkali-activated slag mixtures," in *Construction and Building Materials* 21, Bratislava, ScienceDirect, 2007, p. 1463-1469.
- [62] F. Puertas, S. Martı́nez-Ramı́rez, S. Alonso and T. Vázquez, "Alkali-activated fly ash/slag cements: Strength behaviour and hydration products," in *Cement and Concrete Research*, Madrid, ScienceDirect, 2000, pp. 1625-1632.
- [63] J. L. Provis, R. San Nicolas and J. van Deventer, "Role of carbonates in the chemical evolution of sodium carbonate-activated slag binders," 25 September 2014. [Online]. Available: [https://www.researchgate.net/publication/265168495\\_Role\\_of\\_carbonates\\_in\\_the\\_chemical\\_evolution\\_of\\_sodium\\_carbonate-activated\\_slag\\_binders](https://www.researchgate.net/publication/265168495_Role_of_carbonates_in_the_chemical_evolution_of_sodium_carbonate-activated_slag_binders).
- [64] A. J. Moseson, D. E. Moseson and M. W. Barsoum, "High volume limestone alkali-activated cement developed by design of experiment," in *Cement & Concrete Composites*, Philadelphia, ScienceDirect, 2011, pp. 328-336.
- [65] Y. Bai, N. Collier, N. Milestone and C. Yang, "The potential for using slags activated with near neutral salts as immobilisation matrices for nuclear wastes containing reactive metals," in *Journal of Nuclear Materials*, Chongqing, ScienceDirect, 2011, pp. 183-192.
- [66] T. Bakharev, J. Gnananandan Sanjayan and Y.-B. Cheng, "Cement and Concrete Research 29," in *Alkali activation of Australian slag cements*, Victoria, scienceDirect, 1999, p. 113-120.
- [67] M. Dong, M. Elchalakani and A. Karrech, "Development of high strength one-part geopolymer mortar using sodium metasilicate," in *Construction and Building Materials*, Australia, ScienceDirect, 2020.
- [68] K.-H. Yang and J.-K. Song, "Workability Loss and Compressive Strength Development of Cementless Mortars Activated by Combination of Sodium Silicate and Sodium Hydroxide," 2009. [Online]. Available: [https://www.researchgate.net/publication/270767047\\_Workability\\_Loss\\_and\\_Compressive\\_Strength\\_Development\\_of\\_Cementless\\_Mortars\\_Activated\\_by\\_Combination\\_of\\_Sodium\\_Silicate\\_and\\_Sodium\\_Hydroxide](https://www.researchgate.net/publication/270767047_Workability_Loss_and_Compressive_Strength_Development_of_Cementless_Mortars_Activated_by_Combination_of_Sodium_Silicate_and_Sodium_Hydroxide).
- [69] P. J. Schilling, A. Roy, H. Eaton, P. G. Malone and N. W. Brabston, "Microstructure, strength, and reaction products of ground granulated blast-furnace slag activated by highly concentrated NaOH solution," 03 March 2013. [Online]. Available: <https://www.cambridge.org/core/journals/journal-of-materials-research/article/abs/microstructure-strength-and-reaction-products-of-ground->

granulated-blastfurnace-slag-activated-by-highly-concentrated-naoh-solution/90F489E0F4E60BA2E7D14476C7690622?utm\_sour.

- [70] K. Gong and C. E. White, "Time-dependent phase quantification and local structure analysis of hydroxide-activated slag via X-ray total scattering and molecular modeling," 03 Aug 2021. [Online]. Available: [https://arxiv.org/abs/2108.01535?utm\\_source=chatgpt.com](https://arxiv.org/abs/2108.01535?utm_source=chatgpt.com).
- [71] G. Liu, M. Florea and H. Brouwers, "The role of recycled waste glass incorporation on the carbonation behaviour of sodium carbonate activated slag mortar," in *Journal of Cleaner Production*, Eindhoven, ELSEVIER, 2021.
- [72] C. Sun, J. Sun and D. Wang, "Effect of tartaric acid on the early hydration of NaOH-activated slag paste," in *Journal of Thermal Analysis and Calorimetry*, Budapest, Springer Nature Link, 2021, p. 41–50.
- [73] "Alkali-activated slag mortars Mechanical strength behaviour," in *Cement and Concrete Research*, Madrid, ScienceDirect, 1999, p. 1313–1321.
- [74] A. Noorliyana Hashim, H. Kamarudin, N. Begum and J. Jaya Ekaputri, "Effect of Sodium Hydroxide (NaOH) Concentration on Compressive Strength of Alkali-Activated Slag (AAS) Mortars," April 2015. [Online]. Available: [https://www.researchgate.net/publication/272793301\\_Effect\\_of\\_Sodium\\_Hydroxide\\_NaOH\\_Concentration\\_on\\_Compressive\\_Strength\\_of\\_Alkali-Activated\\_Slag\\_AAS\\_Mortars](https://www.researchgate.net/publication/272793301_Effect_of_Sodium_Hydroxide_NaOH_Concentration_on_Compressive_Strength_of_Alkali-Activated_Slag_AAS_Mortars).
- [75] G. Venkatappa Rao, C. Hanumantha Rao and P. Saha, "INTERNATIONAL JOURNAL OF EARTH SCIENCES AND ENGINEERING," 2011. [Online]. Available: [chrome-extension://efaidnbmnnnibpcajpcglclefindmkaj/https://www.researchgate.net/profile/Hanumantharao-Chappidi-2/publication/277897292\\_Capacity\\_Constraints\\_on\\_Progressing\\_of\\_National\\_Highway\\_Projects\\_in\\_India/links/57a32a0208aef3c1a7b3bc9d/Capacity-Const](chrome-extension://efaidnbmnnnibpcajpcglclefindmkaj/https://www.researchgate.net/profile/Hanumantharao-Chappidi-2/publication/277897292_Capacity_Constraints_on_Progressing_of_National_Highway_Projects_in_India/links/57a32a0208aef3c1a7b3bc9d/Capacity-Const).
- [76] S. Aaron Richard, "Characterization of environmentally-friendly alkali activated slag cements and ancient building materials," Drexel University, Drexel, 2009.
- [77] F. Pacheco-Torgal, J. Castro-Gomes and S. Jalali, "Alkali-activated binders: A review Part 1. Historical background, terminology, reaction mechanisms and hydration products," in *Construction and Building Materials*, Elsevier, 2008, p. 1305–1314.
- [78] M. Sirotti, B. Delsaute and S. Staquet, "New Experimental Evidence for Drying Shrinkage of Alkali-Activated Slag with Sodium Hydroxide," 2023. [Online]. Available: <https://www.mdpi.com/1996-1944/16/16/5659>.
- [79] A. Fernández-Jiménez, A. Palomo and M. Criado, "Alkali activated fly ash binders. A comparative study between sodium and potassium activators," in *Materiales de Construcción*, Revistas, 2006, pp. 51–65.
- [80] A. V. McCormick and A. T. Bell, "The Solution Chemistry of Zeolite Precursors," in *Catalysis Reviews—Science and Engineering*, 1989, pp. 97–127.

- [81] “Understanding the relationship between geopolymer composition, microstructure and mechanical properties,” in *Colloids and Surfaces* , ELSEVIER, 2005, p. 47–58.
- [82] J. L. Provis , G. C. Lukey and J. S. J. van Deven, “Do Geopolymers Actually Contain Nanocrystalline Zeolites? A Reexamination of Existing Results,” in *Chemistry of Materials*, 2005, pp. 3075-3085.
- [83] M. Palacios and F. Puertas, “Effect of shrinkage-reducing admixtures on the properties of alkali-activated slag mortars and pastes,” in *Cement and Concrete Research*, Madrid, ScienceDirect, 207, p. 691–702.
- [84] M. Criado , A. Fernández-Jiménez and A. Palomo, “Alkali activation of fly ash. Part III: Effect of curing conditions on reaction and its graphical description,” in *Fuel*, Madrid, ScienceDirect, 2010, p. 3185–3192.
- [85] C. Liu , H. Wu a, Z. Li , H. Shi and G. Ye, “Effect of curing condition on mechanical properties and durability of alkali-activated slag mortar,” in *Construction and Building Materials*, Delft, ScienceDirect, 2024.
- [86] D. Hardjito, S. E. Wallah, D. M. J. Sumajouw and B. Vijaya Rangan, “On the Development of Fly Ash-Based Geopolymer Concrete,” 2004. [Online]. Available: chrome-extension://efaidnbmnribpcajpcglclefindmkaj/https://www.researchgate.net/profile/Djwantoro-Hardjito/publication/303836414\_ACI\_Materials/links/5c7c43bd92851c6950520ea1/ACI-Materials.pdf.
- [87] F. ŠKVÁRA, T. JÍLEK and L. KOPECKÝ, “GEOPOLYMER MATERIALS BASED ON FLY ASH,” 2005. [Online]. Available: chrome-extension://efaidnbmnribpcajpcglclefindmkaj/http://www.geopolymery.eu/aitom/upload/documents/publikace/2005/ceramics2005\_03\_195.pdf.
- [88] T. Bakharev, . J. Sanjayan and . Y.-B. Cheng, “Effect of elevated temperature curing on properties of alkali-activated slag concrete,” in *Cement and Concrete Research*, Australia, Monash University, 1999, pp. 1619-1625.
- [89] A. Palomo, . M. Grutzeck and M. Blanco, “Alkali-activated fly ashes A cement for the future,” in *Cement and Concrete Research*, USA, ScienceDirect, 1999, pp. 1323-1329.
- [90] D. Hardjito, . S. E. Wallah, . D. M. J. Sumajouw and B. Rangan, “On the Development of Fly Ash-Based Geopolymer Concrete,” 2004. [Online]. Available: https://www.researchgate.net/profile/Djwantoro-Hardjito/publication/303836414\_ACI\_Materials/links/5c7c43bd92851c6950520ea1/ACI-Materials.pdf.
- [91] B. Joseph and G. Mathew, “Influence of aggregate content on the behavior of fly ash based geopolymer concrete,” in *Scientia Iranica*, India, Sharif University of Technology, 2012, pp. 1188-1194.

- [92] P. Nath and P. Kumar Sarker, "Effect of GGBFS on setting, workability and early strength properties of fly ash geopolymer concrete cured in ambient condition," in *Construction and Building Materials*, Australia, Elsevier, 2014, pp. 163-171.
- [93] C. Fredericci , E. Zanotto and E. Ziemath, "Crystallization mechanism and properties of a blast furnace slag glass," in *Non-Crystalline Solids*, SciencDirect, 2000, pp. 64-75.
- [94] M. Nodehi, T. Ozbakkaloglu , A. Gholampour, T. Mohammed and X. Shi, "The effect of curing regimes on physico-mechanical, microstructural and," Elsevier, 2022.
- [95] P. Kumar Mehta and P. J. M. Monteiro, "Concrete: Microstructure, Properties, and Materials, 4th Edition," 2014. [Online]. Available: <https://www.accessengineeringlibrary.com/content/book/9780071797870>.
- [96] R. Thomas, D. Lezama and S. Peethamparan, "On drying shrinkage in alkali-activated concrete: dimensional stability by aging or heat-curing," in *Cement and Concrete Research*, USA, ScienceDirect, 2016, pp. 13-23.
- [97] K. Kovler and S. Zhutovsky, "Overview and future trends of shrinkage research," 5 July 2006. [Online]. Available: <https://link.springer.com/article/10.1617/s11527-006-9114-z>.
- [98] D. Huang, P. Chen , P. Heu, Y. Yiwei, Q. Yuan and M. Su, "A review and comparison study on drying shrinkage prediction between alkali-activated fly ash/slag and ordinary Portland cement," in *Construction and Building Materials*, China, ScienceDirect, 2021.
- [99] H. Ye, C. Cartwright, F. Rajabipour and A. Radlinska , "Understanding the drying shrinkage performance of alkali-activated slag mortars," in *Cement and Concrete Composites*, Pennsylvania State, ScienceDirect, 2017, pp. 13-24.
- [100] Y. Ma and G. Ye, "The shrinkage of alkali activated fly ash," in *Cement and Concrete Research*, Delft, ScienceDirect, 2015, pp. 75-82.
- [101] C. Winterman, G. Ye, M. Luković, M. Gupta and F. Aghabeyk, "Understanding the Mechanism of Drying Shrinkage in Alkali-Activated Binders," TU Delft, Delft, 2024.
- [102] P. Lura, F. Goodwin, D. Bentz, D. Hooton, K. Kovler and J. Weiss, "Standard Test Method for Autogenous Strain of Cement Paste and Mortar," [Online]. Available: <https://orbit.dtu.dk/en/publications/standard-test-method-for-autogenous-strain-of-cement-paste-and-mo>.
- [103] L. J. Struble and Q. Jiang, "Effects of Air Entrainment on Rheology," 2004. [Online]. Available: [http://www.qyjohn.net/blog/2004\\_Rheology.pdf](http://www.qyjohn.net/blog/2004_Rheology.pdf).
- [104] L. Coppola, D. Coffetti, . E. Crotti , S. Candamano, . F. Crea, G. Gazzaniga and T. Pastore, "The combined use of admixtures for shrinkage reduction in one-part alkali activated slag-based mortars and pastes," in *Construction and Building Materials*, Italy, ScienceDirect, 2020.



- [105] S. Aydın and B. Baradan, "The effect of fiber properties on high performance alkali-activated slag/silica fume mortars," in *Composites: Part B*, 2013, ScienceDirect, p. 63–69.
- [106] T. Bakharev, J. G. Sanjayan and Y.-B. Cheng, "Effect of admixtures on properties of alkali-activated slag concrete," in *Cement and Concrete Research*, Elsevier Science , 2000, p. 1367 ± 1374.
- [107] G. Ye , "Experimental Study and Numerical Simulation of the Development of the Microstructure and Permeability of Cementitious Materials," DUP Science, Delft, 2003.
- [108] F. Lea, "The Chemistry of Cement and Concrete," Chemical Publishing Co., New, 1970.
- [109] H. Taylor, "The Chemistry of cement," Academic Press, London, 1964.
- [110] T. Powers and T. Brownyard, "Journal of the American Concrete Institute," in *Studies of the physical properties of hardened portland cement*, 1947, pp. 669-712.
- [111] S. Diamond, "Cement and Concrete Research," in *A critical comparison of mercury porosimetry and capillary condensation pore size distributions of Portland cement pastes*, 1971, pp. 531-545.
- [112] K. Scrivener, "Material Research Society Symposium," in *The use of backscattered electron microscopy and image analysis to study the porosity of cement paste*, 1988, pp. 129-140..
- [113] L. Zhang and F. Glasser, "Advances in Cement Research," in *Critical examination of drying damage to cement pastes*, 2000, pp. 79-88.
- [114] P. Tennis and H. Jennings, "Cement and concrete research," in *A model for two types of calcium silica hydrate in the microstructure of Portland cement pastes*, 2000, pp. 855-863.
- [115] H. Taylor, "Cement Chemistry," Academic Press, London, 1990.
- [116] I. Odler, "Chemistry of Cement and Concrete," in *Hydration, Setting, and Hardening of Portland Cement*, U.K., 1998, p. 241.
- [117] K. van Breugel, "Simulation of hydration and formation of structure in hardening cement-based materials," Delft University of Technology, Delft, 1991.
- [118] E. 196-3, "Method of testing cement - Part 3: Determination of setting time and soundness," December 2016. [Online]. Available: <https://connect.nen.nl/Search/Detail?collectionId=0&compId=10037&colAdmin=false>.
- [119] J. Stark and K. Bollmann, "Delayed Ettringite Formation in Concrete," in *Zement Kalk Gips*, Germany, Bauhaus-University Weimar, 1976, pp. 435-442.
- [120] C. Pignat, P. Navi and K. Scrivener, "International Congress on the Chemistry of Cement, Durban," in *Simulation of cement paste microstructure during hydration*,



*characterization of the pore space and permeability determination*, South Africa, 2003, pp. 197-205.

- [121] P. Stutzman, "Materials Science of Concrete Special Volume," in *Scanning Electron Microscopy in Concrete Petrography*, Florida, 2001, pp. 59-72.
- [122] T. Powers and T. Brownyard, "Journal of the American Concrete Institute," in *Studies of the physical properties of hardened portland cement paste*, 1946.
- [123] P. Tennis and H. Jennings, "Cement and concrete research," in *A model for two types of calcium silica hydrate in the microstructure of Portland cement pastes*, 2000, pp. 855-863.
- [124] N. Banthia and S. Mindess, "Material Research Society Symposium," in *Permeability measurements on cement paste*, pp. 173-178.
- [125] Y. Wang , S. Nanukuttan , Y. Bai and P. Bashe, "Construction and Building Materials," in *Influence of curing on chloride ingress and strength development in concrete*, 2005, p. 13-19.
- [126] J. Khatib and S. Wild, "Cement and Concrete Research," in *Pore size distribution of metakaolin paste*, ELSEVIER, 1996, pp. 1545-1553.
- [127] D. P. Bentz and K. A. Snyder, "Journal of the American Ceramic Society," in *Three-dimensional computer simulation of Portland cement hydration and microstructure development*, ELSEVIER, 1999, p. 1863-1867.
- [128] O. M. Jensen and P. F. Hansen, "Cement and Concrete Research," in *Autogenous deformation and RH-change in perspective*, ELSEVIER, 2001, p. 1859-1865.
- [129] J. Escalante-Garcia, "Cement and Concrete Research," in *Effects of temperature on the hydration of Portland cement*, ELSEVIER, 2001, p. 695-702.
- [130] M. H. Zhang and O. E. Gjrv, "Cement and Concrete Research,," in *Effect of silica fume on pore structure and chloride diffusivity of low water-cement ratio concrete*, 1991, p. 1006-1014.
- [131] M. Raghav , T. Park, H.-M. Yang, S.-Y. Lee, S. Karthick and H.-S. Lee, "Review of the Effects of Supplementary Cementitious Materials and Chemical Additives on the Physical, Mechanical and Durability Properties of Hydraulic Concrete," 28 November 2021. [Online]. Available: [https://pmc.ncbi.nlm.nih.gov/articles/PMC8672277/?utm\\_source=chatgpt.com](https://pmc.ncbi.nlm.nih.gov/articles/PMC8672277/?utm_source=chatgpt.com).
- [132] J. Escalante-Garcia, "Cement and Concrete Research," in *Nonevaporable water from neat OPC and replacement materials in composite cements hydrated at different temperatures*, ELSEVIER, 2003, pp. 1883-1888.
- [133] B. Zhou, K. Wang, P. C. Taylor and Y. Gu, "Superabsorbent Polymers for Internal Curing Concrete: An Additional Review on Characteristics, Effects, and Applications," 08

November 2024. [Online]. Available: [https://www.mdpi.com/1996-1944/17/22/5462?utm\\_source=chatgpt.com](https://www.mdpi.com/1996-1944/17/22/5462?utm_source=chatgpt.com).

- [134] H. Toutanji, N. Delatte, S. Aggoun, . R. Duval and A. Danson, "Cement and Concrete Research," in *Effect of supplementary cementitious materials on the compressive strength and durability of short-term cured concrete*, ELSEVIER, 2004, pp. 311-319.
- [135] H. Ge, Z. Sun, Z. Lu, H. Yang, T. Zhang and N. He, "Journal of Building Engineering," in *Influence and mechanism analysis of different types of water reducing agents on volume shrinkage of cement mortar*, ELSEVIER, 2024, pp. 108-204.
- [136] M. Raghav, T. Park, H.-M. Yang, S.-Y. Lee, S. Karthick and H.-S. Lee, "Review of the Effects of Supplementary Cementitious Materials and Chemical Additives on the Physical, Mechanical and Durability Properties of Hydraulic Concrete," 28 November 2021. [Online]. Available: [https://pmc.ncbi.nlm.nih.gov/articles/PMC8672277/?utm\\_source=chatgpt.com](https://pmc.ncbi.nlm.nih.gov/articles/PMC8672277/?utm_source=chatgpt.com).
- [137] P. Zhong, M. Wyrzykowski, N. Toropovs, L. Li, J. Liu and P. Lura, "Internal curing with superabsorbent polymers of different chemical structures," in *Cement and Concrete Research*, ELSEVIER, 2019.
- [138] A. M. Neville, Properties of concrete, United Kingdom: British Library Cataloguing in Publication, 2011.
- [139] D. P. Bentz, "Three-dimensional computer simulation of Portland cement hydration and microstructure development," in *Journal of the American Ceramic Society*, ELSEVIER, 1997, pp. 3-21.
- [140] M. C. G. e. a. Juenger, "Supplementary cementitious materials: New sources, characterization, and qualification," in *Cement and Concrete Research*, 2019, pp. 105-115.
- [141] M. D. A. Thomas, Supplementary Cementing Materials in Concrete. CRC Press., 2013.
- [142] H. Toutanji, "Effect of silica fume on concrete strength and microstructur," in *Cement and Concrete*, 2004, pp. 559-567.
- [143] M. e. a. Raghav, "Review of the effects of supplementary cementitious materials on concrete properties," in *Cement and Concrete Composites*, 2021.
- [144] N. K. Lee and H. K. Lee, "Setting and mechanical properties of alkali-activated fly ash/slag concrete," in *Construction and Building Materials*, 2013, pp. 1201-1209.
- [145] J. L. B. V. B. A. D.-D. K. & V. B. Provis, "Alkali Activated Materials: State-of-the-Art Report," in *Durability and Testing Physical Processes*, Springer Netherlands, 2014, pp. 277-307.
- [146] R. J. & P. S. Thomas, "Alkali-activated concrete: Engineering properties and stress-strain behavior," in *Construction and Building Materials*, 2015, pp. 49-56.

- [147] C. V. S. S. R. N. & M. P. S. Kameswara Rao, "Mechanical behaviour of concrete as a composite material," in *Matériaux et Construction*, 1974, pp. 265-271.
- [148] Y. D. J.-G. & S. C.-J. Ding, "Mechanical properties of alkali-activated concrete: A state-of-the-art review," in *Construction and Building Materials*, 2016, pp. 68-79.
- [149] P. P. J. L. L. G. C. M. S. W. K. W. M. & v. D. J. S. J. Duxson, "Understanding the relationship between geopolymer composition, microstructure and mechanical properties," in *Colloids and Surfaces A: Physicochemical and Engineering Aspects*, 2005, pp. 47-58.
- [150] R. Priyadarshi, "Shrinkage behaviour of 3D printing concrete mixture An experimental and numerical study," TU Delft, Delft, 2021.
- [151] F. Wittmann, "Surface tension. shrinkage. and strength of hardened cement paste," 1968. [Online]. Available: [https://www.researchgate.net/publication/226838319\\_Surface\\_tension\\_shrinkage\\_and\\_strength\\_of\\_hardenened\\_cement\\_paste](https://www.researchgate.net/publication/226838319_Surface_tension_shrinkage_and_strength_of_hardenened_cement_paste).
- [152] V. Baroghel-Bouny, M. Mainguy, T. Lassabatere and O. Coussy, "Characterization and identification of equilibrium and transfer moisture properties for ordinary and high-performance cementitious materials," in *Cement and concrete research*, ELSEVIER, 1999, p. 1225-1238.
- [153] J. K. a. R. C. G. M. Moelich, "Plastic shrinkage cracking in 3d printed concrete," in *Composites Part B: Engineering*, 2020.
- [154] T. F. F. D. a. T. G. N. F. Tanue, "Characterisation of early age deformations in cement paste: Case of chemical and autogenous shrinkage," in *Journal of Minerals and Materials Characterization and Engineering*, ELSEVIER, 2020, p. 223-239.
- [155] T. Lu, Z. Li and H. Huang, "Restraining effect of aggregates on autogenous shrinkage in cement," in *Construction and Building Materials*, ELSEVIER, 2021, pp. 123-166.
- [156] D. P. B. a. O. M. Jensen, "Mitigation strategies for autogenous shrinkage cracking," in *Cement and Concrete Composites*, ELSEVIER, 2004, p. 677-685.
- [157] J. K. K. a. C. S. Lee, "Moisture diffusion of concrete considering selfdesiccation at early ages," in *Cement and Concrete Research*, ELSEVIER, 1999, p. 1921-1927.
- [158] Z. S. a. P. W. Z. Jiang, "Internal relative humidity distribution in highperformance cement paste due to moisture diffusion and selfdesiccation," in *Cement and concrete research*, ELSEVIER, 2006, p. 320-325.
- [159] X. Z. a. H. Zhao, "Characterization of moisture diffusion in cured concrete slabs at early ages," in *Advances in Materials Science and Engineering*, ELSEVIER, 2015, p. 1-10.
- [160] H. M. J. R. A. L. A. N. G. W. S. J. S. S. K. L. S. a. J. J. T. J. W. Bullard, "Mechanisms of cement hydration," in *Cement and concrete research*, ELSEVIER, 2011, p. 1208-1223.

- [161] R. L. B. J. H. K. N. B. M. a. J. F. Y. A. Bentur, "Structural properties of calcium silicate pastes: li, effect of curing temperature," in *Journal of the American Ceramic Society*, 1979, pp. 362–366,.
- [162] E. E. Holt, "Early age autogenous shrinkage of concrete," University of Washington, Washington, 2001.
- [163] A. G. a. D. Kosson, "Modeling moisture transport from a portland cementbased material during storage in reactive and inert atmospheres," in *Drying Technology*, ELSEVIER, 2003, p. 775–805.
- [164] A. E. Idiart, "Coupled analysis of degradation processes in concrete specimens at the mesolevel," UNIVERSITAT POLITÈCNICA DE CATALUNYA, 2009.
- [165] F. Wittmann, "Surface tension. shrinkage. and strength of hardened cement paste," in *Matériaux et Constructions*, ELSEVIER, 1968, p. 547–552.
- [166] M. C.G. Juenger , F. Winnefeld, . J. L. Provis and J. H. Ideker, "Advances in alternative cementitious binders," in *Cement and Concrete Research*, ScienceDirect, 2010, pp. 1232-1243.
- [167] S.-D. Wang, X.-C. Pu, K. L. Scrivener and P. L. Pratt, "Alkali-activated slag cement and concrete: a review of properties and problems," in *Advances in Cement Research*, emerald, 1995, pp. 93-102.
- [168] S. Prinsse, D. Hordijk, . D. M. Luković, G. Ye and P. Lagendijk, "ALKALI-ACTIVATED CONCRETE: development of material properties (strength and stiffness) and flexural behaviour of reinforced beams over time., " TU Delft, Delft, 2017.
- [169] B. Singh, I. G., M. Gupta and S. Bhattacharyya, "Geopolymer concrete: A review of some recent developments," in *Construction and Building Materials*, India, ELSEVIER, 2015, pp. 78-90.
- [170] B. CHEN, "Utilization of mswi bottom ash as a mineral resource for low-carbon construction materials Quality-upgrade treatments, mix design method, and microstructure analysis," Delft University of Technology, Delft, 2023.
- [171] T. Bakharev, J. Sanjayan and Y.-B. Cheng, "Effect of admixtures on properties of alkali-activated slag concrete," in *Cement and Concrete Research*, Pergamon, 2000, pp. 1367 - 1374.
- [172] M. Palacios and F. Puertas, "Effect of shrinkage-reducing admixtures on the properties of alkali-activated slag mortars and pastes," in *Cement and Concrete Research*, ELSEVIER, 2007, p. 691–702.
- [173] J. S. F. Collins, "Effect of pore size distribution on drying shrinking of alkali-activated slag concrete," in *Cement and Concrete Research*, 2000, p. 1404–1406.

- [174] J. S. F. Collins, "Sanjayan, Strength and shrinkage properties of alkaliactivated slag concrete containing porous coarse aggregate," in *Cement and Concrete Research*, 1999, p. 607–610.
- [175] M. Palacios and F. Puertas, "Effect of shrinkage-reducing admixtures on the properties of alkali-activated slag mortars and pastes," in *Cement and Concrete Research*, 2007, p. 691–702.
- [176] H. Bezemer, N. Awasthy and M. Luković, "Multiscale analysis of long-term mechanical and durability behaviour of two alkali-activated slag-based types of concrete," in *Construction and Building Materials*, Delft, ELSEVIER, 2023.
- [177] A. P. A. F.-J. P. B. M. Criado, "Alkali activated fly ash: effect of admixtures on paste rheology," 2009. [Online]. Available: <https://link.springer.com/article/10.1007/s00397-008-0345-5>.
- [178] J. D. D. L. N. R. G. Habert, "An environmental evaluation of geopolymer based concrete production: reviewing current research trends," in *Journal of Cleaner Production*, 2011, pp. 1229-1238.
- [179] J. P. G. L. J. v. D. C.A. Rees, "The mechanism of geopolymer gel formation investigated through seeded nucleation," in *Colloids Surfaces A Physicochem*, 2008, p. 97–105.
- [180] L. K. O. F. V. Bilek Jr, "Shrinkage-Reducing Admixture Efficiency in AlkaliActivated Slag across the Different Doses of Activator," in *Key Eng. Mater., Trans Tech Publ*, 2018, pp. 19-22.
- [181] R. Snellings, J. Chwast, Ö. Cizer, N. De Belie, Y. Dhandapani, P. Durdzinski, J. Elsen, J. Haufe, D. Hooton, C. Pat, M. Santhanam, K. Scrivener, D. Snoeck, L. Steger, S. Tongbo, A. Vollpracht, F. Winnefeld and B. Lothenbach, "Report of TC 238-SCM: hydration stoppage methods for phase assemblage studies of blended cements—results of a round robin test," in *Materials and Structures*, link.springer, 2018.
- [182] C. Liu, X. Liang, Y. Chen, Z. Li and G. Ye, "Degradation of alkali-activated slag subjected to water immersion," in *Cement and Concrete Composites*, Delft, Elsevier Ltd, 2023, pp. 105-157.
- [183] "NEN-EN 196-1, "Methods of testing cement - Part 1: Determination of strength," 2016," [Online]. Available: <https://connect.nen.nl/Search/Detail?collectionId=0&compId=10037&colAdmin=false&pState=87>.
- [184] "NEN-EN 12390-13:2021," [Online]. Available: <https://connect.nen.nl/Search/Detail?collectionId=0&compId=10037&colAdmin=false&pState=879>.
- [185] Z. Osmanovica, N. Haračićb and J. Zelić, "Properties of blastfurnace cements (CEM III/A, B, C) based on Portland cement clinker, blastfurnace slag and cement kiln dusts," in *Cement and Concrete Composites*, ELSEVIER, 2018, pp. 189-198.

- [186] X. Ke , S. A. Bernal , O. H. Hussein and J. L. Provis, “Chloride binding and mobility in sodium carbonate activated slag pastes and mortars,” in *Materials and Structures*, UK, CrossMark, 2017.
- [187] S. Joseph and Ö. Cizer, “Hydration of Hybrid Cements at Low Temperatures: A Study on Portland Cement-Blast Furnace Slag—Na<sub>2</sub>SO<sub>4</sub>,” 2022.
- [188] B. Yuan, Q. Yu, E. Dainese and H. Brouwers, “Autogenous and drying shrinkage of sodium carbonate activated slag altered by limestone powder incorporation,” in *Construction and Building Materials*, Eindhoven, ELSEVIER, 2017, pp. 459-468.
- [189] B. Yuan, Q. L. Yu and H. J. H. Brouwers, “Phase modification induced drying shrinkage reduction on Na<sub>2</sub>CO<sub>3</sub> activated slag by incorporating Na<sub>2</sub>SO<sub>4</sub>,” in *Materials and Structures*, Eindhoven, Springer, 2017, pp. 220-231.
- [190] P. Kumar Mehta and P. J. M. Monteiro, *Concrete: Microstructure, Properties, and Materials*, California: University of California at Berkeley, 2006.
- [191] A. Hamdan, H. Song, Z. Yao , M. Fouad Alnahhal, T. Kim and A. Hajimohammadi , “Modifications to reaction mechanisms, phase assemblages and mechanical properties of alkali-activated slags induced by gypsum addition,” in *Cement and Concrete Research*, Sydney, ScienceDirect, 2023.
- [192] Y. Zuo, M. Nedeljković and G. Ye, “Pore solution composition of alkali-activated slag/fly ash pastes,” in *Cement and Concrete Research*, Delft, ELSEVIER, 2019, pp. 230-250.
- [193] H. M. Jennings, “A model for the microstructure of calcium silicate hydrate in cement paste,” in *Cement and Concrete Research*, 2000, pp. 101-116.
- [194] J. J. & J. H. M. Thomas, “Cement and Concrete Researc,” in *Hydration kinetics and microstructure development in Portland cement systems*, 2019.
- [195] S. A. e. a. Bernal, “Cement and Concrete Composites,” in *The influence of activation method on the microstructure and mechanical properties of alkali-activated slag pastes*, 2013, p. 226–235.
- [196] J. L. & B. S. A. Provis, “RILEM TC 224-AAM,” in *Alkali Activated Materials: State-of-the-Art Report*, 2014.
- [197] H. Ye, C. Cartwright, F. Rajab and A. Radlinska, “Understanding the drying shrinkage performance of alkali-activated slag mortars,” in *Cement and Concrete Composites*, United States, ScienceDirect, 2016, pp. 13-24.
- [198] M. Sirotti , B. Delsaute and S. Staquet, “New Experimental Evidence for Drying Shrinkage of Alkali-Activated Slag with Sodium Hydroxide,” 2023. [Online]. Available: [https://www.mdpi.com/1996-1944/16/16/5659?utm\\_source=chatgpt.com](https://www.mdpi.com/1996-1944/16/16/5659?utm_source=chatgpt.com).
- [199] H. Bezemer, N. Awasthy and M. Luković , “Multiscale analysis of long-term mechanical and durability behaviour of,” in *Construction and Building Materials*, Delft, ScienceDirect, 2023.

- [200] European Technical Assessment , “ETA-20/0243 of 15 April 2020,” 15 04 2020. [Online]. Available: chrome-extension://efaidnbmnnnibpcajpcgclclefindmkaj/https://www.dibt.de/pdf\_storage/2020/ETA-20!0243(8.03.01-82!19)e.pdf.
- [201] H. Ye, C. Cartwright, F. Rajabipour and A. Radlińska, “Effect of Drying Rate on Shrinkage of Alkali-Activated Slag Cements,” 24 July 2014. [Online]. Available: chrome-extension://efaidnbmnnnibpcajpcgclclefindmkaj/https://docs.lib.purdue.edu/cgi/viewcontent.cgi?article=1049&context=icdcs.
- [202] Z. LI, “Autogenous shrinkage of alkali-activated slag and fly ash materials: From mechanism to mitigating strategies,” TU Delft, Delft, 2021.
- [203] R. Loser and A. Leemann, “An accelerated sulfate resistance test for concrete,” in *Materials and Structures*, SpringerLink, 2016, p. 3445–3457.
- [204] F. C. , S. Carvalhol, C.-N. Chen and J. F. Labuz , “MEASUREMENTS OF EFFECTIVE ELASTIC MODULUS AND MICROCRACK DENSITY,” [Online]. Available: https://www.sciencedirect.com/science/article/pii/S1365160997002396. [Accessed 1997].
- [205] ACI Committee 209, “Guide for Modeling and Calculating Shrinkage and Creep in Hardened Concrete,” 2008.
- [206] COMITE EURO - INTERNATIONAL DU BETON , “CEB - FIP MODEL CODE 1990,” 1990.
- [207] British Standard, “Code of practice for special,” 2002.
- [208] T. Telford, “CEB-FIP Model Code, Design code 1994, Published by,” London, 1990.
- [209] M. Shariq , J. Prasad b and H. Abbas, “Effect of GGBFS on age dependent static modulus of elasticity of concrete,” in *Construction and Building Materials*, 2013, pp. 411-418.
- [210] F. Ali , A. Al-sairafi, J. Chen and M. Wei, “Drying Shrinkage Characteristics of Mortar Incorporating Different Mineral Admixture,” 2018. [Online]. Available: chrome-extension://efaidnbmnnnibpcajpcgclclefindmkaj/https://www.scitepress.org/Papers/2018/75295/75295.pdf.
- [211] V. Zanjani Zadeh and C. P. Bobko, “Nanoscale mechanical properties of concrete containing blast furnace slag and fly ash before and after thermal damage,” in *Cement and Concrete Composites*, 2013, pp. 215-221.
- [212] M. Riggio , J. Sandak , A. Sandak , D. Pauliny and L. Babiński , “Analysis and prediction of selected mechanical/dynamic properties of wood after short and long-term waterlogging,” in *Construction and Building Materials*, 2014, pp. 444-454.
- [213] D. P. B. a. O. M. Jensen, “Mitigation strategies for autogenous shrinkage cracking,” in *and Concrete Composites*, 2004, p. 677–685.



- [214] Z. LI, “Autogenous shrinkage of alkali-activated slag and fly ash materials: From mechanism to mitigating strategies,” Delft University of Technology, Delft, 2021.
- [215] F. W. F. Beltzung, “Role of disjoining pressure in cement based materials,” in *Cem. Concr. Res.*, 2005, p. 2364–2370.
- [216] M. W. P. L. C. Di Bella, “Evaluation of the ultimate drying shrinkage of cement-based mortars with poroelastic models,” in *Mater. Struct.*, 2017.
- [217] K. v. Breugel, “Numerical modelling of volume changes at early ages-Potential, pitfalls and challenges,” in *Mater. Struct.* 34, 2001, p. 293–301.
- [218] O. J. K. V. B. P. Lura, “Autogenous shrinkage in high-performance cement paste: An evaluation of basic mechanisms,” in *Cem. Concr. Res.* 33, 2003, pp. 223–232.
- [219] K. S. S.D. Wang, “Hydration products of alkali activated slag cement,” in *Cem. Concr. Res.* 25, 1995, p. 561–571.
- [220] J. S. F. Collins, “Effect of pore size distribution on drying shrinking of alkaliactivated slag concrete,” in *Cem. Concr. Res.* 30, 2000, p. 1401–1406.
- [221] M. W. K. S. P. L. H. Chen, “Prediction of self-desiccation in low water-to-cement ratio pastes based on pore structure evolution,” in *Cem. Concr. Res.* 49, 2013, p. 38–47.
- [222] S. P. M. N. B.D. Kumarappa, “Autogenous shrinkage of alkali activated slag mortars: Basic mechanisms and mitigation methods,” in *Cem. Concr. Res.* 109, 2018, pp. 1–9.
- [223] F. R. A. R. C. Cartwright, “Shrinkage Characteristics of Alkali-Activated Slag Cements,” in *J. Mater. Civ. Eng.* 27, 2014, pp. 1–9.
- [224] A. R. H. Ye, “Shrinkage mechanisms of alkali-activated slag,” in *Cem. Concr. Res.* 88, 2016, p. 126–135.
- [225] F. D. J. Ma, “Shrinkage and creep behavior of an alkali-activated slag concrete,” in *Struct. Concr.* 18, 2017, p. 801–810.
- [226] O. C. S. Uppalapati, “Understanding the autogenous shrinkage in alkali-activated slag/fly-ash blends,” in *GEOPOLYMERS VERSATILE Mater.*, 2018, p. 27.
- [227] M. P. H. M. J. D. A. R. J. R. F. Puertas, “A model for the CASH gel formed in alkali-activated slag cements,” in *J. Eur. Ceram. Soc.* 31, 2011, pp. 2043–2056.
- [228] A. F.-J. D. M. I. S. J. S. A. P. I. Garcia-Lodeiro, “Stability of synthetic calcium silicate hydrate gels in presence of alkalis, aluminum, and soluble silica,” in *Transp. Res. Rec.* 2142, 2010, pp. 52–57.
- [229] O. A. Mohamed, “Effects of the Curing Regime, Acid Exposure, Alkaline Activator Dosage, and Precursor Content on the Strength Development of Mortar with Alkali-Activated Slag and Fly Ash Binder: A Critical Review,” *Polymers*, 2023.

- [230] M. Chi, "Effects of dosage of alkali-activated solution and curing conditions on the properties and durability of alkali-activated slag concrete," in *Construction and Building Materials*, Taiwan, Department of Fire Science, WuFeng University, 2012, pp. 240-245.
- [231] R. Priyadarshi, "Shrinkage behaviour of 3D printing concrete mixture," Delft University of Technology, Delft, 2021.
- [232] B. Lothenbach, K. Scrivener and R. Hooton, "Supplementary cementitious materials," in *Cement and Concrete Research*, Toronto, ScienceDirect, 2010, pp. 1244-1256.
- [233] F. Collins and J. Sanjayan, "Effect of pore size distribution on drying shrinkage of alkali-activated slag concrete," in *Cement and Concrete Research* 30, Australia, Pergamon, 2000, pp. 1401 - 1406.
- [234] M. Ben Haha, G. Le Saout, F. Winnefeld and B. Lothenbach, "Influence of activator type on hydration kinetics, hydrate assemblage and microstructural development of alkali activated blast-furnace slags," in *Cement and Concrete Research*, Dübendorf, ELSEVIER, 2011, pp. 301 - 310.
- [235] H. Wu , G. Ye, H. Dong, Z. Li and S. Barbosa Nunes, "Improving freeze-thaw resistance of alkali-activated slag by admixtures," TU Delft, Delft, 2023.
- [236] W. Piasta and H. Sikora, "Effect of air entrainment on shrinkage of blended cements concretes," in *Construction and Building Materials*, Poland, ELSEVIER, pp. 298-307.
- [237] S. De Carvalho Gomes, . Q. Dieu Nguyen , W. Li and A. Castel, "Effects of mix composition on the mechanical, physical and durability properties of alkali-activated calcined clay/slag concrete cured under ambient condition," in *Construction and Building Materials*, ELSEVIER, 2024.
- [238] M. Palacios and F. Puertas, "Effect of shrinkage-reducing admixtures on the properties of alkali-activated slag mortars and pastes," in *Cement and Concrete Research*, Madrid, ELSEVIER, 2007, p. 691-702.
- [239] H. Ma, H. Zhu, C. Wu, J. Fan, . S. Yang and Z. Hang, "Effect of shrinkage reducing admixture on drying shrinkage and durability of alkali-activated coal gangue-slag material," in *Construction and Building Materials*, ELSEVIER, 2021.
- [240] T. Bakharev, J. Sanjayan and . Y.-B. Cheng, "Effect of admixtures on properties of alkali-activated slag concrete," in *Cement and Concrete Research*, Pergamon, 2000.
- [241] J. Yuan, W. Lindquist, D. Darwin and J. Browning, "Effect of Slag Cement on Drying Shrinkage of Concrete," 2015. [Online].
- [242] F. A. Ali Al-sairafi, J. Chen, M. Wei, Y. Wang and P. Li, "Drying Shrinkage Characteristics of Mortar Incorporating Different Mineral Admixture," 2010. [Online].
- [243] "NEN-EN 12390-13 Testing hardened concrete - Part 13: Determination of secant modulus of elasticity in compression," juli 2021. [Online]. Available: <https://www.nen.nl/nen-en-12390-13-2021-en-285738>.

- [244] H. A. Neckles and F. T. Short, "The effects of global climate change on seagrasses," 1 April 1999. [Online]. Available: <https://www.sciencedirect.com/science/article/pii/S030437709800117X>.
- [245] IPCC, "Climate Change," 2014. [Online]. Available: [https://www.ipcc.ch/site/assets/uploads/2018/02/AR5\\_SYR\\_FINAL\\_SPM.pdf](https://www.ipcc.ch/site/assets/uploads/2018/02/AR5_SYR_FINAL_SPM.pdf).
- [246] A. Hamdan, H. Song, Z. Yao, M. Fouad Alnahhal, T. Kim and A. Hajimohammadi , "Modifications to reaction mechanisms, phase assemblages and mechanical properties of alkali-activated slags induced by gypsum addition," in *Cement and Concrete Research*, ScienceDirect, 2023, p. 174.
- [247] . J. L. Provis, A. Palomo and C. Shi, "Advances in understanding alkali-activated materials," in *Cementand Concrete Research*, ScienceDirect, 2015.
- [248] J. L. Provis, "Alkali-activatedmaterials," in *CementandConcreteResearch*, SciencDirect, 2018, pp. 40-48.
- [249] N. Bella, E. Gudiel, L. Soriano, A. Font, . M. Victoria Borrachero, J. Paya and J. Maria Monzó, "Formulation of Alkali-Activated Slag Binder Destined for Use in Developing Countries," 18 December 2020. [Online]. Available: [https://www.mdpi.com/2076-3417/10/24/9088?utm\\_source=chatgpt.com](https://www.mdpi.com/2076-3417/10/24/9088?utm_source=chatgpt.com).
- [250] Z. Jia, Y. Yang, L. Yang, Y. Zhang and Z. Sun, "Hydration products, internal relative humidity and drying shrinkage of alkali activated slag mortar with expansion agents," in *Construction and Building Materials*, Nanjing, ScienceDirect, 2017, pp. 198-207.
- [251] "INNOVATIVE TECHNIQUES AND MATERIALS FOR PREVENTING CONCRETE SHRINKAGE CRACKING," BUREAU OF RESEARCH, 2023.
- [252] G. R. Lomboy, D. B. Cleary, C. Zhu, S. Kawashima, P. Badjatya and S. Michael Wagner , "INNOVATIVE TECHNIQUES AND MATERIALS FOR PREVENTING CONCRETE SHRINKAGE CRACKING," BUREAU OF RESEARCH, 2023.
- [253] K. Nagendra Shivaprasad, H.-M. Yang and J. Kumar Singh, "A path to carbon neutrality in construction: An overview of recent progress in recycled cement usage," [Online]. Available: <https://www.sciencedirect.com/science/article/pii/S2212982024001513>. [Accessed 20 May 2024].
- [254] P. Kumar Mehta and P. J. M. Monteiro, "CONCRETE Microstructure, Properties and Materials," [Online]. Available: <https://www.accessengineeringlibrary.com/content/book/9780071797870>. [Accessed 20 October 2001].
- [255] R. M. Andrew, "Global CO<sub>2</sub> emissions from cement production, 1928–2017," in *Earth Syst. Sci. Data*, 10, , Norway, Copernicus Publications., 2018, p. 2213–2239.
- [256] S.-D. Wang, X.-C. Pu and K. L. Scrivener, "Alkali-activated slag cement and concrete: a review of properties and problems," 01 July 1995. [Online]. Available:

<https://www.emerald.com/jadcr/article-abstract/7/27/93/392774/Alkali-activated-slag-cement-and-concrete-a-review?redirectedFrom=fulltext>.

- [257] Z. Shi , C. Shi , S. Wan and Z. Ou, “Effect of alkali dosage on alkali-silica reaction in sodium hydroxide activated slag mortars,” in *Construction and Building Materials*, Changsha, ScienceDirect, 2017, pp. 16-23.
- [258] X. Ouyang, Y. Ma, Z. Liu, J. Liang and G. Ye, “Effect of the Sodium Silicate Modulus and Slag Content on Fresh and Hardened Properties of Alkali-Activated Fly Ash/Slag,” [Online]. Available: <https://www.mdpi.com/2075-163X/10/1/15>. [Accessed 23 December 2019].
- [259] R. M. Andrew, “Global CO2 emissions from cement production, 1928–2017,” 10 d 2018. [Online]. Available: <https://essd.copernicus.org/articles/10/2213/2018/>.
- [260] P. Duxson, A. Fernández-Jiménez, J. L. Provis, G. C. Lukey, A. Palomo and J. S. J. van Deventer , “Geopolymer technology: the current state of the art,” in *Journal of Materials Science*, Springer Nature Link, 2006, p. 2917–2933.
- [261] Q. Zhang, R. Le Roy, M. Vandamme and B. Zuber , “Long-term creep properties of cementitious materials: Comparing microindentation testing with macroscopic uniaxial compressive testing,” in *Cement and Concrete Research*, ELSEVIER, 2014, pp. 89-98.

# Appendix

## Appendix A: Determination of secant modulus of elasticity

Method A – Determination of initial and stabilized secant modulus of elasticity, according to NEN-EN 12390-13:2021, art. 7.3.

### 1) Preloading Procedure and Verification Checks

To ensure the system's stability and confirm the correct placement of the test specimen, three preloading cycles were performed. These cycles served two main purposes: verifying the wiring system (first verification) and checking the specimen's alignment within the testing setup (second verification). The specimens were carefully mounted in the centre of the testing machine, and the measuring instruments were aligned with the loading axis.

#### - Cycle Details:

In the first cycle, the stress applied to the specimen was gradually increased at a controlled rate of  $(0.6 \pm 0.2)$  MPa/s until it reached a target stress level, referred to as  $\sigma_b$ . This stress was held steady, within 5% of the intended value, for as short a time as possible, but no longer than 20 seconds. At this point, the lower stress value was recorded.

The stress was then reduced, at the same rate, down to the preload level,  $\sigma_p$ , and again held for up to 20 seconds. After this, the strain measuring instruments were reset to zero.

This entire loading sequence was repeated two more times (for a total of three cycles). After the second and third cycles, strain measurements ( $\epsilon_b$ ) were taken at the lower stress level along each measurement line.

#### - Post-Cycle Verification:

Once all three preloading cycles were complete and the preload stress stabilized (within  $\pm 5\%$  of the target), two quick checks were carried out, both within 60 seconds:

#### - First Verification:

For each measurement line, the difference in  $\epsilon_b$  between the second and third cycles must be within 10%. If the variation exceeds this limit, the test must be paused. The instruments should be re-checked or recalibrated, and the test restarted. If the variation still exceeds 10% after restarting, the test is stopped.

#### - Second Verification:

The  $\epsilon_b$  values from the third cycle must be consistent across all measurement lines, differing by no more than 20% from the average. If they vary more than that, the specimen must be repositioned and the test repeated. If the values are still outside the allowed range after recentring, the test is stopped and the specimen is rejected.

## 2) Loading Procedure and Measurement Recording

The testing process began by increasing the stress from the preload level to the lower stress level at a controlled rate of  $(0.6 \pm 0.2)$  MPa/s. Once the lower stress level was reached, it was held steady within  $\pm 5\%$  of the target value for the shortest possible time, but not longer than 20 seconds. At the end of this hold period, strain readings were taken along each measurement line, and the average strain, referred to as  $\varepsilon_{b,0}$ , was calculated.

- A total of three loading cycles were carried out.

In each cycle, the stress was increased at the same rate until it reached the upper stress level,  $\sigma_a$ . This upper level was held within  $\pm 5\%$  of the nominal value, again for no more than 20 seconds. In the first and second cycles, the stress was then decreased at the same rate back to the lower stress level, which was held within  $\pm 5\%$  for up to 20 seconds.

## 3) Strain measurements were taken at specific points during the cycles:

After the upper stress level in the first and third cycles, once the load had stabilized, the strain was recorded. The average strains at these stages were labelled  $\varepsilon_{a,1}$  and  $\varepsilon_{a,3}$ , respectively.

At the end of the lower stress level in the second cycle, the stabilized strain was also recorded, and the average value  $\varepsilon_{b,2}$  was determined.

Additionally, the actual stress values at the lower and upper levels  $\sigma_{bm}$  and  $\sigma_{am}$ , respectively were recorded.

Once all measurements for the third cycle were complete, the test continued to failure in order to determine the compressive strength of the specimen, following the procedure outlined in EN 12390-3. The resulting strength value was recorded to the nearest 0.1 MPa.

To avoid damaging the strain gauges during the final failure stage, it may be wise to remove the measuring instruments beforehand. If this is done, it should be done carefully to ensure safety.

If the measured compressive strength differs from the specified value,  $f_c$ , by more than 20%, this discrepancy must be noted in the test report.

An illustration of the loading cycle used to determine the elastic modulus is provided in Figure A1.

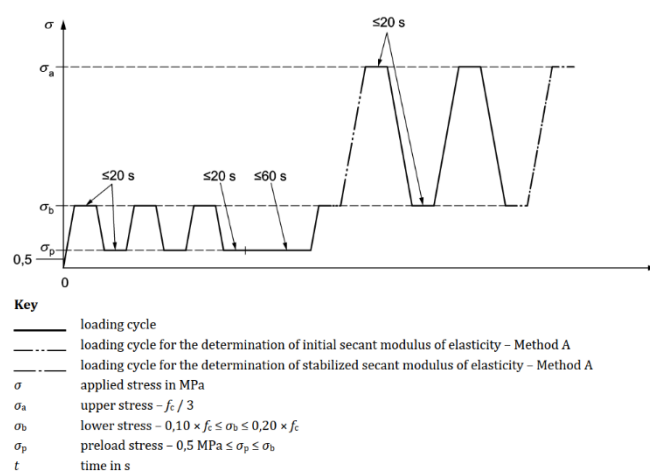


Figure A1: Determination of initial and stabilized secant modulus of elasticity [243].

## Appendix B: Methods of testing cement - Part 1: Determination of strength

### B1) Flexural Strength Testing Procedure

The three-point loading method must be used, following one of the equipment setups described in Section 4.7 of NEN-EN 196-1. The prism specimen should be placed in the testing apparatus so that one of its side faces rests on the two supporting rollers. The prism's longitudinal axis must be positioned perpendicular to the supports. The load is then applied vertically to the opposite side face using the loading roller and increased smoothly at a rate of  $(50 \pm 10)$  N/s until the specimen fractures.

After the fracture occurs, both halves of the prism should be covered with a damp cloth to retain moisture until they are tested in compression.

The flexural strength, denoted as  $R_f$  and expressed in megapascals (MPa), is calculated using the following formula:

$$R_f = \frac{1.5 F_f L}{b^3} \quad (B1)$$

Where:

- $R_f$  = flexural strength (MPa)
- $F_f$  = applied load at the point of fracture (N)
- $L$  = distance between the supports (span length, in mm)
- $b$  = side length of the square cross-section of the prism (mm)

### B2) Compressive Strength Testing Procedure

The test of compressive strength shall be conducted on the two halves of the prism that were fractured previously either according to the method prescribed in Section B.1 or by another appropriate method which does not induce damaging stresses on the prism halves.

As per sections 4.8 and 4.9 of NEN-EN 196-1, the load is applied to the side faces of each half for testing. During setup.

Place the two halves centrally on the machine's platens, with lateral misalignment not exceeding  $\pm 0.5$  mm.

Longitudinally, each half shall be placed such that the end face protrudes about 10 mm beyond the edge of the platens or auxiliary plates.

The load should be applied smoothly and steadily at  $(2400 \pm 200)$  N/s and this rate should be maintained to fracture the specimen. When the load is manually controlled, the test must be conducted in a very careful manner near the fracture so that the loading rate is not changed suddenly to maintain good results.

The compressive strength, which is signified as  $R_c$  and is expressed as MPa, is given by the formula.

$$R_c = \frac{F_c}{A} \quad (B2)$$



Where:

- $R_c$  = compressive strength (MPa).
- $F_c$  = maximum load applied at fracture (N).
- $A$  = Area of the platens or auxiliary plates in contact with the specimen ( $\text{mm}^2$ ).